• Institute of Fundamental Technological Research
• Polish Academy of Sciences
• Warsaw • Poland

LECTURE NOTES 5

A. L. Yarin

Electrospinning of Nanofibers from Polymer Solutions and Melts

Centre of Excellence for
Advanced Materials and Structures

Warsaw 2003

AMAS LECTURE NOTES

Edition of this volume has been partially supported by the European Commission

Published and distributed by
Institute of Fundamental Technological Research
Świętokrzyska 21, 00-049 Warszawa, Poland

ISSN 1642-0578

Papier offset. kl. III, 70 g, B1
Ark. wyd.: 8.3; ark. druk.: 7
Skład w systemie TEX: T.G. Zieliński
Oddano do druku: I 2003; druk ukończono: II 2003
Druk i oprawa: Drukarnia Braci Grodzickich, Piaseczno, ul. Geodetów 47a

Contents

Abstract

A straightforward, cheap and unique method to produce novel fibers with a diameter in the range of 100 nm and even less is related to electrospinning. For this goal, polymer solutions or melts, liquid crystals, suspensions of solid particles and emulsions, are electrospun by a voltage of about 10 kV/10 cm. The electric force results in an electrically charged jet of polymer solution flowing out from a pendant droplet. After the jet flows away from the droplet in a nearly straight line, it bends into a complex path and other changes in shape occur, during which electrical forces stretch and thin it by very large ratios. After the solvent evaporates, birefringent nanofibers are left. Nanofibers of ordinary, conducting and photosensitive polymers were electrospun. The present course deals with the mechanism and electro-hydrodynamic modeling of the instabilities and related processes resulting in electrospinning of nanofibers. Also some applications are discussed. In particular, a unique electrostatic field-assisted assembly technique was developed with the aim to position and align individual conducting and light-emitting nanofibers in arrays and ropes. These structures are of potential interest in the development of novel polymer-based light-emitting diodes, diodes, transistors, photonic crystals and flexible photocells. Some other applications discussed include micro-aerodynamic decelerators based on permeable nanofiber mats and tiny flying objects and sensors (smart dust), nanofiber-based filters, protective clothing, biomedical applications including wound dressings, drug delivery systems based on nanotubes, the design of solar sails, light sails and mirrors for use in space, the application of pesticides to plants, structural elements in artificial organs, reinforced composites, as well as nanofibers reinforced by carbon nanotubes.

Chapter 1

Introduction and background

The preparation of organic, inorganic materials, of semiconductor systems which are functionalized via a structuring process taking place on the submicrometer scale – nanotechnology – is currently an area of intense activities both in fundamental and applied science on an international scale. Depending on the application, one has in mind three-dimensional systems (photonic band gap materials), two-dimensional systems (quantum well structures), or one-dimensional systems (quantum wires, nanocables). Semi-ordered or disordered (non-woven) systems are of interest for such applications as filter media, fiber-reinforced plastics, solar and light sails and mirrors in space, application of pesticides to plants, biomedical applications (tissue engineering scaffolds, bandages, drug release systems), protective clothing aimed for biological and chemical protection, and fibers loaded with catalysts and chemical indicators. For a broad range of applications one-dimensional systems, i.e. nanofibers, hollow nanofibers (nanotubes) are of fundamental importance [1−5].

The reduction of the diameter into the nm-range gives rise to a set of favorable properties including the increase of the surface to volume ratio, variations in the wetting behaviour, modifications of the release rate or a strong decrease of the concentration of structural defects on the fiber surface which will enhance the strength of the fibers.

For a great number of other types of applications one is interested in tubular structures, i.e. hollow nanofibers, nanotubes, porous systems with

narrow channels [6–9]. Such systems are of interest among others for drug delivery systems, separation and transport applications, for micro- reactors and for catalysts, for microelectronic and optical applications (nanocables, light guiding, tubes for the near-field microscopy). Such tubular objects can be used to impose confinement effects on optical and electronic properties, or they can be used as templates for the growth of fiber-shaped systems, for the creation of artificial viruses, or a protein-storage medium.

Various approaches leading to thin compact fibers and hollow fibers have been described in the past [1–9]. Yet these approaches are either limited to fiber dimensions well above 1 μm or they are limited to specific materials. The extrusion of hollow fibers or compact fibers from the melt or solution is an example for the first case and the preparation of carbon nanotubes is an example for the second case. Our main aim in the present course is the electrospinning process allowing for the preparation of such nanoscaled objects for a broad range of different polymer materials and on a technical scale.

Chapter 2

Various methods of producing nanofibers

Nanofibers can be obtained by a number of methods: via air-blast atomization of mesophase pitch, via assembling from individual carbon nanotube molecules [10], via pulling of non-polymer molecules by an AFM tip [11], via depositing materials on linear templates or using whiskers of the semiconductor which spontaneously grow out of gold particles placed in the reactor chamber [12]. InP (indium phosphide) nanowires were prepared by laser-assisted catalytic growth [13], molybdenum nanowires were electrodeposited [14]. Step-by-step application of organic molecules and metal ions on predetermined patterns [15] and DNA-templated assembly [16, 17] were also proposed as possible routes towards nanofibers and nanowires.

While air-blast atomization of mesophase pitch allows for a fast generation of a significant and even a huge amount of non-woven nanofibers in a more or less uncontrollable manner, the other methods listed above allow for a rather good process control. However, all of them yield significantly short nanofibers and nanowires with the lengths of the order of several microns. They are also not very flexible with respect to material choice.

Electrospinning of nanofibers, nanowires and nanotubes represents a very flexible method which allows for manufacturing of long nanofibers (of the order of ten centimeters) and a relatively easy route for their assembly and manipulation. The number of polymers which were electrospun to make nanofibers and nanotubes approaches one hundred. These include both organic

and silicon-based polymers. Electrospinning is considered in detail in the following sections.

Chapter 3

Electrospinning of nanofibers

Electrospinning is a straightforward and cost effective method to produce novel fibers with diameters in the range of from less than 3 nm to over 1 μm, which overlaps contemporary textile fiber technology. Electrified jets of polymer solutions were investigated as routes to the manufacture of polymer nanofibers [18−22]. Since 1934, when a U.S. patent on electrospinning was issued to Formhals [23], over 30 U.S. patents have been issued. Nanofibers of polymers were electrospun by creating an electrically charged jet of polymer solution at a pendant or sessile droplet. In the electrospinning process a pendant drop of fluid (a polymer solution) becomes unstable under the action of the electric field, and a jet is issued from its tip. An electric potential difference, which is around 10 kV, is established between the surface of the liquid drop (or pipette, which is in contact with it) and the collector/ground. After the jet flowed away from the droplet in a nearly straight line, it bent into a complex path and other changes in shape occurred, during which electrical forces stretched and thinned it by very large ratios. After the solvent evaporated, birefringent nanofibers were left. The above scenario is characteristic of the experiments conducted by a number of groups with very minor variations [18, 22, 24−33]. Templates for manufacturing nanotubes are also electrospun by the same method [34−38]. A recent review can also be found in [39].

Chapter 4

Taylor cone and jetting from liquid droplets in electrospinning of nanofibers [1)]

Sessile and pendant droplets of polymer solutions acquire stable shapes when they are electrically charged by applying an electrical potential difference between the droplet and a flat plate, if the potential is not too large. These stable shapes result only from equilibrium of the electric forces and surface tension in the cases of inviscid, Newtonian, and viscoelastic liquids. It is widely assumed that when the critical potential φ_{0^*} has been reached and any further increase will destroy the equilibrium, the liquid body acquires a conical shape referred to as the Taylor cone [41], having a half angle of 49.3°. In the present section we show that the Taylor cone corresponds essentially to a specific self-similar solution, whereas nonself-solutions exist which do not tend towards a Taylor cone. Thus, the Taylor cone does not represent a unique critical shape: another shape exists which is not self-similar. The experiments demonstrate that the half-angles observed are much closer to the new shape. In this section a theory of stable shapes of droplets affected by an electric field is exposed and compared with data acquired in the experimental work on electrospinning of nanofibers from polymer solutions and melts.

Consider a droplet positioned inside a capacitor. As the strength of the field E increases, the droplet becomes more and more prolate until no shape is stable beyond some critical value E^*. This resembles the behaviour recorded

[1)] The results presented in this chapter were published by A.L. Yarin, S. Koombhongse and D.H. Reneker in [40].

in the seminal work of Taylor [41] for droplets subjected to a higher and higher potential Φ_0: they elongate to some extent, but then suddenly tend to a cone-like shape. The boundary between the stable electrified droplets and those with a jet flowing from the tip lies somewhere near the critical value of the potential (or the field strength). Taylor calculated the half-angle at the tip of an infinite cone arising from an infinite liquid body. In Sec. 4.1 we calculate the half-angle by a different method which brings out the self-similar nature of the Taylor cone, and states the assumptions involved in its calculation. Then, in Sec. 4.2 we consider a family of nonself-similar solutions for the hyperbolical shapes of electrified liquid bodies in equilibrium with their own electric field due to surface tension forces. In Sec. 4.3 we show that these solutions do not tend to the self-similar solution corresponding to the Taylor cone, and represent an alternative to the Taylor cone. Thus we conclude that another shape, one tending towards a sharper cone than that of Taylor, can precede the stability loss and the onset of jetting. In Sec. 4.4 experimental results are presented and compared with the theory. These results confirm the theoretical predictions of Sec. 4.3.

4.1. Taylor cone as a self-similar solution

All the liquids we deal with throughout Chapter 4 are considered to be perfect ionic conductors. The reason that the assumption of a perfect conductor is valid in the present case is in the following. The characteristic charge relaxation time $\tau_C = \varepsilon/(4\pi\sigma)$, where ε is the dielectric permeability and σ is the electric conductivity. The plausible values of these parameters for the polymer solutions used in electrospinning and for many other leaky dielectric fluids are $\varepsilon \cong 40$ and $\sigma = 10^{-6}\,\mathrm{S/m} = 9 \cdot 10^3\,\mathrm{s}^{-1}$. Therefore $\tau_C = 0.35\,\mathrm{ms}$. If a characteristic hydrodynamic time $\tau_H \gg \tau_C$, then the fluid behaviour is that of a perfect conductor in spite of the fact that it is actually a poor conductor (leaky dielectric) compared to such good conductors as metals. In the present chapter τ_H is associated with the residence time of fluid particles in the droplets which is of the order of 1 s in the experiments. Therefore $\tau_H \gg \tau_C$ and the approximation of a perfect conductor is fully justified.

Under the influence of an applied potential difference, excess charge flows to or from the liquid. Anions and cations are distributed non-uniformly on the surface of the liquid. The free surfaces of the liquids are always equipotential

surfaces with the charges distributed in a way that maintains a zero electric field inside the liquid.

To establish the self-similar nature of the solution corresponding to the Taylor cone, we consider an axisymmetric liquid body kept at a potential (φ_0+const) with its tip at a distance a_0 from an equipotential plane (Fig. 4.1). The distribution of the electric potential $\Phi = \varphi + \text{const}$ is described in the spherical coordinates R and θ, and in the cylindrical coordinates ρ and z (see Fig. 4.1). The shape of the free surface is assumed to be that of equilibrium, which means that the electrical forces acting on the droplet in Fig. 4.1 are balanced by the surface tension forces. The potential φ_0 can, in such a case, always be expressed in terms of the surface tension coefficient σ and of a_0, specifically as $\varphi_0 = C(\sigma a_0)^{1/2}$, where C is a dimensionless factor. Due to the dimensional arguments the general representation of φ is, in the present case, $\varphi = \varphi_0 F_1(R/a_0, \theta)$, where F_1 is a dimensionless function. The value of the potential Φ throughout the space that surrounds the liquid body is given by

$$\Phi = (\sigma a_0)^{1/2} F\left(\frac{R}{a_0}, \theta\right) + \text{const}, \tag{4.1}$$

where $F = C F_1$ is a dimensionless function.

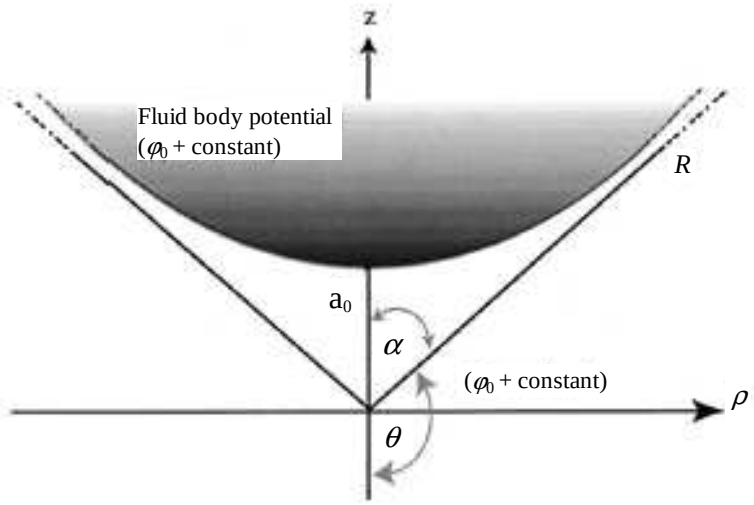

FIGURE 4.1. Axisymmetric "infinite" fluid body kept at potential $\Phi_0 = \phi_0 + \text{const}$ at a distance a_0 from an equipotential plane kept at $\Phi = \text{const}$.

At distances $R \gg a_0$, where it can be assumed that the influence of the gap a_0 is small, the function F should approach a specific power-law scaling

$$F\left(\frac{R}{a_0}, \theta\right) = \left(\frac{R}{a_0}\right)^{1/2} \Psi(\theta) \tag{4.2}$$

($\Psi(\theta)$ being a dimensionless function), whereupon Eq. (4.1) takes the asymptotic self-similar form, independent of a_0

$$\Phi = (\sigma R)^{1/2}\, \Psi(\theta) + \text{const.} \tag{4.3}$$

Power-law scalings leading to self-similar solutions are common in the boundary-layer theory (cf., for example, [42] and [43], and references therein). In particular, such self-similar solutions for jets and plumes, considered as issuing from a pointwise source, in reality correspond to the non-self-similar solutions of the Prandtl equations for the jets and plumes being issued from finite-size nozzles, at distances much larger than the nozzle size [43, 44]. The remote-asymptotic and self-similar solution [45] for capillary waves generated by a weak impact of a droplet of diameter D onto a thin liquid layer, emerges at distances much greater than D from the centre of impact. The self-similar solution for the electric field Eq. (4.3) is motivated by precisely the same idea, and is expected to be the limit to all non-self-similar solutions at distances $R \gg a_0$.

This solution should also satisfy the Laplace equation, which enables us to find Ψ as [41]

$$\Psi(\theta) = P_{1/2}(\cos\,\theta), \tag{4.4}$$

where $P_{1/2}(\cos\theta)$ is a Legendre function of order $1/2$.

The free surface becomes equipotential only when θ corresponds to the only zero of $P_{1/2}(\cos\theta)$ in the range $0 \leqslant \theta \leqslant \pi$, which is $\theta_0 = 130.7°$ [41]. Then the fluid body shown in Fig. 4.1 is enveloped by a cone with the half-angle at its tip equal to $\alpha = \alpha_T = \pi - \theta_0 = 49.3°$, which is the Taylor cone [41]. The shape of the liquid body in Fig. 4.1 would then approach the Taylor cone asymptotically as $R \to \infty$. Taylor's self-similarity assumption leading to Eqs. (4.2) and (4.3) also specifies that $\Phi \to \infty$ as $R \to \infty$, which is quite peculiar. In Sec. 4.2 we show that relevant non-self-similar solutions do not follow this trend as $R \to \infty$, which means that these solutions are fundamentally different from the solution corresponding to the Taylor cone.

4.2. Nonself-similar solutions for hyperboloidal liquid bodies

Experimental data of [41] and numerous subsequent works show that droplets acquire a static shape that does not depend on the initial shape. This static shape is stable if the strength of the electric field does not exceed a certain critical level. As the electric field approaches the critical value, the droplet shape approaches that of a cone with a rounded tip. The radius of curvature of the tip can become too small to be seen in an ordinary photograph (to be discussed in Sec. 4.4). Nevertheless, the tip should be rounded, since otherwise the electric field would become infinite at the tip. Detailed calculation of the exact droplet shape near the tip is an involved nonlinear integro-differential problem, since the field depends on the droplet shape and vice versa. To simplify such calculations, approximate methods were proposed [41, 46, 47]. In those approximate methods a likely shape for a droplet is chosen that would satisfy the stress balance between the electric field and surface tension in an approximate way. In the present problem any likely droplet shape must be very close to a hyperboloid of revolution. Therefore the first theoretical assumption is that the droplet shape is a hyperboloid of revolution. In this section we show that such a hyperboloidal droplet approaches a static shape that is very close to that of a cone with a rounded tip. The tip has a very small radius of curvature. This hyperboloid corresponds to the experimental evidence (discussed in Sec. 4.4).

In calculating an electric field about a body shaped as a hyperboloid of revolution, like the one denoted BCD in Figs. 4.2(b) and 4.2(c), it is natural to use the prolate spheroidal coordinate system (ξ, η). We assume that the tip of the hyperboloid BCD is situated at a distance a_0 from the equipotential surface $z = 0$ and the range in which a solution is sought corresponds to $0 \leqslant \xi \leqslant \xi_0 < 1,\ 1 \leqslant \eta \leqslant \infty$. The surface of hyperboloid BCD is represented by ξ_0 (see Fig.4.2(c)). Coordinate isolines are also shown in Fig. 4.2, with the lines $\eta = \text{const}$ representing ellipsoids, and the lines $\xi = \text{const}$ representing hyperboloids.

The second theoretical assumption is that the space charge effects are negligible. This assumption is discussed in detail in Sec. 4.4. Then the electric potential Φ satisfies the Laplace equation. In prolate spheroidal coordinates

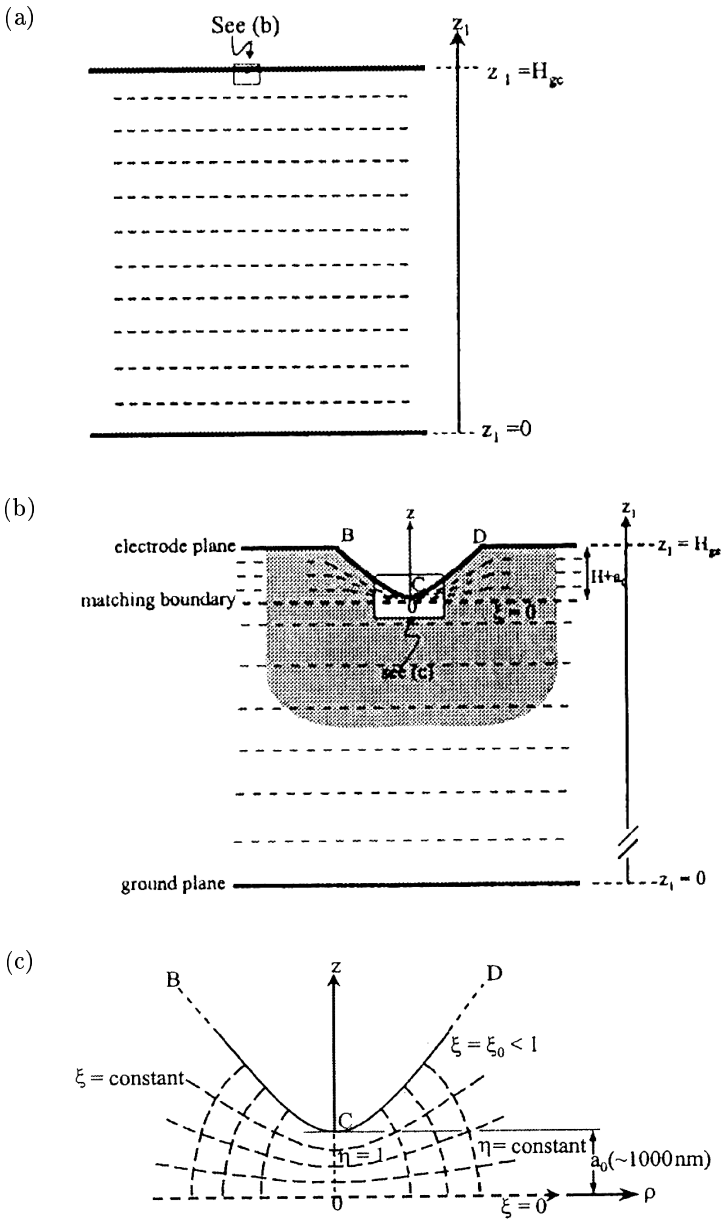

FIGURE 4.2. Prolate spheroidal coordinate system about a hyperboloidal liquid body BCD. (a) Equipotential lines are shown for $0 \leqslant z_1 \leqslant H_{ge} - (H + a_0)$. (c) Equipotential lines ($\xi = \text{const}$) are shown for $H_{ge} - (H + a_0) \leqslant z_1 \leqslant H_{ge}$.

it takes the form [48]

$$\frac{\partial}{\partial\xi}\left[(1-\xi^2)\frac{\partial\Phi}{\partial\xi}\right]+\frac{\partial}{\partial\eta}\left[(\eta^2-1)\frac{\partial\Phi}{\partial\eta}\right]=0, \tag{4.5}$$

which has the general solution,

$$\Phi=\sum_{m=0}^{\infty}\left[A_m\,P_m(\xi)+B_m\,Q_m(\xi)\right]\left[A'_m\,P_m(\eta)+B'_m\,Q_m(\eta)\right]+\text{const}, \tag{4.6}$$

where $P_m(\cdot)$ and $Q_m(\cdot)$ are the Legendre functions and associated Legendre functions of integer order m, respectively, and A_m, B_m, A'_m, B'_m are the constants of integration.

Since in the present case the range of interest includes $\eta=1$ (cf. Fig. 4.2) where $Q_m(1)=\infty$, to have a finite solution we should take $B'_m=0$. Also in the present case it suffices to consider only the first term of Eq. (4.6) corresponding to $m=0$. We then obtain from Eq. (4.6)

$$\Phi=A''_0P_0(\eta)\left[P_0(\xi)+B''_0Q_0(\xi)\right]+\text{const}, \tag{4.7}$$

where $A''_0=A_0A'_0$, $B''_0=B_0/A_0$, $P_0(\eta)=P_0(\xi)=1$, and $Q_0(\xi)=(1/2)\cdot\ell n[(1+\xi)/(1-\xi)]$.

Expression (4.7) then takes the form

$$\Phi=D\ell n\left(\frac{1+\xi}{1-\xi}\right)+\text{const}, \tag{4.8}$$

where D is a constant, determined by the circumstance that the free surface of the hyperboloid BCD at $\xi=\xi_0$ is kept at a potential $\Phi_0=\varphi_0+\text{const}$. Then $D=\varphi_0/\ell n[(1+\xi_0)/(1-\xi_0)]$, and

$$\Phi=\varphi_0\frac{\ell n[(1+\xi)/(1-\xi)]}{\ell n[(1+\xi_0)/(1-\xi_0)]}+\text{const}. \tag{4.9}$$

Note that a similar solution was found and used in [46].

Hyperboloid BCD is given by the expression

$$\frac{z^2}{a_0^2}-\frac{\rho^2}{b_0^2}=1, \tag{4.10}$$

where

$$a_0^2=c^2\xi^2, \tag{4.11a}$$

$$b_0^2=c^2(1-\xi^2), \tag{4.11b}$$

and c is a constant.

The normal derivative of the electric potential at its surface is given by

$$\left.\frac{\partial\Phi}{\partial n}\right|_{\xi=\xi_0} = \frac{1}{c}\left(\frac{1-\xi^2}{\eta^2-\xi^2}\right)^{1/2}\left.\frac{\partial\Phi}{\partial\xi}\right|_{\xi=\xi_0}, \tag{4.12}$$

which yields, using Eq. (4.9)

$$\left.\frac{\partial\Phi}{\partial n}\right|_{\xi=\xi_0} = \frac{2\varphi_0}{\ell n[(1+\xi_0)/(1-\xi_0)]}\,\frac{1}{c[(\eta^2-\xi_0^2)(1-\xi_0^2)]^{1/2}}. \tag{4.13}$$

From Eq. (4.11a) it is seen that for the hyperboloid considered $c = a_0/\xi_0$.

Expression (4.13) characterizes the charge distribution over the free surface BCD with the maximal charge at the tip, where $\eta = 1$. The only non-zero stress of electric origin acting on BCD is the normal stress,

$$\sigma_{nn} = \frac{1}{8\pi}\left.\left(\frac{\partial\Phi}{\partial n}\right)^2\right|_{\xi=\xi_0}, \tag{4.14}$$

which yields the stress distribution over the surface of the hyperboloid ξ_0

$$\sigma_{nn}|_{\xi=\xi_0} = \frac{\varphi_0^2}{2\pi\ell n^2[(1+\xi_0)/(1-\xi_0)]}\,\frac{1}{[(z^2/\xi_0^2-a_0^2)(1-\xi_0^2)]}. \tag{4.15}$$

The z-coordinates of points on the free surface are z.

It is emphasized that to arrive at Eq. (4.15) we also used Eq. (4.11a) and the first formula relating the cylindrical and the prolate spheroidal coordinates

$$z = c\,\eta\,\xi, \tag{4.16a}$$

$$\rho = c[(1-\xi^2)(\eta^2-1)]^{1/2}. \tag{4.16b}$$

From Eq. (4.15) it follows that the stresses σ_{nn} at the tip of hyperboloid BCD at $z = a_0$ and $H \gg a_0$ are given by

$$\begin{aligned}\sigma_{nn}|_{z=a_0} &= \sigma_{nn,\max}\\ &= \frac{\varphi_0^2}{2\pi\ell n^2\,[(1+\xi_0)/(1-\xi_0)]}\left(\frac{\xi_0}{a_0}\right)^2\frac{1}{(1-\xi_0^2)^2},\end{aligned} \tag{4.17a}$$

$$\begin{aligned}\sigma_{nn}|_{z=H} &= \sigma_{nn,\min}\\ &= \frac{\varphi_0^2}{2\pi\ell n^2[(1+\xi_0)/(1-\xi_0)]}\,\frac{1}{[(H^2/\xi_0^2-a_0^2)(1-\xi_0^2)]}.\end{aligned} \tag{4.17b}$$

It should be noted that the solutions obtained above for the electric field about hyperboloidal bodies are exact. However, for liquid bodies the shape of the free surface cannot, *a priori*, be expected to be a perfect hyperboloid and should be calculated separately.

Assuming a hyperboloidal shape as an approximation, its curvature is given by

$$K = \frac{(b_0 z/a_0)^2 - b_0^2 + (b_0^2 z/a_0^2)^2 + b_0^4/a_0^2}{[(b_0 z/a_0)^2 - b_0^2 + (b_0^2 z/a_0^2)^2]^{3/2}}. \tag{4.18}$$

Therefore the capillary pressure $p_\sigma = \sigma K$ at the tip and at a height H above the tip (see Fig. 4.2) is given by

$$p_\sigma|_{z=a_0} = \sigma \frac{2a_0}{b_0^2}, \tag{4.19a}$$

$$p_\sigma|_{z=H} = \sigma \frac{(b_0 H/a_0)^2 - b_0^2 + (b_0^2 H/a_0^2)^2 + b_0^4/a_0^2}{\left[(b_0 H/a_0)^2 - b_0^2 + (b_0^2 H/a_0^2)^{\,2}\right]^{3/2}}. \tag{4.19b}$$

Like in the first spheroidal approximation used in [41], we approximate the force balance at the hyperboloidal surface by the expressions

$$\sigma K|_{z=a_0} - \Delta p = \sigma_{nn}|_{z=a_0}\,, \tag{4.20a}$$

$$\sigma K|_{z=H} - \Delta p = \sigma_{nn}|_{z=H}\,. \tag{4.20b}$$

Assuming that Δp, the difference between the pressure inside and that outside the surface, is the same at the tip $z = a_0$ and "bottom" $z = H$, we obtain

$$\sigma_{nn}|_{z=a_0} - \sigma_{nn}|_{z=H} = \sigma K|_{z=a_0} - \sigma K|_{z=H}\,. \tag{4.21}$$

Substituting Eqs. (4.17) and (4.19) in Eq. (4.21), we find the dependence of φ_0 on the surface tension coefficient σ,

$$\frac{\varphi_0^2}{2\pi \ell n^2 \left[(1+\xi_0)/(1-\xi_0)\right]} \left[\left(\frac{\xi_0/a_0}{1-\xi_0^2} \right)^2 - \frac{1}{\left[(H/a_0)^2 - a_0^2\right]\,\left(1-\xi_0^2\right)} \right]$$
$$= \sigma \left(\frac{2a_0}{b_0^2} - \frac{(b_0 H/a_0)^2 - b_0^2 + \left(b_0^2 H/a_0^2\right)^2 + b_0^4/a_0^2}{\left[(b_0 H/a_0)^2 - b_0^2 + \left(b_0^2 H/a_0^2\right)^2\right]^{3/2}} \right). \tag{4.22}$$

Also from Eq. (4.11) we obtain

$$b_0^2 = a_0^2 \frac{(1-\xi_0^2)}{\xi_0^2}. \tag{4.23}$$

Substituting Eq. (4.23) in Eq. (4.22) and rendering Eq. (4.22) dimensionless, we rearrange it as follows

$$\frac{\varphi_0^2}{\sigma a_0} = 2\pi \ell n^2 \left(\frac{1+\xi_0}{1-\xi_0}\right) \left[2\xi_0^2 - \frac{\xi_0(1-\xi_0^2)^{1/2}\left[(\bar{H}^2+1)/\xi_0^2 - 2\right]}{\left[(\bar{H}/\xi_0)^2 - 1\right]^{3/2}}\right] \cdot \left\{\frac{\xi_0^2}{1-\xi_0^2} - \frac{1}{\left[(\bar{H}/\xi_0)^2 - 1\right]}\right\}^{-1}. \quad (4.24)$$

For a given $\bar{H} = H/a_0$ we obtain from expression (4.24) a dependence of $\varphi_0^2/(\sigma a_0)$ on ξ_0 for a stationary liquid body assumed to have a hyperboloidal shape. In the case of an "infinite" hyperboloid ($\bar{H} \gg 1$), with its tip at a distance a_0 from the equipotential surface $z = 0$, expression (4.24) yields

$$\varphi_0 = (\sigma a_0)^{1/2} (4\pi)^{1/2} \ell n \left(\frac{1+\xi_0}{1-\xi_0}\right) \left(1-\xi_0^2\right)^{1/2}, \quad (4.25)$$

which is analyzed in Sec. 4.3.

The temptation is to assign the equipotential surface $z = 0$ to the ground plate at $z_1 = 0$. This assignment is ruled out, because a_0 would then be much larger than the droplet size. Then the electric field adjoining the droplet (which is only a small detail of the practically uniform, capacitor-like field between the electrode and the ground, cf. Fig. 4.2(a)) would be grossly in error because this calculation does not account for the presence of the electrode at $z_1 = H_{ge}$. To eliminate this difficulty, we assume that the equipotential surface $z = 0$ is situated very close to the droplet tip, at a distance a_0, which is yet to be determined. The electric field between the matching boundary (cf. Fig. 4.2(b)) and the free surface of the droplet was already determined, and was described above.

The electric field between the matching boundary and the ground plate at distances from the tip much larger than a_0 is practically unaffected by the droplet. Thus the electric field in the region between the ground plate and the matching boundary may be assumed to be that of a parallel-plate capacitor (cf. Fig. 4.2(a)). The parallel-capacitor field and the field of the potential Φ found here in Sec. 4.2 (cf. Fig. 4.2(c)) are to be matched at $z = 0$, which enables us to calculate a_0 (cf. Fig. 4.2(b)). We can call the space between the surface $z = 0$ and the hyperboloid the boundary layer, which is characterized by the scale a_0. The space below $z = 0$ is then the "outer field" using a fluid-mechanical analogy. It is emphasized that this procedure is only a crude first

approximation, since the normal derivatives of the potentials (the electric field intensities) are not automatically matched at $z = 0$. A much better representation of the field and potential in the intermediate region could be achieved by matching asymptotic expansions or computer modelling. The region where the potential is not predicted with much precision is shown in gray in Fig. 4.2(b).

We now consider in detail matching of the approximate solutions for the electric potential. If z_1 is the coordinate directed from the ground plate (at $z_1 = 0$) toward the droplet, then the capacitor-like field is given by

$$\Phi = \frac{\Phi_0}{H_{ge}} z_1. \tag{4.26}$$

Here H_{ge} is the distance between the ground plate and an electrode attached to the droplet (at potential Φ_0).

Given that the droplet height in the z direction is H, that the borderline equipotential surface where $z = \xi = 0$ is situated at $z_1 = H_{ge} - H - a_0$, and matching the solutions for the potential, we find from Eqs. (4.9) and (4.26) that the constant in Eq. (4.9) is

$$\text{const} = \frac{\Phi_0}{H_{ge}}(H_{ge} - H - a_0). \tag{4.27}$$

Thus Eqs. (4.9) and (4.27) yield

$$\Phi = \varphi_0 \frac{\ell n\left[(1+\xi)/(1-\xi)\right]}{\ell n\left[(1+\xi_0)/(1-\xi_0)\right]} + \Phi_0 \frac{(H_{ge} - H - a_0)}{H_{ge}}. \tag{4.28}$$

For the droplet surface at $\xi = \xi_0$, the potential is $\Phi = \Phi_0$, and thus from Eq. (4.28) we find

$$\varphi_0 = \frac{\Phi_0}{H_{ge}}(H + a_0). \tag{4.29}$$

Combining Eq. (4.29) with Eq. (4.25), we obtain the equation for a_0

$$(\sigma a_0)^{1/2}(4\pi)^{1/2}\ell n\left(\frac{1+\xi_0}{1-\xi_0}\right)\left(1-\xi_0^2\right)^{1/2} = \frac{\Phi_0}{H_{ge}}(H + a_0), \tag{4.30}$$

which has two solutions. The solution relevant here reads

$$a_0 = \frac{1}{2}\left(\frac{1}{\beta^2} - 2H\right) - \left[\frac{1}{4}\left(\frac{1}{\beta^2} - 2H\right)^2 - H^2\right]^{1/2}, \tag{4.31a}$$

$$\beta = \frac{\Phi_0}{H_{ge}(4\pi\sigma)^{1/2}\ell n\left[(1+\xi_0)/(1-\xi_0)\right] \cdot \left(1-\xi_0^2\right)^{1/2}}, \tag{4.31b}$$

whereas the other one is irrelevant, since it yields $a_0 > H_{ge}$.

Expression (4.31a) permits calculation of a_0 for any given hyperboloidal droplet (given ξ_0 and H) at any given potential Φ_0. It should be noted that the results will be accurate if the calculated value of a_0 is sufficiently small relative to H.

4.3. Failure of the self-similarity assumption for hyperboloidal solutions

The electric potential between the free surface of a hyperboloidal liquid body and the equipotential surface z = 0 is given by Eq. (4.9) with φ_0 as per Eq. (4.25). To visualize the asymptotic behaviour of Eq. (4.9), we should follow a straight line with a constant slope θ, while R tends to infinity (see Fig. 4.1). Then using Eqs. (4.16) we find

$$R = (z^2 + \rho^2)^{1/2} = c(\eta^2 + \xi^2 - 1)^{1/2}. \tag{4.32}$$

Also

$$-\tan\theta = \frac{\rho}{z} = \frac{\left[(1-\xi^2)(\eta^2-1)\right]^{1/2}}{\eta\xi}, \tag{4.33}$$

which yields

$$\eta^2 = \frac{1-\xi^2}{1-(\xi/\cos\theta)^2}. \tag{4.34}$$

Substituting the latter in Eq. (4.32), we find

$$R = c\frac{\xi}{-\cos\theta}\left[\frac{1-\xi^2}{1-(\xi/\cos\theta)^2}\right]^{1/2}. \tag{4.35}$$

It is seen that $R \to \infty$ as $\xi \to -\cos\theta$. Then we obtain from Eqs. (4.9) and (4.25) the potential Φ as $R \to \infty$ in the following form

$$\Phi\,|_{R\to\infty} = (\sigma a_0)^{1/2}(4\pi)^{1/2}(1-\xi_0^2)^{1/2}\ell n\left(\frac{1-\cos\theta}{1+\cos\theta}\right) + \text{const}, \qquad \frac{\pi}{2} \leqslant \theta \leqslant \pi, \tag{4.36}$$

which shows that the asymptotic value, $\Phi\,|_{R\to\infty}$, is finite. Φ does not tend towards infinity as the self-similarity of Sec. 4.1 implies. Also, in spite of the fact that $R \gg a_0$, the dependence on a_0 does not disappear from Eq. (4.36) in contrast with the self-similar behaviour of Taylor's solution given by Eq. (4.3). We thus have here an example of a nonself-similar solution with a non-fading

influence of the value of a_0, even when $R \gg a_0$. Details of the shape of the tip at small distances of the order of a_0, affect the solution for Φ at any $R \gg a_0$. In other words, the solution for the field about a hyperboloid depends on the value of a_0 everywhere, while the field surrounding the Taylor cone does not depend on a_0 at $R \gg a_0$. The field surrounding the hyperboloidal bodies is always affected by the value of a_0, even when R approaches ∞. This behaviour is quite distinct from that of the boundary-layer theory cases of jets from a finite orifice and of plumes originating at a finite source, where the influence of the size of the orifice or source rapidly fades out.

The following observation should be mentioned. In the case of the parabolic governing equations (the boundary layer theory [42−44]), or the equation with a squared parabolic operator (the beam equation describing self-similar capillary waves [45]), self-similar solutions attract the nonself-similar ones and thus are realizable. On the other hand, in the present case the governing Laplace equation is elliptic, and its self-similar solution does not attract the nonself-similar one and therefore could hardly be expected to be realizable. Moreover, a similar phenomenon was found in the problem described by the biharmonic (the elliptic operator squared) equation, namely in the problem on a wedge under a concentrated couple. The later is known in the elasticity theory as the Sternberg-Koiter paradox [49].

The calculated cone, which is tangent to the critical hyperboloid just before a jet is ejected, is definitely not the Taylor cone. Indeed, in Fig. 4.3 the dependence of $\varphi_0/(\sigma a_0)^{1/2}$ on ξ_0 according to Eq. (4.25) is shown. The maximal potential at which a stationary shape can exist corresponds to $\xi_{0_*} = 0.834$ and $\varphi_{0_*} = 4.699(\sigma a_0)^{1/2}$. The value ξ_{0_*} corresponds to the critical hyperboloid. An envelope cone for any hyperboloid can be found using the derivative

$$\left.\frac{dz}{d\rho}\right|_{\rho\to\infty} = \frac{a_0}{b_0}, \tag{4.37}$$

which follows from Eq. (4.10).

For the critical hyperboloid, using Eq. (4.23), we find

$$\frac{a_0}{b_0} = \frac{\xi_{0_*}}{(1-\xi_{0_*}^2)^{1/2}} = 1.51. \tag{4.38}$$

Therefore the half angle at the tip of the cone is given by (cf. Fig. 4.1)

$$\alpha_* = \frac{\pi}{2} - \arctan(1.51), \tag{4.39}$$

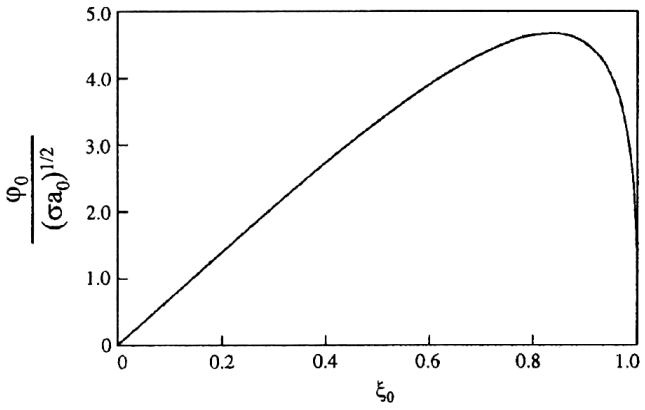

FIGURE 4.3. Dependence of the shape parameter ξ_0 on the electric potential φ_0 of an infinite hyperboloid.

which yields $\alpha_* = 33.5°$, which is significantly smaller than the angle for the Taylor cone $\alpha_T = 49.3°$. Note also that the Taylor cone is asymptotic to a hyperboloid possessing a value of $\xi = \xi_{0T}$ which should be less than ξ_*. Indeed, similar to Eq. (4.38)

$$\frac{a_{0T}}{b_{0T}} = \frac{\xi_{0T}}{(1-\xi_{0T}^2)^{1/2}} = \tan\left(\frac{\pi}{2} - \alpha_T\right), \tag{4.40}$$

which yields $\xi_{0T} = \cos\alpha_T = 0.65$. Comparing this value with that for the critical hyperboloid, $\xi_{0_*} = 0.834$, we see once more that the critical hyperboloid is much "sharper" than the one corresponding to the Taylor cone, since this sharpness increases with ξ.

The left part of the curve with a positive slope in Fig. 4.3 can be realized pointwise, since there higher potentials correspond to sharper hyperboloids. By contrast, the right-hand part represents still sharper hyperboloids for lower potentials, which cannot be reached in usual experiments with a stable fluid body. The latter means that the right-hand part corresponds to unstable solutions. It is also emphasized that the critical angle $\alpha_* = 33.5°$ is much closer to the experimental values reported in Sec. 4.4 than that of the Taylor cone.

The results of Secs. 4.2 and 4.3 are equally relevant for inviscid, for Newtonian, or for viscoelastic liquids after the stress has relaxed. All these manifest in stationary states with zero deviatoric stresses.

4.4. Experimental results and comparison with the theory

Two experiments, using sessile and pendant droplets, were performed for comparison with the theory. In the sessile drop experiment (Fig. 4.4) a droplet was created at the tip of an inverted pipette by forcing the liquid through the pipette slowly with a syringe pump. The liquid used was an aqueous solution of polyethylene oxide with a molecular weight of 400 000 and a weight concentration of 6%. Fluid properties of such solutions including shear and elongational viscosity, surface tension, and conductivity/resistivity are published elsewhere [24, 26, 27]. Their evaporation rate can be described using the standard dependence of saturation vapour concentration on temperature [27]. For droplet sizes of the order of 0.1 cm, the evaporation process lasts not less than 600 s [50]. This is much more than the time required to reach steady state and make measurements (of the order of 1 s). Therefore evaporation effects when the photographs were taken are negligible. All the experiments were done at room temperature. Elevated temperatures were not studied. Droplet configurations are quite reproducible for a given capillary size, which was not varied in the present experiments. The effect of pH was not studied in detail. Addition of sodium chloride to the solution was discussed in [24]. The electrode material, usually copper, had no important effect on the ionic conductivity of the solutions [24, 26, 27].

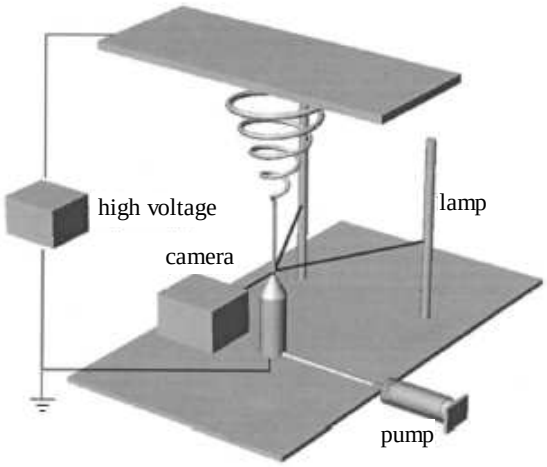

FIGURE 4.4. Sessile drop experiment.

The electric potential was applied between the droplet and a flat metal collector plate held above the droplet. The droplet was kept at ground potential for convenience. The potential difference was increased in steps of about 200 V, each step a few seconds long, until a jet formed at the tip of the droplet. Images of the droplet were made with a video camera. The shape of the droplet during the step that preceded the formation of the jet was called the critical shape. Two linear lamps were mounted vertically, behind and on either side of the droplet. The shape and diameter of the droplet were demarcated by reflection of the lights, seen as white line on the image recorded by the video camera. Diffuse back lighting was used for the pendant drop (Fig. 4.5).

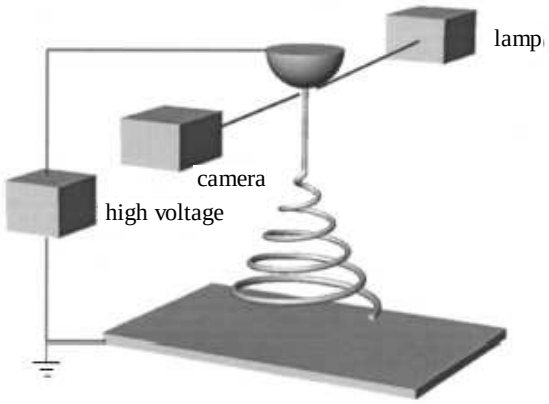

FIGURE 4.5. Pendant drop experiment.

The drops were photographed at a rate of 30 frames per second. The observed shape of the droplet is compared with the calculated shape in Fig. 4.6(a).

In the pendant droplet experiment (Fig. 4.5) the polymer solution was placed in a spoon with a 1 mm hole in its bowl. The potential was applied between the drop and a flat plate. The experimental result is shown in Fig. 4.6(b).

The sessile droplet, which was attracted towards a flat electrode at a distance $H_{ge} = 13\,\mathrm{cm}$, became critical at the potential $\Phi_0 = 19.34\,\mathrm{kV} = 64.47\,(\mathrm{g{\cdot}cm})^{1/2}/\mathrm{s}$. The drop had a height of $H = 0.128\,\mathrm{cm}$. When Φ_0 was slightly increased by a step of about 200 V, a jet emerged from the top of the droplet. Using these data, as well as $\xi_0 = \xi_{0*} = 0.834$ (cf. Sec. 4.3), and

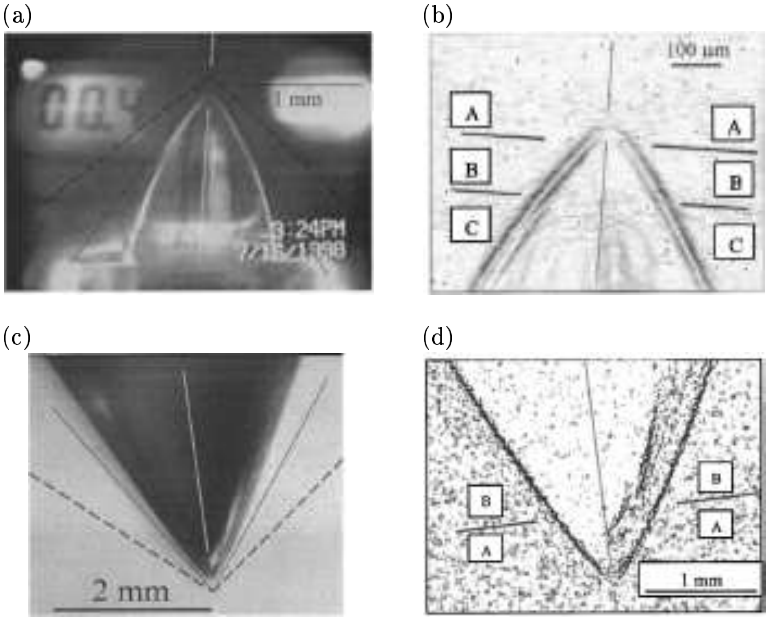

FIGURE 4.6. (a) Videograph of the critical droplet shape observed for a sessile droplet. The bottom of the drop was constrained to the inner diameter of the pipette on which it sat. The drop is symmetrical about the white line. The symmetry axis is not exactly vertical due to camera tilt, the tilt of the pipette, and the tilt of the electric field direction. The half angles predicted in this section are indicated by the solid lines. The half angle associated with the Taylor cone is indicated by the dashed lines. This image was not enhanced or cropped. The outlines of the pipette can be seen at the bottom, and information on the experimental parameters is visible in the background. (b) Part of the image in (a), processed with Scion Image "Find Edges" (`http://www.scioncorp.com/`). No useful data about the location of the edge were found in region A. Lines tangent to the boundary segments in region B indicate a half angle of 37.5°. Lines tangent to the boundary segments in region C indicate a half angle of 30.5°. The lower parts of the boundary were not used because they were constrained by the pipette. (c) Critical droplet shape observed for a pendant drop. (d) Part of the image in (c). The enlarged droplet tip from (c), processed with Scion Image "Find Edges". Lines tangent to the boundary segments in region A indicate a half angle of 31°. Lines tangent to the boundary segments in region B indicate a half angle of 26°.

taking $\sigma = 70\,\mathrm{g/s^2}$, the value of a_0 was found from Eq. (4.31) to be $a_0 = 0.00026\,\mathrm{cm}$. Since the value of a_0 is much smaller than H, the hyperboloidal approximation not accounting for perturbations due to the electrode, is self-consistent and satisfactory (see earlier discussion near the end of Sec. 4.2).

The pendant droplet became critical at the potential $\Phi_0 = 19.5\,\mathrm{kV} = 65.6\,(\mathrm{g{\cdot}cm})^{1/2}/\mathrm{s}$ at $H_{ge} = 17.3\,\mathrm{cm}$ (see Fig. 4.6(b)). The height of the droplet was $H = 0.30\,\mathrm{cm}$. The value of a_0 was found to be $0.00021\,\mathrm{cm}$, which is also sufficiently small relative to H. The corresponding value of the potential difference between the droplet and the equipotential surface at the matching boundary is $\varphi_{0*} = 4.699(\sigma a_0)^{1/2} = 0.57\,(\mathrm{g{\cdot}cm})^{1/2}/\mathrm{s} = 171\,\mathrm{V}$.

The hyperboloids calculated using Eqs. (4.10) and (4.25) approach the conical asymptotes with a half-angle of $\alpha_* = 33.5°$, which are shown by the solid lines in Fig. 4.6. Cones with a half-angle of $\alpha_T = 49.3°$, which is characteristic of the Taylor cone, are shown in Fig. 4.6 by dashed lines. The half-angle at the tip shown in the photographs of Figs. 4.6(a) and 4.6(b) in region C, where the influence of the pipette is small, is 30.5°. Even closer to the tip in region B an observed half-angle is 37.5°. Both these angles are closer to the hyperboloidal solution (33.5°) than to the Taylor solution (49.3°). Calculation predicts that the hyperboloid approaches within $5\,\mu\mathrm{m}$ of the intersection of the asymptotes, but there is not enough resolution in the images that this can be seen. Half-angles were measured, as shown in Fig. 4.6. For the sessile drop the measured half-angle near the tip in region B was 37.5° and in region C it was 30.5°. For the pendant drop the measured half-angle near the tip in region A was 31° and in region B it was 26°. All these angles are closer to the hyperboloidal solution than to the Taylor cone.

Note also that the electrode used in the experiments was submerged in the liquid inside the pipette so the influence of the actual electrode on the shape of the droplet is minimal. The lower part of the droplet shown in Fig. 4.6(a), is also affected mechanically by the pipette wall, which restricts the diameter of the base of the droplet. That is the reason why the free surface deviates from the predicted solid line in Fig. 4.6(a) near the bottom.

It should be mentioned that in [51] it was stated that according to experimental data, a stable cone can be obtained for a range of angles, but typically the half-angle was close to 45°. Both Taylor [41] and Michelson [51] worked with low molecular weight liquids, which are prone to perturbations and atomization. These perturbations might lead to premature jetting before a true critical shape can be achieved. This can explain the larger (and varying) values of α recorded in the experiments of [41] and [51].

In [52] critical configurations of liquid droplets affected by the electric field in a parallel capacitor were calculated numerically using the boundary element method. One of the arrangements considered, the initially hemispher-

ical droplet supported by an electrode, is close to the experimental situation in the present work. The numerical predictions for this case (Fig. 42 of [52]) showed that the apparent cone angle is less than or about 40°, which is closer to the critical angle $\alpha_* = 33.5°$ predicted in the present work than to $\alpha_T = 49.3°$.

The numerically predicted value of the half-angle of the calculated shape, which is significantly less than 49.3°, may be an indication of failure of the self-similarity assumption, similar to what was discussed in Sec. 4.3. However, due to inaccuracies intrinsic in numerical methods in cases in which a singularity is formed, a definite statement cannot be made. According to [53], in which both boundary and finite element calculations related to the present problem were characterized, "all the numerical studies either assume a rounded end and/or cannot resolve the structure in the neighborhood of a nearly pointed end". As usual, close to singularities, insight can be gained by approximate models, for example, the slender body approximation [53–55], or the hyperboloidal approximation of the present work.

A recent attempt [56] to simulate numerically dynamics of Taylor cone formation revealed the following. In one of the two cases considered, the free surface developed a protrusion, which did not approach a cone-like shape before the calculations were stopped. In the second case, a cone-like structure with a half-angle of about 50.5° was achieved after the calculations were started from a very large initial perturbation. It should be mentioned that the generatrix of the initial perturbation was assumed to be given by the Gaussian function, and liquid was assumed to be at rest. These assumptions are arbitrary and non-self-consistent. Also, the assumed initial shape was far from a spherical droplet relevant within the context of polymeric fluids. Moreover, the value assumed for the electric field was chosen arbitrarily and could have exceeded the critical electric field for a stationary Taylor cone. All this makes the results inconclusive and shows that the dynamic theory of Taylor cone formation deserves further effort.

It is emphasized that the present work, following that of Taylor [41], assumes the liquid in the droplet to be a perfect conductor. In a number of works, cases where liquid in the drop is an insulator, were considered [53, 55, 57]. Two self-similar conical solutions with half-angles of $0° \leqslant \alpha_* \leqslant 49.3°$ exist when the ratio of the dielectric constants is in the range of $17.59 \leqslant \varepsilon_d/\varepsilon_s \leqslant \infty$, where ε_d corresponds to the droplet, and ε_s corresponds to a surrounding fluid (the ratio $\varepsilon_d/\varepsilon_s = \infty$ corresponds to the fully conductive

droplet). For $\varepsilon_d/\varepsilon_s < 17.59$ equilibrium conical solutions do not exist. Deviation of the experimental half angles to values significantly below 49.3° can, in principle, be attributed to one of the two solutions for the range of $\varepsilon_d/\varepsilon_s$ where two solutions exist. The choice between these solutions based on the stability argument leads to the rather puzzling outcome that the Taylor cone branch is unstable, and that very small half angles should be taken in contradiction to experiments [53, 55]. However, the assumption that liquids could be considered as insulators actually holds only on time scales shorter than the charge relaxation times, $\tau_H < \tau_C$. The latter are of the order of $10^{-10} \div 10^{-3}$ s according to the estimates of [57] and in Sec. 4.1. Since in our experiments the residence time of a liquid in the cone, $\tau_H = 1$ s, is much longer than the charge relaxation time, conductivity effects should dominate the dielectric effects [57]. In insulating dielectric liquids, due to non zero electric shear stress at the cone surface, flow is inevitable inside the droplet [57]. In the experiments of the present work such a flow was not seen. The absence of such a flow is consistent with the fact that the behaviour of the polymer solutions could be closely approximated by that of a perfectly conductive liquid, as was assumed.

It is of interest to estimate the radius of curvature r at the tip at the potential which corresponds to the onset of instability. From Eq. (4.19a), we have $r = b_0^2/2a_0$. Using Eq. (4.23) we find

$$r = a_0 \frac{(1-\xi_0^2)}{2\xi_0^2}. \tag{4.41}$$

Substituting here $\xi_0 = 0.834$ and $a_0 = 0.00026$ cm, which are the values found above, we find $r = 5.69 \times 10^{-5}$ cm, which is near the wavelength of light and is too small to be seen in an ordinary photograph. Dimensions of polymer molecules, such as the radius of gyration in the solution, are typically around $10\ nm(10^{-6}cm)$, and therefore can be neglected.

In a group of works related to the development of pure liquid alloy ion sources (LAIS) [58–60] several additional physical processes, which may be relevant within the context of Taylor cone formation, were revealed. The most important of them is field evaporation of metal ions from the tip of the cone leading to the emergence of ion emission currents and space charge. These phenomena are totally irrelevant in the present context for the following reasons. According to [58–60] field evaporation is impossible unless a jet-like protrusion is formed on top of the Taylor cone. The characteristic radius of

curvature of the protruding tip should be of the order of 1-1.5 nm, and the corresponding field strength of the order of 1.5×10^5 kV/cm. These conditions could never be realized in the electrospinning experiments. In the present case, unlike in LAIS, the huge fields needed for field evaporation could not even be approached. Moreover, the apex temperatures corresponding to field evaporation and the accompanying effects are of the order of 600-1000°C according to [59]. Such temperatures would produce drastic chemical changes in a polymer solution.

In the course of the present work space charge and electrical currents in the air were occasionally measured. It was shown that the occurrence of these phenomena was always a consequence of corona discharge, and could always be reduced to a very low level. All the above taken together allows us to conclude that field evaporation and ion current effects on the half angle of the observed cones can be totally disregarded.

For low viscosity liquids, as already mentioned, tiny droplets can easily be emitted from the cone tip. Sometimes droplet emission begins at α_* close to 45° [51], sometimes close to 49° [61]. It should be emphasized that single tiny protrusions, jets, and droplets of submicron size at the top of the Taylor cone are invisible in ordinary photographs. It is difficult to judge when the jet emerges since the cone tip may oscillate as each droplet separates. At higher voltage, atomization of the cone tip can lead to significant space charge from the electrically charged droplets emitted. In [61] it was shown that the backward electric effect of the charged droplets on the tip of the cone leads to reduction of its half-angle to a range of $32° < \alpha_* < 46°$. For the highly viscoelastic liquids we are dealing with in the present work, atomization is virtually impossible. Breakup of tiny polymer jets, threads, and filaments is always prevented by viscoelastic effects and the huge elongational viscosity associated with them [26, 27, 62, 63]. Therefore, it is highly improbable that the reduced values of the half-angle α_* found in the present experiments can be attributed to a space charge effect similar to that in [61].

When the critical potential for static cone formation is exceeded, jetting begins from the tip. In the relevant case of polymer solutions the jets are stable to capillary perturbations, but are subject to bending instability, which is usually observed in the electrospinning process (see Chapter 5). On the other hand, in the case of low viscosity liquids or removal of the charge [24], the jets are subject to capillary instability [41], which sometimes leads to an almost immediate disappearance of the jet [61]. Sometimes, however, in

the case of bending or capillary instability a visible, almost straight section of a jet exists, where the growing perturbations are still very small. Therefore it is of interest to describe the jet profile corresponding to the almost straight section. This is typically done within the framework of the quasi-one-dimensional equations of dynamics of free liquid jets [26, 62, 64–67]. In [66] and [67] such a solution for the jet was also matched with a conical semi-infinite meniscus using the method of matched asymptotic expansions. As a basic approximation for the droplet shape, a Taylor cone of $\alpha_T = 49.3°$ was chosen. In light of the present results a similar calculation is worth doing for an almost conical hyperboloidal droplet with $\alpha_* = 33.5°$.

4.5. Summary

The hyperboloidal approximation employed permits prediction of the stationary critical shapes of drops of inviscid, Newtonian and viscoelastic liquids. It was shown, both theoretically and experimentally, that as a liquid surface develops a critical shape, its configuration approaches the shape of a cone with a half angle of 33.5°, rather than a Taylor cone of 49.3°.

The critical half angle does not depend on fluid properties, since an increase in surface tension is always accompanied by an increase in the critical electric field.

Chapter 5

Bending instability of electrically charged liquid jets of polymer solutions in electrospinning [1)]

In the present section the physical mechanism of the electrospinning process is explained and described. It is shown that the longitudinal stress caused by the external electric field acting on the charge carried by the jet stabilizes the straight jet for some distance. Then a lateral perturbation grows in response to the repulsive forces between adjacent elements of charge carried by the jet. This is the key physical element of the electrospinning process responsible for enormously strong stretching and formation of nanofibers. A localized approximation is developed to calculate the bending electric force acting on an electrified polymer jet. Using this force, a far-reaching analogy between the electrically driven bending instability and the aerodynamically driven instability was established. Continuous, quasi-one-dimensional, partial differential equations are derived and used to predict the growth rate of small electrically driven bending perturbations of a liquid column. A discretized form of these equations, that accounts for solvent evaporation and polymer solidification, is used to calculate the jet paths during the course of nonlinear bending instability leading to formation of large loops and resulting in nanofibers. The results of the calculations are compared to the experimental data. The mathematical model provides a reasonable representation of the

[1)] The results presented in this section were published by D.H. Reneker, A.L. Yarin, H. Fong and S. Koombhongse in [26] and by A.L. Yarin, S. Koombhongse and D.H. Reneker in [27].

experimental data, particularly of the jet paths determined from high-speed videographic observations.

In Sec. 5.1 the experimental electrospinning set-up is described. The experimental observations are presented in Sec. 5.2. In Sec. 5.3 a model of the rectilinear part of the electrified jet is presented. The basic physics of bending instability in electrospinning is explained in Sec. 5.4. Localized approximation for calculation of electrostatic repulsive forces in bending instability is introduced in Sec. 5.5. Using it, the continuous quasi-one-dimensional equations of the dynamics of electrified jets are introduced in Sec. 5.6, and the corresponding discretized equations – in Sec. 5.7. Solvent evaporation and jet solidification are incorporated in the model in Sec. 5.8. Growth rate and wavelength of small bending perturbations of an electrified liquid column are discussed in Sec. 5.9. Nonlinear dynamics of bending and looping in electro-

TABLE 5.1. Symbols employed and their definitions.

Symbol	**Definition**	**Unit** (cgs)
a	Cross-sectional radius	cm
a_0	Initial cross-sectional radius	cm
e	Charge	$\mathrm{g}^{1/2}\mathrm{cm}^{3/2}/\mathrm{s}$
f_a	Air friction force per unit length	$\mathrm{g/s}^2$
f_g	Gravity force per unit length	$\mathrm{g/s}^2$
G	Elastic modulus	$\mathrm{g/(cm\,s}^2)$
h	Distance from pendant drop to grounded collector	cm
L	Length scale, $L = (e^2/\pi a_0^2 G)^{1/2}$	cm
L_Z	Length of the straight segment	cm
ℓ	Length of the ideal rectilinear jet	cm
m	Mass	g
t	Time	s
v	Velocity	cm/s
V_0	Voltage	$\mathrm{g}^{1/2}\mathrm{cm}^{1/2}/\mathrm{s}$
W	Absolute value of velocity	cm/s
ζ	Initial segment length	cm
λ	Perturbation wavelength	cm
μ	Viscosity	$\mathrm{g/(cm\,s)}$
ν	Kinematic viscosity	cm^2/s
σ	Surface tension	$\mathrm{g/s}^2$
σ_{ij}	Stress	$\mathrm{g/(cm\,s}^2)$
ρ	Density	$\mathrm{g/cm}^3$
ρ_a	Air density	$\mathrm{g/cm}^3$
θ	Relaxation time $(= \mu/G)$	s
ω	Frequency of the perturbation	s^{-1}

spinning predicted theoretically is discussed and compared to the experimental data in Sec. 5.10. Conclusions are drawn in Sec. 5.11.

The international system of units (Système International (SI)) is used to report the values of experimental measurements. Gaussian units that are customary in fluid mechanics and electrostatics have also been used, as well as dimensionless combinations of parameters to provide concise coverage of the multidimensional parameter space. The numerical results from the calculations were converted to SI units for comparison with the experimental observations. Table 5.1 of symbols and Table 5.2 of dimensionless groups of parameters are provided.

Table 5.2. Dimensionless groups and parameters employed and their definitions.

Symbol	**Dimensionless group**	**Dimensionless parameter**	**Definition**
A	Surface tension		$\frac{\sigma\,\pi\,a_0^2\,\mu^2}{m\,L_{e\ell}^2\,G^2}$
H	Distance from pendant drop to grounded collector		$\frac{h}{L_{e\ell}}$
K_s	Perturbation frequency		$\frac{\omega\,\mu}{G}$
Q	Charge		$\frac{e^2\mu^2}{L_{e\ell}^3\,m\,G^2}$
V	Voltage		$\frac{e\,V_0\,\mu^2}{h\,L_{e\ell}\,m\,G^2}$
F_{ve}	Elastic modulus		$\frac{\pi\,a_0^2\,\mu^2}{m\,L_{e\ell}\,G}$
$\bar{t}$		Time	$\frac{t}{\mu/G}$
$\bar{W}$		Absolute value of velocity	$\frac{W}{L_{e\ell}\,G/\mu}$
$\bar{\ell}$		Length of the rectilinear part of the jet	$\frac{\ell}{L_{e\ell}}$
$\bar{v}$		Velocity	$\frac{v}{L_{e\ell}\,G/\mu}$
$\bar{\sigma}_{ij}$		Stress	$\frac{\sigma_{ij}}{G}$

5.1. Experimental set-up for electrospinning

Figure 5.1 is a sketch of the experimental apparatus. In this section, words such as up, down, top and bottom, are used to simplify the description of the experimental arrangements and the observations. The jet flowed downwards from the surface of a pendant drop of fluid towards a collector at the distance h below the droplet. An electrical potential difference, which was around 20 kV, was established between the surface of the liquid drop and the collector. The distance, h, was around 0.2 m. The nanofibers formed a mat on the collector. The coordinates used in the mathematical description are also shown. A magnified segment of the jet near the top of the envelope cone shows the electrical forces that cause the growth of the bending instability. These forces are described in detail in Sec. 5.4 and Fig. 5.12.

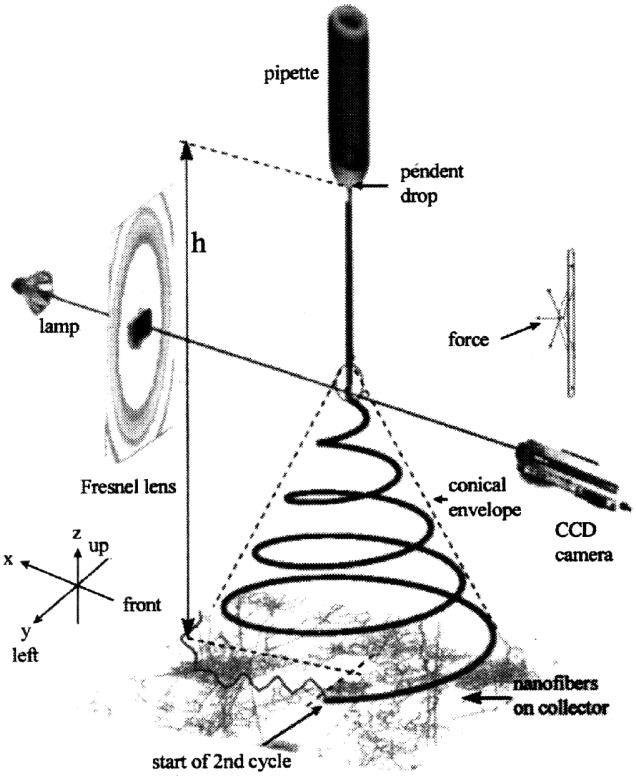

FIGURE 5.1. Schematic drawing of the electrospinning process, showing the jet path, reference axes, relative arrangement of parts of the apparatus at different scales, and the region where the bending instability grew rapidly.

In general, the pendant drop may be replaced by other fluid surfaces such as films on a solid or shapes generated by surface tension and flow. The collector is usually a good electric conductor. The charged nanofibers may be collected on an insulator, although a way to neutralize the charge carried by nanofibers must be provided in order to collect many layers of nanofibers. Airborne ions from a corona discharge provide an effective way to neutralize the charge on the jets and on the nanofibers. Nanofibers may also be collected on the surface of a liquid.

Experiments on electrospinning [22, 24] typically use set-ups similar to that sketched in Fig. 5.1. All experiments were performed at room temperature, which was about 20°C. Polyethylene oxide with a molecular weight of 400 000, at a weight concentration of 6%, was dissolved in a mixture of around 60% water and 40% ethanol. Fresher solutions produced jets that travelled further before the first bending instability appeared. The solution was held in a glass pipette with an internal diameter of about 1 mm. At the beginning of the experiment, a pendant droplet of polymer solution was supported at the tip of the capillary. The liquid jet formed on the surface of the pendant drop of solution. When the electrical potential difference (measured in volts, and often referred to as the applied voltage) between the capillary and the grounded collector is increased, the surface of the liquid becomes charged by the electrical field induced migration of ions through the liquid. Instability of the droplet set in when the potential difference was high enough that electrical forces overcame the forces associated with surface tension (cf. Chapter 4). Above this threshold, a stable liquid jet emerged. The jet carried away excess ions that migrated to the surface when the potential was applied. A higher potential difference created a higher charge on the jet. For low conductivity solutions, a significant time may be required for the charge to reach a saturation value after the applied potential changes, since charge transport within the fluid is limited by the finite mobility of the ions.

A region about 5 mm across near the vertex of the envelope cone was imaged with a lens that had a focal length of 86 mm and an f number of 1.0. The lens was placed about 20 cm from the jet to avoid disturbing the electrical field near the jet. The image produced by this lens was observed using a 12.5-75 mm, f 1.8 zoom lens on an electronic camera that recorded up to 2000 frames per second with exposure times as short as 0.0125 ms, although the exposure times used in this work were longer.

The light source was a 50 W halogen lamp with a faceted parabolic reflector. A Fresnel condenser lens was used to project an image of the halogen lamp and its reflector onto the region occupied by the cone. The Fresnel lens had a focal length of 19 cm and a diameter of 30 cm. The central 15 cm diameter part of the Fresnel lens was covered so that the camera received the light scattered from the jet superimposed upon the dark background produced by the covered part of the Fresnel lens.

Images for stereographic viewing were obtained by removing the 86 mm lens, which reduced the magnification so that a region about 1 cm wide is shown in each image in Fig. 5.2. A pair of wedge prisms that were 40 mm high and 55 mm wide were placed about 20 cm in front of the jet. Each prism deflected the light beam that passed through it by 5°. The zoom lens on the electronic camera, viewing the jet through the two prisms, produced side by side images of the jet from two directions that were 10° apart on each frame that was recorded. These paired images were viewed stereoscopically during playback to produce a slowed down, three-dimensional image of the moving jet. Image processing and analysis was done with *Adobe Photoshop*, *Corell Photopaint* and the software supplied with the electronic camera.

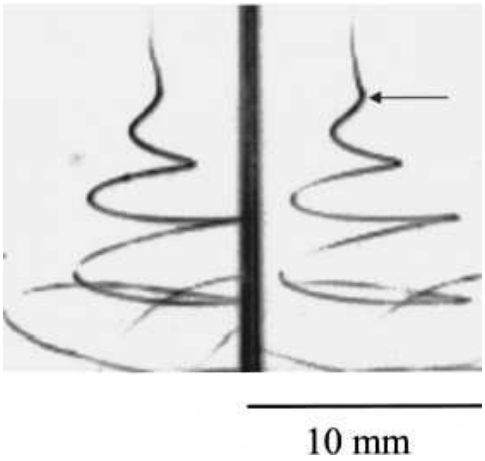

FIGURE 5.2. Stereographic images of an electrically driven bending instability. The exposure time was 0.25 ms. The arrow marks a maximum lateral excursion of a loop.

5.2. Experimental observations

5.2.1. Jet paths

The region near the vertex of the envelope cone was imaged at 2000 frames per second. These images showed the time evolution of the shape of the jet clearly and in detail. Stereographic images such as those in Fig. 5.2 showed the shape in three dimensions. The expanding spiral in Fig. 5.2 is a simple example of the kinds of paths that were observed. After a short sequence of unstable bending back and forth, with growing amplitude, the jet followed a bending, winding, spiraling and looping path in three dimensions. The jet in each loop grew longer and thinner as the loop diameter and circumference increased. Some jets, which are shown in Figs. 5.3-5.5, drifted downwards at a velocity much slower than the downward velocity of the smaller loops close to the vertex of the envelope cone. After some time, segments of a loop suddenly developed a new bending instability, similar to, but at a smaller scale than, the first. Each cycle of bending instability can be described in three steps.

Step 1. A smooth segment that was straight or slightly curved suddenly developed an array of bends.

Step 2. The segment of the jet in each bend elongated and the array of bends became a series of spiraling loops with growing diameters.

Step 3. As the perimeter of the loops increased, the cross-sectional diameter of the jet forming the loop grew smaller; the conditions for step (1) were established on a smaller scale, and the next cycle of bending instability began.

This cycle of instability was observed to repeat at an even smaller scale. It was inferred that more cycles occur, reducing the jet diameter even more and creating nanofibers. After the second cycle, the axis of a particular segment may point in any direction. The fluid jet solidified as it dried and electrospun nanofibers were collected some distance below the envelope cone.

The vector sum of forces from the externally applied field, the charge momentarily held in space by the jet, and air drag caused the charged segments to drift towards the collector. Except for the creation of the pendant droplet, the electrospinning process discussed in this section depends only slightly on the gravity force.

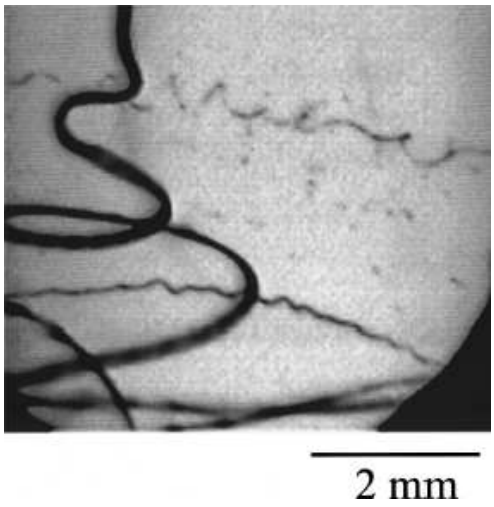

FIGURE 5.3. Image of the end of the straight segment of the jet. The exposure time was 0.25 ms.

Figure 5.3 shows the jet entering the upper left corner, near the end of the straight segment of a jet, and the vertex of the envelope cone, where the first bending instability grew. Several segments of the jet are shown, including segments from slow moving loops that formed earlier. All these segments are connected by segments that are not shown. Two smooth segments cross each other in this image as they run nearly horizontally across the bottom of the image. These two segments are noticeably thinner than the jet entering the image because the jet elongated as time evolved. These slow moving segments were a part of large loops and were affected both by air drag and by the disturbance of the applied electrical field caused by the presence of both charged segments of the jet and charged nanofibers below the region being observed. Such slow moving segments remained in view for many frames.

Two thinner segments that formed even earlier are also included in Fig. 5.3. One runs across the top half of the image, and the other runs across the bottom half. In the lower of these segments, the successive bends (step (1) of the second cycle) were apparent. In the upper segments, the bends had already developed into spiraling loops (step (2) of the second cycle). The pattern of dots visible in the lower left corners of Figs. 5.3-5.5 was caused by the pattern of facets or the reflector of the halogen lamp used to illuminate this experiment. These dots are not evidence of the familiar varicose instability that

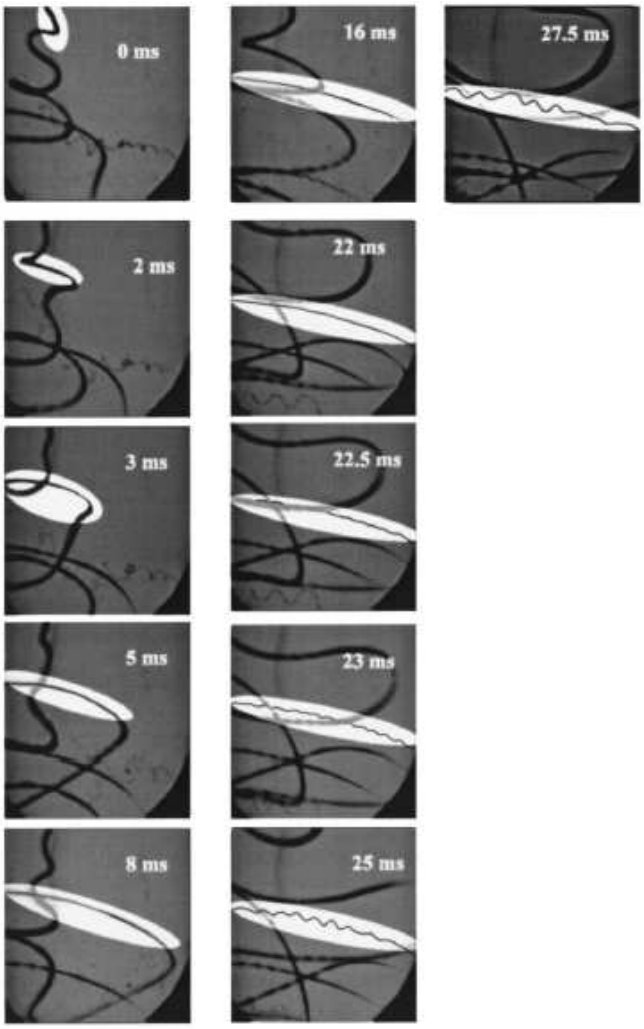

FIGURE 5.4. Evolution of electrical bending instability. The exposure times were 0.25 ms. The width of each image was 5 mm.

may cause a liquid jet to become a series of droplets. No varicose instability was observed in this experiment.

Using a set of image files created by the electronic camera it was often possible to follow the evolution of the shape of spiraling segments, such as those shown in Fig. 5.3, back to the straight segment that entered the upper left hand corner of the image. In Figs. 5.4 and 5.5, the light ellipse in the first image marks a segment that evolved in an interesting way. The selected

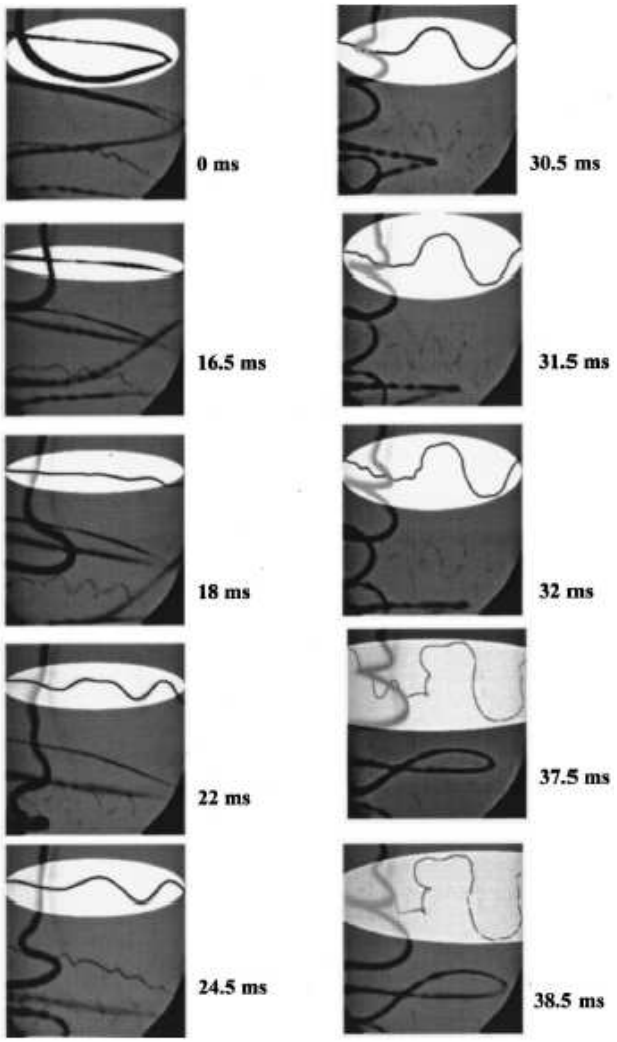

FIGURE 5.5. Images of secondary and tertiary cycles of bending instabilities. The exposure time was 0.25 ms. The width of each image is 5 mm.

segment of the jet was followed forward in time, from the moment it entered the region contained in the images until it elongated, looped, became unstable, bent, entered the next cycle, and ultimately became too thin to form an image.

Figure 5.4 starts with a bend near the end of the straight segment of a jet entering the image at the upper left. The onset of the electrically driven bending instability occurred just before the jet entered the image. The straight

segment of the jet extended upward, and is not shown. The segment of the jet that is highlighted by the white ellipse was followed for 27.5 ms in a series of images that were recorded at 0.5 ms intervals. The thinner segments of the jet were emphasized by using the Photopaint 6 software to reproduce them. Places where the faint image of the jet was ambiguous are indicated by dots, seen, for example, in the image at 22.5 ms.

Eleven images were selected from this series of 55 images to show the evolution of the highlighted segment. The time intervals between the images that are shown vary. Many images that show only a gradual evolution of the path were omitted to simplify Fig. 5.4. The time at which the first image was captured is taken as time zero. The elapsed time at which each of the following images was recorded is given in Fig. 5.4.

The looping segment being observed at zero time elongated for 10 ms in Fig. 5.4. Its further elongation was not followed, because the loop had extended entirely across the image. The rate of increase in the length of the highlighted segment was around 120 mm/s. After 22 ms the visible part of the highlighted segment still appeared in Fig. 5.4 as a smooth, slightly curved line. In the short time interval between 22.0 and 22.5 ms, this long, slightly curved smooth segment suddenly became instable. A linear array of bends appeared, marking the beginning of the second cycle. The lateral amplitude of the bends grew to about 1 mm, and the spatial period of the bends along the segment was also about 1 mm.

These smaller bent segments of the jet continued to elongate, but the images of the trajectories grew fainter and soon were ambiguous. The elongation and the associated thinning presumably continued as long as the charge on the jet supplied enough force. Meanwhile, the elongational viscosity increased as the jet dried. Eventually the jet solidified and the elongation stopped. The evolution of the solidification process remains to be investigated.

The first image in Fig. 5.5 shows a selected segment that was tracked back to the highlighted area near the bottom of the straight segment. This loop grew in diameter as the jet elongated and became thinner. After 18 ms, an array of bends that had a relatively long wavelength developed. These bends evolved gradually to the path shown at 30.5 ms. Then a tertiary array of bends developed on the highlighted segment during the next 0.5 ms, and quickly evolved to the path shown at 31.5 ms. The growth of the tertiary excursions was followed until 38.5 ms after the first image, at which point the jet was so thin that its image could no longer be followed.

5.2.2. Jet splaying

The circled region in Fig. 5.6 shows a jet that split into two jets that splayed apart, with the axis of the thinner branch generally perpendicular to the axis of the primary jet. The thinner jet disappeared in a few milliseconds, in some cases because it rapidly became even thinner, and in other cases because its path left the field of view. No bending instability was observed on the thinner segment, probably because it was not observed long enough for an instability to develop. Only a few such events were observed in the thousands of images of polyethylene oxide solution examined.

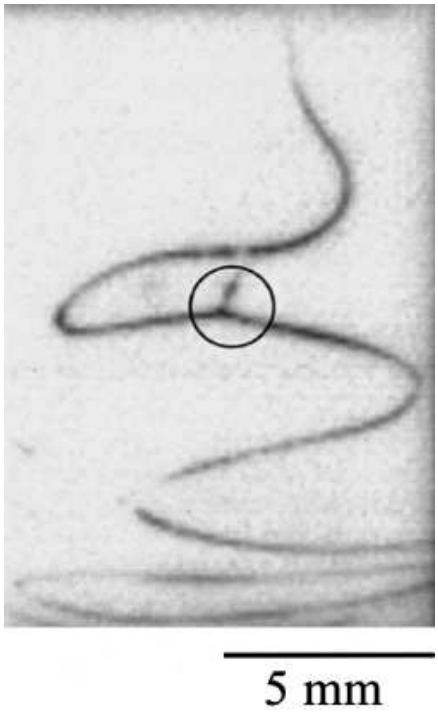

FIGURE 5.6. A jet splits off the primary jet and splays to a different direction.

Before the high frame rate, short exposure time images of Figs. 5.4 and 5.5 were available, visual observations and video images of electrically driven jets were interpreted as evidence of a process that splayed the primary jet into many smaller jets. The smaller jets were supposed to emerge from the region just below the apex of the envelope cone. Figure 5.7(a) shows an image from a video frame with an exposure of 16.7 ms. The envelope cone was illuminated

with a single bright halogen lamp that projected a narrow beam through the envelope cone, towards, but not directly into, the lens, so that most of the light that entered the video camera was scattered from the jets.

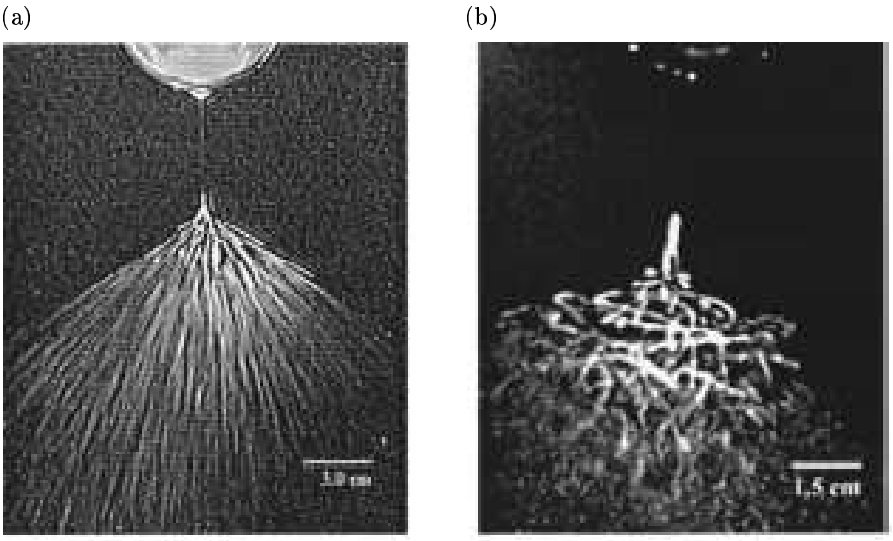

FIGURE 5.7. Images of electrospinning jet with longer camera exposure times: (a) 16.7 ms, (b) 1.0 ms.

Figure 5.7(b) shows a jet similar to that shown in Fig. 5.7(a) that was illuminated with light from two halogen lamps and photographed with a video camera. The two lamps were above and behind the jet. One was to the left and the other to the right. This provided a broader source of illumination than that used for Fig. 5.7(a), but not as uniform as the Fresnel lens arrangement shown in Fig. 5.1. An exposure time of 1 ms was used. The part of the straight jet with small bending amplitude is visible as are the loops containing segments, which had turned so that the axis of the segment formed a high angle with the axis of the straight segment. The parts of the jet nearer the vertex of the envelope cone appeared only as short, unconnected lines. Spectacular reflections of the beam of light, called glints, from one or the other of the two halogen lamps off nearly horizontal segments of downward moving loops, were shown to be the cause of these bright spots. Similar bright spots moved downwards during the longer exposure of Fig. 5.7(a), and created the lines that are prominent in Fig. 5.7(a).

The video frame rate of 30 frames per second was not fast enough to follow the smooth development of the jet path. At this frame rate, for any particular frame, the preceding and the following frames showed loops and spirals in completely different positions. Only after the illumination was improved, described in Sec. 5.1, and the high frame rate electronic camera used, was it obvious that the envelope cone was occupied by one long, flowing, continuous, and ever thinner jet. The repeated cycles of ever smaller electrically driven bending instabilities created a complex path in which the directions of the axes of the connected segments were often different and changing, sometimes by large angles.

5.2.3. Coiled and looped jets captured on a hard surface

Nanofibers were sometimes collected by moving a glass microscope slide, a metal screen, or other solid surfaces through the conical envelope. Figure 5.8 shows that coiled and looped nanofibers collected in this way were similar in shape to the bending instabilities photographed with the high-speed camera. The abundance and single coil of the coiled loops depended on the distance below the vertex at which they were collected.

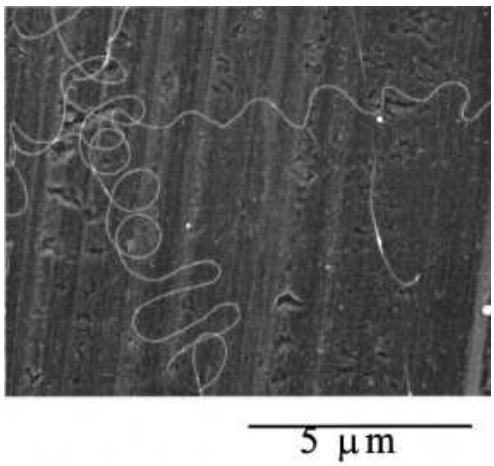

FIGURE 5.8. Scanning electron micrograph of coiled and looped nanofibers on the surface of an aluminum collector.

The well-known tendency [62] of a straight liquid jet moving in its axial direction to coil when it impacts a hard, stationary surface and buckles could account for some of the observed coils. This mechanical effect is easily

observed when a gravity driven jet of honey falls onto a hard surface. The occurrence of mechanical buckling during impact is likely to be infrequent because most of the long segments of the jet were moving in a sidewise direction as they encountered the collector. It is interesting to hypothesize that in these experiments the coils and loops solidified before collection. Then, the collected coils and loops provide information about the smallest bending instabilities that occurred.

5.3. Viscoelastic model of a rectilinear electrified liquid jet

Estimates based on the Maxwell equations, show that all possible magnetic effects can be safely neglected and the conditions of the electrohydrodynamics can be assumed.

Consider first a rectilinear electrified liquid jet in an electric field parallel to its axis. We model a segment of the jet by a viscoelastic dumbbell as shown in Fig. 5.9. In the mathematical description, we use the Gaussian electrostatic system of units. Corresponding SI units are given when parameters are evaluated. Table 5.1 lists the symbols and their units.

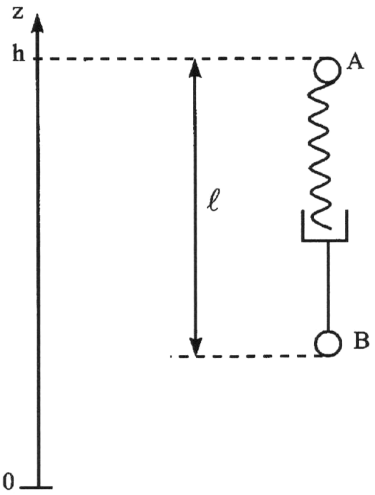

FIGURE 5.9. Viscoelastic dumbbell representing a segment of the rectilinear part of the jet.

Each of the beads, A and B, possesses a charge e and mass m. Let the position of bead A be fixed by non-Coulomb forces. The Coulomb repulsive

force acting on bead B is $-e^2/\ell^2$. The force applied to B due to the external field is $-eV_0/h$. The dumbbell, AB, models a viscoelastic Maxwellian liquid jet. Therefore the stress, σ, pulling B back to A is given by [68]

$$\frac{d\sigma}{dt} = G\frac{d\ell}{\ell dt} - \frac{G}{\mu}\sigma, \tag{5.1}$$

where t is time, G and μ are the elastic modulus and viscosity, respectively, and ℓ is the filament length. It should be emphasized that according to [62] and [69], the phenomenological Maxwell model adequately describes rheological behaviour of concentrated polymeric systems in strong uniaxial elongation, which is the case in the present work.

The momentum balance for bead B is

$$m\frac{dv}{dt} = -\frac{e^2}{\ell^2} - \frac{eV_0}{h} + \pi a^2\sigma, \tag{5.2}$$

where a is the cross-sectional radius of the filament, and v is the velocity of bead B which satisfies the kinematics equation

$$\frac{d\ell}{dt} = -v. \tag{5.3}$$

We adopt dimensionless descriptions, as is customary in fluid mechanics (see Table 5.2). We define the length scale $L_{e\ell} = (e^2/\pi a_0^2 G)^{1/2}$, where a_0 is the initial cross-sectional radius at $t = 0$, and render ℓ dimensionless by $L_{e\ell}$, and assume $L_{e\ell}$ to be also an initial filament length which is not restrictive. To make them dimensionless, we divide t by the relaxation time μ/G, stress σ by G, velocity v by $L_{e\ell}\,G/\mu$, and radius a by a_0. Denoting $W = -v$ and applying the condition that the volume of the jet is conserved,

$$\pi\, a^2\, \ell = \pi\, a_0^2\, L_{e\ell}, \tag{5.4}$$

we obtain Eqs. (5.1)-(5.3) in the following dimensionless forms:

$$\frac{d\bar{\ell}}{d\bar{t}} = \bar{W}, \tag{5.5a}$$

$$\frac{d\bar{W}}{d\bar{t}} = V - F_{ve}\frac{\bar{\sigma}}{\bar{\ell}} + \frac{Q}{\bar{\ell}^2}, \tag{5.5b}$$

$$\frac{d\bar{\sigma}}{d\bar{t}} = \frac{\bar{W}}{\bar{\ell}} - \bar{\sigma}, \tag{5.5c}$$

where the dimensionless parameters are denoted by bars, and the dimensionless groups are given by

$$Q = \frac{e^2 \mu^2}{L_{e\ell}^3 \, m \, G^2}, \tag{5.6a}$$

$$V = \frac{e \, V_0 \, \mu^2}{h \, L_{e\ell} \, m \, G^2}, \tag{5.6b}$$

$$F_{ve} = \frac{\pi \, a_0^2 \, \mu^2}{m \, L_{e\ell} \, G}. \tag{5.6c}$$

It is emphasized that in this momentum balance we temporarily neglect the secondary effects of the surface tension, gravity and the air drag force. Note also that using the definition of $L_{e\ell}$, we obtain from Eqs. (5.6a) and (5.6c) that $Q \equiv F_{ve}$. It should also be mentioned that here in Eq. (5.4) and hereinafter in this model, we neglect mass losses due to evaporation. In principle, they can be accounted for using a specific expression for the evaporation rate. Evaporation is not expected to introduce qualitative changes in jet dynamics in the main part of the jet path. However, the effect of solvent evaporation on the values of the rheological parameters of the polymer solution, which are not fully known at present, ultimately leads to the solidification of the jet into a polymer fiber. Evaporation and solidification are discussed in detail in Sec. 5.8.

Numerical solutions of the system, Eqs. (5.5), may be found using the following initial conditions at $\bar{t} = 0$:

$$\bar{\ell} = 1, \tag{5.7a}$$

$$\bar{W} = 0, \tag{5.7b}$$

$$\bar{\sigma} = 0. \tag{5.7c}$$

Rheological and electrical parameters of the polymer solution are at present not fully known from experiments. Therefore, here and hereinafter, the calculations were done with the best values available for the dimensionless groups. In certain cases, the values were chosen as close as possible to plausible estimates of the physical parameters involved. In these cases, we list the values of the physical parameters along with the values of the dimensionless groups based on them. The calculated results in Fig. 5.10 show that the longitudinal stress $\bar{\sigma}$ first increases over time as the filament stretches, passes

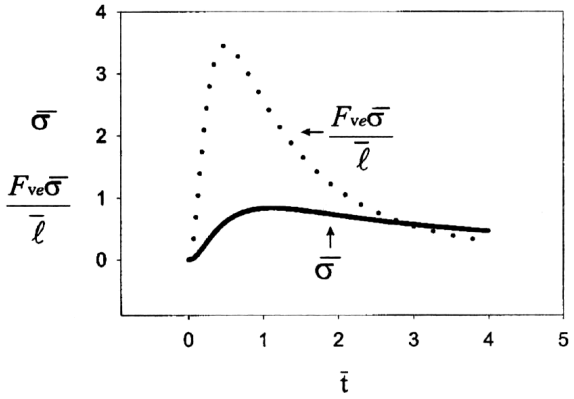

FIGURE 5.10. Longitudinal stress $\bar{\sigma}$ in the rectilinear part of the jet, and the longitudinal force $F_{ve}\bar{\sigma}/\bar{\ell}$. $Q = 12$, $V = 2$, $F_{ve} = 12$.

a maximum, and then begins to decrease, since the relaxation effects always reduce the stress at long times. The dimensionless longitudinal force in the filament, $F_{ve}\bar{\sigma}/\bar{\ell}$, passes its maximum before $\bar{\sigma}$ does. At the conditions corresponding to the maximum of $\bar{\sigma}$ the value of the force is already comparatively small and decreasing rapidly. We will see below that this small value of the longitudinal force allows the onset of an electrically driven bending instability. Therefore we identify the filament length, $\bar{\ell}^*$, at the condition when $\bar{\sigma}$ passes the maximum and the longitudinal force is already small, as the length of the rectilinear segment of the electrospun jet at which the bending insta-

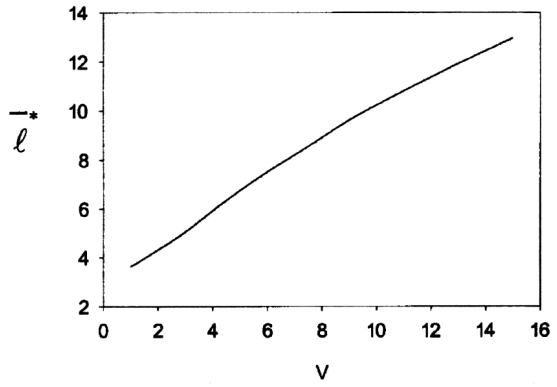

FIGURE 5.11. Length of the rectilinear part of the jet $\bar{\ell}^*$ as a function of the dimensionless voltage V. $Q = 12$ and $F_{ve} = 12$.

bility begins to grow rapidly. The relationship of this theoretically defined segment to the observed length of the straight segment is not yet determined. The length, $\bar{\ell}^*$, increases with applied voltage as is seen in Fig. 5.11. Near the pendant drop, the longitudinal force is also small, but the jet does not bend, since its radius there is large, and the corresponding bending stiffness is large.

The rectilinear liquid jets are unstable to capillary (varicose) perturbations driven by surface tension. Longitudinal stretching can stabilize the jet in the presence of these perturbations [70]. In electrospinning, jets are stretched along their axis by the external electric field and are elongated further by the repulsive force between charges on adjacent segments. The resulting tensile forces prevent development of capillary instability in the experiments reported here.

5.4. Bending instability of electrified jets

Dealing with the bending instability of electrospun jets, we consider the polymer solutions to be perfect dielectrics with frozen charges. This is justified by the fact that the bending instability we are going to tackle is characterized by the characteristic hydrodynamic time, $\tau_H \cong 1\,\mathrm{ms}$, and thus $\tau_C \gg \tau_H$ ($\tau_C = 35\,\mathrm{ms}$). Under such conditions the same fluid, which behaved as a perfect conductor in Taylor's cone, behaves as a perfect dielectric in the bending jet.

The reason for the observed bending instability may be understood in the following way. In the coordinates that move with a rectilinear electrified jet, the electrical charges can be regarded as a static system of charges interacting mainly by Coulomb's law (without the external field). Such systems are known to be unstable according to Earnshaw's theorem [71]. To illustrate the instability mechanism that is relevant in the electrospinning context, we consider three point-like charges each with a value e and originally in a straight line at A, B and C as shown in Fig. 5.12. Two Coulomb forces having magnitudes $F = e^2/r^2$ push against charge B from opposite directions. If a perturbation causes point B to move off the line by a distance δ to B$'$, a net force $F_1 = 2F\cos\theta = (2e^2/r^3)\,\delta$ acts on charge B in a direction perpendicular to the line, and tends to cause B to move further in the direction of the perturbation away from the line between fixed charges, A and C. The growth of the small bending perturbation that is characterized by δ is governed in

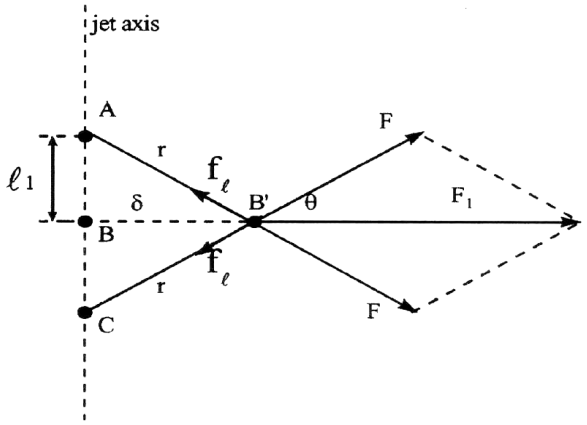

FIGURE 5.12. Illustration of the Earnshaw instability, leading to bending of an electrified jet.

the linear approximation by the equation

$$m\frac{d^2\delta}{dt^2} = \frac{2e^2}{\ell_1^2}\,\delta, \tag{5.8}$$

where m is the mass.

The growing solution of this equation, $\delta = \delta_0 \exp[(2e^2/m\,\ell_1^3)^{1/2}t]$, shows that small perturbations increase exponentially. The increase is sustained because electrostatic potential energy of the system depicted in Fig. 5.12 decreases as e^2/r when the perturbations, characterized by δ and r, grow. We believe that this mechanism is responsible for the observed bending instability of jets in electrospinning.

If charges, A, B, and C are attached to a liquid jet, forces associated with the liquid tend to counteract the instability caused by the Coulomb forces. For very thin liquid jets, the influence of the shearing force related to the bending stiffness can be neglected in comparison with the stabilizing effect of the longitudinal forces since the shearing forces are of the order of $O(a^4)$, which is much smaller than the longitudinal forces [62], which are of the order of $O(a^2)$. The longitudinal force, at the moment when the bending instability sets in, was calculated above for the stretching of a rectilinear filament. Its value is given by $f_\ell = \pi a^2 \sigma^*$ (or in the dimensionless form by $F_{ve}\,\bar{\sigma}^*/\bar{\ell}^*$). The values of σ and $\bar{\ell}$ at the moment when σ (or $\bar{\sigma}$) passes its maximum are denoted by asterisks. The forces f_ℓ are directed along BC or BA in Fig. 5.12, and are opposite to the local Coulomb force F. If F is larger

than the viscoelastic resistance, f_ℓ, the bending perturbation continues to grow, but at a rate decelerated by f_ℓ.

It might be thought that bending perturbations of very short lengths can always overcome the viscoelastic resistance f_ℓ, since the Coulomb force increases when the wavelength of the perturbation decreases. In fact, the surface tension always counteracts the bending instability because bending always leads to an increase of the area of the jet surface [62]. Surface tension resists the development of too large a curvature by the perturbation ABC in Fig. 5.12, and therefore limits the smallest possible perturbation wavelengths. All these factors are accounted for in the description of the three-dimensional bending instability of electrospun jets in Secs. 5.6 and 5.7.

5.5. Localized approximation

In the dynamics of thin vortices in fluids the localized-induction approximation is widely used to describe velocity induced at a given vortex element by the rest of the vortex line [72−76]. A similar approach may be used to calculate the electric force imposed on a given element of an electrified jet by the rest of it. Consider an enlarged element of a curved jet shown in Fig. 5.13. We assume that the arc length ξ is reckoned along the jet axis from the cen-

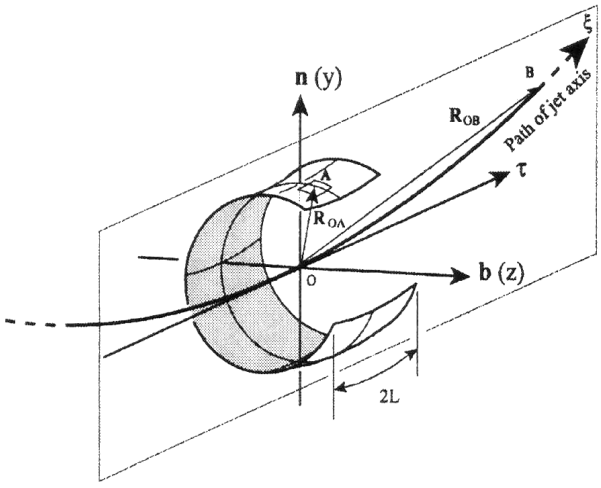

FIGURE 5.13. Sketch of an enlarged element of a curved jet and the associated normal, binormal and tangent vectors $\mathbf{n}$, $\mathbf{b}$, and $\boldsymbol{\tau}$.

tral cross-section of the element where $\xi = 0$. We denote the coordinates reckoned along the normal and binormal by y and z, so that the radius vector of point A on the surface of the element $\mathbf{R}_{\rm OA} = y\,\mathbf{n} + z\,\mathbf{b}$. The radius vector of point B at the jet axis close enough to the element considered is thus given by

$$\mathbf{R}_{\rm OB} = \boldsymbol{\tau}\,\xi + \frac{1}{2}|k_0|\,\xi^2\mathbf{n}, \tag{5.9}$$

where k_0 is the curvature of the jet axis at point O and $\boldsymbol{\tau}$ is a unit tangent vector. Therefore

$$\mathbf{R}_{\rm BA} = \mathbf{R}_{\rm OA} - \mathbf{R}_{\rm OB} = \left[y - \frac{1}{2}|k_0|\,\xi^2\right]\mathbf{n} + z\,\mathbf{b} - \boldsymbol{\tau}\,\xi. \tag{5.10}$$

Denote the cross-sectional radius of the jet element by a, assume that charge is uniformly distributed over the jet surface with the surface density Δe, and denote the charge per unit jet length by $e = 2\pi\,a\,\Delta e$. Then the Coulomb force acting at a surface element near point A from the jet element situated near point B is given by

$$d\mathbf{F}_{BA} = \frac{e\,d\xi\,\Delta e\,a\,d\theta\,d\xi}{\left|\mathbf{R}_{\rm BA}\right|^3}\,\mathbf{R}_{\rm BA}, \tag{5.11}$$

where θ is the polar angle in the jet cross-section. Substituting Eq. (5.10) in Eq. (5.11) and accounting for the fact that $y = a\cos\theta$ and $z = a\,\sin\theta$, we obtain from Eq. (5.11)

$$d\mathbf{F}_{BA} = e\,d\xi\,\Delta e\,a\,d\theta\,d\xi\frac{\left[(a\cos\theta - |k_0|\,\xi^2/2)\,\mathbf{n} + a\sin\theta\,\mathbf{b} - \boldsymbol{\tau}\,\xi\right]}{\left[a^2 - a\cos\theta\,|k_0|\,\xi^2 + |k_0|^2\,\xi^4/4 + \xi^2\right]^{3/2}}. \tag{5.12}$$

For a thin jet, as $a \to 0$, all the terms containing a in the numerator of Eq. (5.12) can be safely neglected, also in the denominator the term $a\cos\theta\,|k_0|\,\xi^2$ is negligibly small as compared to ξ^2. Then using Eq. (5.12) we calculate the electric force acting on a particular element of the jet, assuming that the length of the element is $2L$, with L being a cut-off for the integral, to be determined later on

$$\mathbf{F}_{e\ell} = \int\limits_0^{2\pi} d\theta \int\limits_{-L}^{L} d\mathbf{F}_{BA} = e^2\,d\xi \int\limits_{-L}^{L} d\xi\frac{-\boldsymbol{\tau}\,\xi - |k_0|\,\xi^2\,\mathbf{n}/2}{\left[a^2 + \xi^2 + |k_0|^2\,\xi^4/4\right]^{3/2}}\,. \tag{5.13}$$

The latter yields

$$\mathbf{F}_{e\ell} = e^2\,d\xi \int\limits_{-L/a}^{L/a} dx\left[\frac{-\boldsymbol{\tau}\,x}{a(1+x^2)^{3/2}} - \frac{|k_0|\,x^2\,\mathbf{n}/2}{(1+x^2)^{3/2}}\right]. \tag{5.14}$$

The force in the axial direction obviously cancels, whereas the force becomes

$$\mathbf{F}_{e\ell} = -e^2\,\ell\,n\left(\frac{L}{a}\right)\,|k|\,\mathbf{n}\,d\xi. \tag{5.15}$$

This shows that the net electric force acting on a jet element is related to its curvature $\mathrm{k} = k_0$, and acts in the normal (lateral) direction to the jet axis. The magnitude of the net force acting on a jet element due to the action of the surface tension forces is equal to

$$\mathbf{F} = \pi\,a\,\sigma\,\boldsymbol{\tau}\Big|_{\xi+d\xi} - \pi\,a\,\sigma\,\boldsymbol{\tau}\Big|_{\xi} = \pi\,a\,\sigma\,|k|\,\mathbf{n}\,d\xi, \tag{5.16}$$

where σ is the surface tension coefficient.

Therefore, the net normal (lateral) force acting on a jet element is given by the sum of the electric and surface tension forces, Eqs. (5.15) and (5.16), as

$$d\mathbf{F} = |k|\,\mathbf{n}\,d\xi\left[\pi\,a\,\sigma - e^2\,\ell\,n\,\frac{L}{a}\right]. \tag{5.17}$$

The cut-off length L is still to be found. It will be done below in Sec. 5.9.

5.6. Continuous quasi-one-dimensional equations of the dynamics of electrified liquid jets

For very thin jets we can neglect, in the first approximation, the effect of the shearing force in the jet cross-section, as well as the bending stiffness (cf. [62], p. 49). If we use a Lagrangian parameter s "frozen" into the jet elements, then the momentless quasi-one-dimensional equations of the jet dynamics (cf. [62], Eq. (4.19) p. 49) take the form

$$\lambda\,f = \lambda_0\,f_0, \tag{5.18a}$$

$$\rho\,\lambda_0\,f_0\frac{\partial\mathbf{V}}{\partial t} = \boldsymbol{\tau}\frac{\partial P}{\partial s} + \lambda\,|k|\,P\,\mathbf{n} - \rho\,g\,\lambda_0\,f_0\,\mathbf{k} + \lambda\,|k|\left(\pi\,a\,\sigma - e^2\ell\,n\frac{L}{a}\right)\mathbf{n} - \lambda\,e\frac{U_0}{h}\,\mathbf{k}. \tag{5.18b}$$

Equation (5.18a) is the continuity equation with λ being the geometrical stretching ratio, so that $\lambda\,ds = d\xi$ and $f = \pi a^2$ the cross-sectional area. Subscript zero denotes the parameter values at time $t = 0$. Equation (5.18b) is the momentum balance equation with ρ being the liquid density, $\mathbf{V}$ is its

velocity, P is the longitudinal force in the jet cross-section (of viscoelastic origin in the case of electrospinning of polymer jets), $g\,\mathbf{k}$ is gravity acceleration, and U_0/h is the outer field strength (the outer field is assumed to be parallel to the unit vector $\mathbf{k}$, with U_0 being the value of electrical potential at the jet origin, and h the distance between the origin and a ground plate). It is emphasized that on the right-hand side of the momentum Eq. (5.18b) we account for the longitudinal internal force of rheological origin acting on the jet (the first two terms), the gravity force (the third term), the bending electrical force and the stabilizing effect of the surface tension (the fourth term following from Eq. (5.17)), and for the electric force acting on the jet from an electric field created by the potential difference of the starting point of the jet and the collector.

Equations (5.18) are supplemented by the kinematic relation

$$\frac{\partial \mathbf{R}}{\partial t} = \mathbf{V}, \tag{5.19}$$

where $\mathbf{R}$ is the radius vector of a point on the axis of the jet.

Introducing the Cartesian coordinate system associated with a capillary (the jet origin) or a ground plate, with unit vectors $\mathbf{i}$, $\mathbf{j}$, and $\mathbf{k}$, and accounting for

$$\begin{aligned} \mathbf{R} &= \mathbf{i}\,X + \mathbf{j}\,Y + \mathbf{k}\,Z, \\ \mathbf{V} &= \mathbf{i}\,u + \mathbf{j}\,v + \mathbf{k}\,w, \end{aligned} \tag{5.20}$$

we obtain from the projections of Eqs. (5.18b) and (5.19) the following system of scalar equations

$$\rho\,\lambda_0\,f_0\frac{\partial u}{\partial t} = \tau_X\frac{\partial P}{\partial s} + \lambda\,|k|\,P\,n_X + \lambda\,|k|\left(\pi a\sigma - e^2\ell n\frac{L}{a}\right)n_X, \tag{5.21a}$$

$$\rho\,\lambda_0\,f_0\frac{\partial v}{\partial t} = \tau_Y\frac{\partial P}{\partial s} + \lambda\,|k|\,P\,n_Y + \lambda\,|k|\left(\pi a\sigma - e^2\ell n\frac{L}{a}\right)n_Y, \tag{5.21b}$$

$$\begin{aligned} \rho\,\lambda_0\,f_0\frac{\partial w}{\partial t} &= \tau_Z\frac{\partial P}{\partial s} + \lambda\,|k|\,P\,n_Z \\ &\quad + \lambda\,|k|\left(\pi\,a\,\sigma - e^2\ell\,n\frac{L}{a}\right)n_Z - \rho\,g\,\lambda_0\,f_0 - \lambda\,e\,\frac{U_0}{h}, \end{aligned} \tag{5.21c}$$

$$\frac{\partial X}{\partial t} = u, \qquad \frac{\partial Y}{\partial t} = v, \qquad \frac{\partial Z}{\partial t} = w. \tag{5.22}$$

The following geometric relations should be added:

$$\lambda = \left(X_{,s}^2 + Y_{,s}^2 + Z_{,s}^2\right)^{\frac{1}{2}}, \tag{5.23}$$

$$\tau_X = \frac{1}{\lambda}\frac{\partial X}{\partial s}, \qquad \tau_Y = \frac{1}{\lambda}\frac{\partial Y}{\partial s}, \qquad \tau_Z = \frac{1}{\lambda}\frac{\partial Z}{\partial s},$$
$$n_X = \frac{1}{|k|\,\lambda}\frac{\partial \tau_X}{\partial s}, \qquad n_Y = \frac{1}{|k|\,\lambda}\frac{\partial \tau_Y}{\partial s}, \qquad n_Z = \frac{1}{|k|\,\lambda}\frac{\partial \tau_Z}{\partial s}, \tag{5.23 [cont.]}$$

$$|k| = \left[\frac{\left(X_{,s}^2 + Y_{,s}^2 + Z_{,s}^2\right)\left(X_{,ss}^2 + Y_{,ss}^2 + Z_{,ss}^2\right) - \left(X_{,s}X_{,ss} + Y_{,s}Y_{,ss} + Z_{,s}Z_{ss}\right)^2}{\left(X_{,s}^2 + Y_{,s}^2 + Z_{,s}^2\right)^3}\right]^{\frac{1}{2}}.$$

Also assuming the simplest version of the upper-convected Maxwell model of viscoelasticity properly fitted to describe uniaxial elongation [62, 77], we obtain the equation for the normal stress in the jet cross-section $\sigma_{\tau\tau}$

$$\frac{\partial \sigma_{\tau\tau}}{\partial t} = G\frac{1}{\lambda}\frac{\partial \lambda}{\partial t} - \frac{G}{\mu}\sigma_{\tau\tau}\,, \tag{5.24}$$

where G is the modulus of elasticity, and μ is the viscosity, and

$$\frac{1}{\lambda}\frac{\partial \lambda}{\partial t} = \frac{X_{,s}\,u_{,s} + Y_{,s}\,v_{,s} + Z_{,s}\,w_{,s}}{\lambda^2}\,. \tag{5.25}$$

Then the longitudinal force P is given by

$$P = \frac{\lambda_0\, f_0}{\lambda}\sigma_{\tau\tau}\,. \tag{5.26}$$

It is emphasized that in Eq. (5.26) should actually stand the normal stress $\sigma_{\tau\tau} - \sigma_{nn}$ instead of $\sigma_{\tau\tau}$. However, in strong uniaxial elongational flows (electrospinning is an example of such a flow) the axial component $\sigma_{\tau\tau} \gg \sigma_{nn}$, and the latter can be neglected. Detailed proof of this fact can be found in [63].

Also the equation of the charge conservation in a jet element holds

$$e\,\lambda = e_0\,\lambda_0. \tag{5.27}$$

The system of the equations presented in this section allows one to find the jet configuration in space at any moment of time. The equations will be discretized and solved numerically. It is emphasized that the discretized equations can also be obtained directly considering the jet to be a locus of inertial electrically charged beads connected by the spring and dashpot viscoelastic elements (similar to Sec. 5.4). This is done in the following section.

5.7. Discretized three-dimensional equations of the dynamics of the electrospun jets

In the present section we account for the whole integral responsible for the electric force. This is the only difference with Sec. 5.6 where the bending electric force is calculated using the localized approximation.

We represent the electrospun jets by a model system of beads possessing charge e and mass m connected by viscoelastic elements as shown in Fig. 5.14, which generalizes the models of Figs. 5.9 and 5.12. It needs to be mentioned that these imaginary beads are not the same as the physical beads [24] resulting from the varicose instability. The parameters corresponding to the element connecting bead i with bead $(i+1)$ are denoted by subscript u (up), those for the element connecting bead i with $(i-1)$ by subscript d (down). The lengths ℓ_{ui} and ℓ_{di} of these elements are given by

$$\begin{aligned} \ell_{ui} &= \left[(x_{i+1}-x_i)^2+(y_{i+1}-y_i)^2+(z_{i+1}-z_i)^2\right]^{\frac{1}{2}}, \\ \ell_{di} &= \left[(x_i-x_{i-1})^2+(y_i-y_{i-1})^2+(z_i-z_{i-1})^2\right]^{\frac{1}{2}}, \end{aligned} \tag{5.28}$$

respectively, where x_i, y_i, $z_i, \ldots$, are the Cartesian coordinates of the beads.

The rates of strain of the elements are given by $(d\ell_{ui}/dt)/\ell_{ui}$ and $(d\ell_{di}/dt)/\ell_{di}$. The viscoelastic forces acting along the elements are similar to Eq. (5.1),

$$\begin{aligned} \frac{d\sigma_{ui}}{dt} &= G\frac{1}{\ell_{ui}}\frac{d\ell_{ui}}{dt}-\frac{G}{\mu}\sigma_{ui}, \\ \frac{d\sigma_{di}}{dt} &= G\frac{1}{\ell_{di}}\frac{d\ell_{di}}{dt}-\frac{G}{\mu}\sigma_{di}. \end{aligned} \tag{5.29}$$

The total number of beads, N, increases over time as new electrically charged beads are inserted at the top of Fig. 5.14 to represent the flow of solution into the jet. The net Coulomb force acting on the i-th bead from all the other beads is given by

$$\mathbf{f}_C = \sum_{\substack{j=1,N \\ j\neq i}} \frac{e^2}{R_{ij}^2}\left[\mathbf{i}\,\frac{x_i-x_j}{R_{ij}}+\mathbf{j}\,\frac{y_i-y_j}{R_{ij}}+\mathbf{k}\,\frac{z_i-z_j}{R_{ij}}\right], \tag{5.30}$$

where $\mathbf{i}$, $\mathbf{j}$ and $\mathbf{k}$ are unit vectors along the x, y and z axes, respectively, and

$$R_{ij} = \left[(x_i-x_j)^2+(y_i-y_j)^2+(z_i-z_j)^2\right]^{\frac{1}{2}}. \tag{5.31}$$

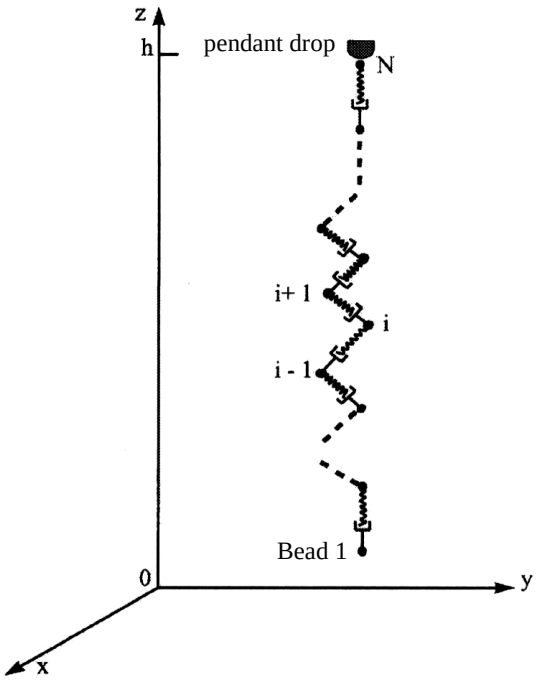

FIGURE 5.14. Bending electrospun jet modeled by a system of beads connected by viscoelastic elements.

The electric force imposed on the i-th bead by the electric field created by the potential difference between the pendant drop and the collector is

$$\mathbf{f}_0 = -e\frac{V_0}{h}\,\mathbf{k}. \tag{5.32}$$

It is clear that the gravitational force may be included in $\mathbf{f}_0$.

The net viscoelastic force acting on the i-th bead of the jet is

$$\mathbf{f}_{ve} = \pi a_{ui}^2\,\sigma_{ui}\left[\mathbf{i}\,\frac{x_{i+1}-x_i}{\ell_{ui}} + \mathbf{j}\,\frac{y_{i+1}-y_i}{\ell_{ui}} + \mathbf{k}\,\frac{z_{i+1}-z_i}{\ell_{ui}}\right]$$
$$- \pi a_{di}^2\,\sigma_{di}\left[\mathbf{i}\,\frac{x_i-x_{i-1}}{\ell_{di}} + \mathbf{j}\,\frac{y_i-y_{i-1}}{\ell_{di}} + \mathbf{k}\,\frac{z_i-z_{i-1}}{\ell_{di}}\right], \tag{5.33}$$

where, when mass is conserved and evaporation neglected, the filament radii

a_{ui} and a_{di} are given by

$$\begin{aligned} \pi\, a_{ui}^2\, \ell_{ui} &= \pi\, a_0^2\, L_{e\ell}, \\ \pi\, a_{di}^2\, \ell_{di} &= \pi\, a_0^2\, L_{e\ell}, \end{aligned} \tag{5.34}$$

which is similar to Eq. (5.4).

The surface tension force acting on the i-th bead, and tending to restore the rectilinear shape of the bending part of the jet, is given by

$$\mathbf{f}_{cap} = -\frac{\sigma\, \pi (a^2)_{av}\, k_i}{(x_i^2 + y_i^2)^{\frac{1}{2}}} \Big[\mathbf{i}\, |x_i|\, \mathrm{sign}(x_i) + \mathbf{j}\, |y_i|\, \mathrm{sign}(y_i) \Big], \tag{5.35}$$

where σ is the surface tension coefficient, k_i is the jet curvature calculated using the coordinates of beads $(i-1)$, i and $(i+1)$, and $(a^2)_{av} = (a_{ui}+a_{di})^2/4$. The meaning of "sign" is as follows:

$$\mathrm{sign}(x) = \begin{cases} 1, & \text{if} \quad x > 0, \\ 0, & \text{if} \quad x = 0, \\ -1, & \text{if} \quad x < 0. \end{cases} \tag{5.36}$$

Setting the forces described in Eqs. (5.30), (5.32), (5.33), and (5.35) equal to mass times acceleration, according to Newton's second law, we obtain the equation governing the radius vector of the position of the i-th bead $\mathbf{r}_i = \mathbf{i}\, x_i + \mathbf{j}\, y_i + \mathbf{k}\, z_i$ in the following form:

$$\begin{aligned} m \frac{d^2 \mathbf{r}_i}{dt^2} = & \sum_{\substack{j\,=\,1,\,N \\ j\,\neq\,i}} \frac{e^2}{R_{ij}^3} (\mathbf{r}_i - \mathbf{r}_j) - e \frac{V_0}{h}\, \mathbf{k} + \frac{\pi\, a_{ui}^2\, \sigma_{ui}}{\ell_{ui}} (\mathbf{r}_{i+1} - \mathbf{r}_i) \\ & - \frac{\pi\, a_{di}^2\, \sigma_{di}}{\ell_{di}} (\mathbf{r}_i - \mathbf{r}_{i-1}) - \frac{\sigma\, \pi (a^2)_{av}\, k_i}{\left(x_i^2 + y_i^2\right)^{\frac{1}{2}}} \big[\mathbf{i}\, |x_i|\, \mathrm{sign}(x_i) + \mathbf{j}\, |y_i|\, \mathrm{sign}(y_i) \big]. \end{aligned} \tag{5.37}$$

For the first bead, $i = 1$, the total number of beads, N, is also 1. As more beads are added, N becomes larger and the first bead $i = 1$ remains at the bottom end of the growing jet. For this bead, all the parameters with subscript d should be set equal to zero since there are no beads below $i = 1$. Equation (5.37) is essentially a discretized form of Eq. (5.18b) or of its scalar counterparts, Eqs. (5.21), (5.22).

It is easy to show that the aerodynamic drag force and gravity have a negligibly small effect on the electrospinning. Indeed, for an uncharged jet

moving in air at high speed, an aerodynamically driven bending instability may set in if $\rho_a V_0^2 > \sigma/a$, where ρ_a is the air density, V_0 is the jet velocity, and σ is the surface tension coefficient [62, 78]. Taking, for example, $\rho_a = 1.21\,\mathrm{kg/m^3}$, $V_0 \sim 0.5\,\mathrm{m/s}$, $\sigma \sim 0.1\,\mathrm{kg/s^2}$, and $a \sim 10^{-4}\,\mathrm{m}$, we estimate $\rho_a V_0^2 \sim 0.3\,\mathrm{kg/m{\cdot}}s^2$, which is much smaller than $\sigma/a \sim 10^3\,\mathrm{kg/m{\cdot}}s^2$. Therefore, under the conditions characteristic of the experiments on electrospinning, the aerodynamically driven bending instability does not occur.

The air drag force per unit jet length, which tends to compress the jet along its axis, is given by [79]

$$f_a = \pi\, a\, \rho_a V_0^2\, 0.65 \left(\frac{2V_0 a}{\nu_a}\right)^{-0.81}, \tag{5.38}$$

where ρ_a and ν_a are the air density and kinematic viscosity, respectively. The gravity force per unit length pulling the jet downward in the experimental geometry shown in Fig. 5.1 is

$$f_g = \rho\, g\, \pi\, a^2, \tag{5.39}$$

where ρ is the liquid density, and g is the acceleration due to gravity.

In the momentum balance, Eqs. (5.2) or (5.5b), we neglected f_g as a secondary effect. The air drag force f_a is even smaller than f_g. Taking $\rho_a = 1.21\,\mathrm{kg/m^3}$, $\nu_a = 0.15 \cdot 10^{-4}\,\mathrm{m^2/s}$, $\rho = 1000\,\mathrm{kg/m^2}$, $V_0 = 0.5\mathrm{m/s}$ and $a = 150\,\mu\mathrm{m}$ we obtain from Eqs. (5.38) and (5.39) $f_a = 1.4 \cdot 10^{-5}\,\mathrm{kg/s^2}$ and $f_g = 6.9 \cdot 10^{-4}\,\mathrm{kg/s^2}$. The compressive stress along the jet axis of the air drag is negligibly small in comparison with the stretching due to gravity, and is much smaller than the stretching due to the electrical forces. Buckling of the electrospun jet due to the compressive force from air drag does not occur, since the electrical forces that tend to elongate the jet are larger and dominate any perturbation that might lead to buckling.

5.8. Evaporation and solidification

The systems of governing equations in Secs. 5.6 and 5.7 do not account for the evaporation and solidification effects. We account for them in the present section.

In [80] the following correlation is given for the Nusselt number for a cylinder moving parallel to its axis in air

$$Nu = 0.42\, Re^{\frac{1}{3}}, \tag{5.40}$$

where the Reynolds number $Re = V_0\, 2a/\nu_a$, a is the cross-sectional radius, and ν_a is the kinematic viscosity of air.

Taking the Prandtl number of air to be $Pr = 0.72$, we can generalize the correlation (5.40) for an arbitrary value of the Prandtl number as

$$Nu = 0.495\, Re^{\frac{1}{3}} Pr^{\frac{1}{2}}. \tag{5.41}$$

Similarly, to (5.41), we take the following correlation for the Sherwood number

$$Sh = 0.495\, Re^{\frac{1}{3}} Sc^{\frac{1}{2}}, \tag{5.42}$$

where $Sh = h_m\, 2a/D_a$, where h_m is the mass transfer coefficient for evaporation, D_a is the vapour diffusion coefficient in air, and the Schmidt number $Sc = \nu_a/D_a$. The Sherwood number is the dimensionless mass transfer coefficient describing the evaporation rate.

Correlations of the type of Eqs. (5.40)–(5.42) are valid for the air ($Pr = 0.72$) for the Reynolds number in the range $1 \leqslant Re \leqslant 60$. For $a \leqslant 10^{-2}\,\mathrm{cm}$, $V_0 \sim 10^2 \div 10^3\,\mathrm{cm/s}$ and $\nu_a = 0.15\,\mathrm{cm}^2/\mathrm{s}$, the Reynolds number is $10 \leqslant Re \leqslant 10^2$ which corresponds approximately to the range of validity.

The initial mass of polymer in a jet element is given by

$$M_{p0} = \rho\, f_0\, \lambda_0\, ds\, c_{p0}, \tag{5.43}$$

where c_{p0} is the initial polymer mass fraction. The variable solvent content in the element is

$$M_s = \rho\, f\, \lambda\, ds - \rho\, f_0\, \lambda_0\, ds\, c_{p0}, \tag{5.44}$$

which corresponds to the solvent mass fraction

$$c_s = 1 - \frac{f_0 \lambda_0}{f \lambda} c_{p0}. \tag{5.45}$$

The solvent mass decreases due to evaporation according to the equation

$$\frac{\partial M_s}{\partial t} = -\rho\, h_m \big[c_{s,eq}(T) - c_{s\infty}\big] 2\pi\, a\, \lambda\, ds, \tag{5.46}$$

where $c_{s,eq}(T)$ is the saturation vapour concentration of solvent at temperature T, and $c_{s\infty}$ is the vapour concentration in atmosphere far from the jet.

For water as a solvent, the following expression for $c_{s,eq}(\mathrm{T})$ is recommended [81]:

$$c_{s,eq} = \frac{1}{1013}\Big\{a_0 + T\Big[a_1 + T\Big(a_2 + T\big(a_3 + T\big(a_4 + T(a_5 + a_6 T)\big)\big)\Big)\Big]\Big\}, \tag{5.47}$$

where T is taken in the Celsius degrees, and

$$a_0 = 6.107799961, \qquad a_1 = 4.436518521 \cdot 10^{-1},$$
$$a_2 = 1.428945805 \cdot 10^{-2}, \qquad a_3 = 2.650648731 \cdot 10^{-4},$$
$$a_4 = 3.031240396 \cdot 10^{-6}, \qquad a_5 = 2.034080948 \cdot 10^{-8},$$
$$a_6 = 6.136820929 \cdot 10^{-11}.$$

The concentration $c_{s\infty}$ is equal to a relative humidity in atmosphere.

Substituting Eqs. (5.42) and (5.44) in Eq. (5.46), we obtain the equation describing the variation of the jet volume

$$\frac{\partial f\lambda}{\partial t} = -D_a\, 0.495\, Re^{\frac{1}{3}} Sc^{\frac{1}{2}} \left[c_{s,eq}(T) - c_{s\infty}\right] \pi\lambda\,. \tag{5.48}$$

Solvent mass decreases until the solvent mass ratio defined by Eq. (5.46) becomes small enough (say, $c_s = 0.1$), at which point the evaporation part of the calculation is stopped and the viscosity remains a constant value. This cut-off can be rationalized by the assumption that further evaporation is reduced because the diffusion coefficient of solvent in the remaining polymer is small.

When the evaporation is accounted for as per Eq. (5.48), the left-hand sides of Eqs. (5.18b), and (5.21) become, respectively,

$$\rho\frac{\partial f\lambda\,\mathbf{V}}{\partial t}, \tag{5.49}$$

$$\rho\frac{\partial f\lambda\,u}{\partial t}, \tag{5.50a}$$

$$\rho\frac{\partial f\lambda\,v}{\partial t}, \tag{5.50b}$$

$$\rho\frac{\partial f\lambda\,w}{\partial t}. \tag{5.50c}$$

Also the gravity term in Eq. (5.21c) should contain $f\lambda$ instead of $f_0\lambda_0$, since due to the evaporation $f\lambda$ is not equal to $f_0\lambda_0$ any more.

If the discretized version of the model described in Sec. 5.7 is used, λ in Eq. (5.48) is replaced by the distance between two adjoining beads.

The local polymer mass ratio in the jet is given by

$$c_p = c_{p0}\frac{f_0\lambda_0}{f\lambda}. \tag{5.51}$$

We account for the solidification process due to solvent evaporation employing the following correlation for the viscosity dependence on the polymer concentration [80]

$$\mu = 10^A \cdot 10^{B\, c_p^m} \tag{5.52}$$

with $m = 0.1$ to 1.

The value of parameter B is estimated as follows. According to [80] (p. 32), when c_p is doubled, the viscosity of the solution increases by a factor of 10 to 10^2. Using the value 10^2 and assuming that c_p increased from 0.1 to 0.2, we find for $m = 1$ that $B = 20$. The value of $B = 17.54$ corresponds to the factor of 10 and $m = 0.1$. Therefore the order of magnitude estimate of B yields the value $B = O(10)$. The value of A is unimportant, since the initial value of the viscosity $\mu_0 = 10^A \cdot 10^{B\, c_{p0}^m}$ is assumed to be known and is used for scaling. On the other hand, the relaxation time θ is proportional to c_p [62]. Therefore

$$\frac{\theta}{\theta_0} = \frac{c_p}{c_{p0}}, \tag{5.53}$$

where the initial relaxation time in known.

The modulus of elasticity $G = \mu/\theta$. Rendering the equations of the problem dimensionless, we obtain the rheological constitutive equation (5.24) in the following dimensionless form:

$$\frac{\partial \bar{\sigma}_{\tau\tau}}{\partial \bar{t}} = \bar{G}\frac{\partial \lambda}{\lambda \partial \bar{t}} - \frac{\bar{G}}{\bar{\mu}}\bar{\sigma}_{\tau\tau}. \tag{5.54}$$

Here G is rendered dimensionless by $G_0 = \mu_0/\theta_0$ and μ by μ_0. Therefore

$$\bar{G} = \frac{10^{B(c_p^m - c_{p0}^m)}}{c_p/c_{p0}}, \tag{5.55}$$

$$\bar{\mu} = 10^{B(c_p^m - c_{p0}^m)}, \tag{5.56}$$

with $B = O(10)$.

5.9. Growth rate and wavelength of small bending perturbations of an electrified liquid column

In [62] and [78] the theory of the aerodynamically driven jet bending was described. In that case, due to the jet curvature, a distributed lift force acts on the jet (because of the Bernoulli equation for airflow), which enhances

perturbations and makes the perturbations grow. The aerodynamic bending force per jet length $d\xi$ in the case of small bending perturbations is given by [62, 78]

$$\mathbf{F}_{aer} = -\rho_a V_0 \pi a_0^2 |k| \mathbf{n} d\xi, \tag{5.57}$$

where ρ_a is the air density, V_0 is the jet velocity, and a_0 the jet cross-sectional radius which does not change for small perturbations.

This force is the only difference between the aerodynamic- and electric-driven bending. Comparing Eq. (5.15) (with $e = e_0$) with Eq. (5.57), we see that all the results obtained in [62] and [78] for the aerodynamic bending may also be used here in the case of electric bending, if one replaces the factor $\rho_a V_0^2$ by $e_0^2 \ell n(L/a_0)/\pi a_0^2$.

Dynamics of small bending perturbations was studied in [62] and [78] accounting for the shearing force and moment in jet cross-section (thus, accounting for the bending stiffness in the equations generalizing Eqs. (5.21), (5.22)). For example, the case of viscous Newtonian fluid was considered. We recast these results here for the case of an electrified liquid column of Newtonian fluid of viscosity μ. In particular, this generalizes the results of Taylor [82] to the viscous case, and allows us to find the cut-off length L.

Recasting the results of [62] and [78], we find that the destabilizing electric force overcomes the stabilizing effect of the surface tension if

$$e_0^2 \ell n \left(\frac{L}{a_0} \right) > \pi a_0 \sigma. \tag{5.58}$$

If we assume $a_0 = 0.015\,\text{cm}$, and the jet charge of 1 Coulomb/liter, then $e_0 = 2120.5\,(\text{g·cm})^{1/2}/\text{s}$. Below we show that a reasonable value of L is $L = 0.0325\,\text{cm}$. Using it for the estimate, we find that $e_0^2 \ell n(L/a_0) = 3.465 \cdot 10^6\,\text{g·cm/s}^2$, whereas $\pi a_0 \sigma = 3.3\,\text{g·cm/s}^2$ for $\sigma = 70\,\text{g/s}^2$. Therefore, in this case the inequality (5.58) definitely holds and the bending instability should set in and grow.

From the results of [62] and [78] we obtain in the present case that the wavenumber χ_* and the growth rate γ_* of the fastest growing bending perturbation are given by

$$\chi_* = \left\{ \frac{8}{9} \frac{\rho a_0^2}{\mu^2} \left[\frac{e_0^2 \ell n(L/a_0)}{\pi a_0^2} - \frac{\sigma}{a_0} \right] \right\}^{\frac{1}{6}}, \tag{5.59a}$$

$$\gamma_* = \frac{\left[e_0^2 \ell n(L/a_0)/\pi a_0^2 - \sigma \right]^{\frac{2}{3}}}{(3\mu\rho a_0^4)^{\frac{1}{3}}}. \tag{5.59b}$$

Here $\chi_* = 2\pi a_0/\ell_*$, where ℓ_* is the wavelength of the fastest growing perturbation.

The results (5.59) correspond to the maximum of the spectrum $\gamma(\chi)$ given by the characteristic equation

$$\gamma^2 + \frac{3}{4}\frac{\mu\chi^4}{\rho a_0^2}\gamma + \left[\frac{\sigma}{\rho a_0^3} - \frac{e_0^2\,\ell n(L/a_0)}{\pi\rho a_0^4}\right]\chi^2 = 0. \tag{5.60}$$

This equation is to be compared with the characteristic equation for electrically driven bending perturbations of an inviscid liquid ($\mu = 0$) column derived by Taylor [82] (his Eq. (12)). Expanding that equation in the long-wave limit as $\chi \to 0$, we find that it reduces to Eq. (5.60) with the term $\ell n(1/\chi_*)$ instead of $\ell n(L/a_0)$. This fact defines the cut-off length L, since the result of Taylor [82] is exact. Thus taking $\ell\, n(L/a_0) = \ell\, n(1/\chi_*)$ and neglecting the minor surface tension effect in Eq. (5.59a), we reduce the latter to the form

$$\chi_* = \left[\frac{8}{9}\frac{\rho}{\mu^2}\frac{e_0^2}{\pi}\,\ell\, n\left(\frac{1}{\chi_*}\right)\right]^{\frac{1}{6}}, \tag{5.61}$$

which is the equation defining χ_* (and thus L). Taking the same values of the parameters as before, as well as $\rho = 1\,\mathrm{g/cm^3}$ and $\mu = 10^4\,\mathrm{g/(cm{\cdot}s)}$ (remember that $e_0 = 2120.5\,(\mathrm{g{\cdot}cm})^{1/2}/\mathrm{s}$), we reduce Eq. (5.61) to the form

$$\chi_* = 0.483\left[\ell\, n\left(\frac{1}{\chi_*}\right)\right]^{\frac{1}{6}}, \tag{5.62}$$

which yields $\chi_* = 0.462$.

Therefore the wavelength of the fastest growing perturbation $\ell_* = 2\pi \cdot 0.015/0.462 = 0.204\,\mathrm{cm}$ and the cut-off length $L = \ell_*/2\pi = 0.0325\,\mathrm{cm}$. Comparing the latter with the jet cross-sectional radius $a_0 = 0.015\,\mathrm{cm}$, we see that the cut-off length is very short, of the order of a_0.

Based on the results of [62] and [78], it also follows that the bending perturbations of highly viscous liquids grow much faster than the capillary ones (driven by the surface tension), if the condition

$$\frac{\pi\mu^2}{\rho\, e_0^2\,\ell\, n(L/a_0)} \gg 1 \tag{5.63}$$

is fulfilled. For the values of the parameters used in the present section, the left-hand side of Eq. (5.63) is equal to 90.7, which shows that the inequality (5.63), indeed, holds. Therefore, such a jet bends with a nearly constant radius.

5.10. Nonlinear dynamics of bending electrospun jets

To model the way a spatial perturbation develops, we denote the last bead pulled out of the pendant drop and added at the upper end of the jet by $i = N$. When the distance $\ell_{d,N}$ between this bead and the pendant drop becomes long enough, say, $h/25000$, a new bead $i = N + 1$ is inserted at a small distance, say, $h/50000$, from the previous one. At the same time a small perturbation is added to its x and y coordinates,

$$\begin{aligned} x_i &= 10^{-3} L_{e\ell} \sin(\omega t), \\ y_i &= 10^{-3} L_{e\ell} \cos(\omega t). \end{aligned} \tag{5.64}$$

Here, ω is the perturbation frequency. The condition that the collector at $z = 0$ is impenetrable is enforced numerically, and the charge on each element of the jet is removed as it arrives at the collector. Such a calculation mimics the development of the electrically driven bending instability. The calculation begins with only two beads, $N = 2$. As the jet flows, the number of beads in the jet, N, increases. In the cases when evaporation and solidification were not accounted for, the system of Eqs. (5.29) and (5.37) was solved numerically, assuming that the stresses σ_{ui} and σ_{di}, and the velocity $d\mathbf{r}_i/dt$ were zero at $t = 0$. The equations were made dimensionless by the same scale factors as those in Sec. 5.3. Since here it is necessary to account for the surface tension and for the perturbing displacements, two new dimensionless groups emerge in addition to those of Eqs. (5.6)

$$A = \frac{\sigma \pi a_0^2 \mu^2}{m L_{e\ell}^2 G^2}, \tag{5.65a}$$

$$K_s = \frac{\omega \mu}{G}. \tag{5.65b}$$

The last dimensionless group needed in this case is formed by dividing the distance h, from the collector to the pendant droplet, by $L_{e\ell}$,

$$H = \frac{h}{L_{e\ell}}. \tag{5.66}$$

In cases when evaporation and solidification are accounted for, all the dimensionless groups of Eqs. (5.6), (5.65) and (5.66) now contain μ_0 and G_0. Two new dimensionless groups appear: the Deborah number

$$De = \frac{\mu_0/G_0}{a_0^2/D_a}, \tag{5.67}$$

representing the ratio of the relaxation time $\theta_0 = \mu_0/G_0$ to the diffusional characteristic time a_0^2/D_a, and

$$\delta = \frac{L_{e\ell}\, a_0}{(\mu_0/G_0)\, \nu_a}. \tag{5.68}$$

The latter, as well as A in Eq. (5.65a) and H in Eq. (5.66), is based on the "electric" characteristic length $L_{e\ell}$ introduced in Sec. 5.3. The group δ is involved in the calculation of the Reynolds number Re introduced in Sec. 5.8.

5.10.1. Jet path calculated for the electrically driven bending instability without accounting for evaporation and solidification

Now consider the development of small perturbations into a bending instability in a jet without accounting for evaporation and solidification. We estimate the charge carried by the jet to be $1\,\mathrm{C}/\ell$, which is of the same order as the values measured [24]. We also estimate that the relaxation time θ is 10 ms, a_0 is 150 μm, ρ is $10^3\,\mathrm{kg/m^3}$, h is 2 m, V_0 is 10 kV, σ is $0.07\,\mathrm{kg/s^2}$, and μ is $10^3\,\mathrm{kg/(m{\cdot}s)}$. The value of μ is taken to be much larger than the zero-shear viscosity μ_0 reported [24], since the strong longitudinal flows we are dealing with in the present work lead to an increase, by several orders of magnitude, of the elongational viscosity from μ_0 [62, 69, 83, 84]. The dimensionless parameters are as follows: $Q = F_{ve} = 78359.6$, $V = 156.7$, $A = 17.19$, and $H = 626.9$. The length scale is $L_\ell = 3.19$ mm. The charge on the bead $e = 8.48\,(\mathrm{g^{1/2}cm^{3/2}})/\mathrm{s} = 2.83 \cdot 10^{-9}$ C. The mass on each bead is $m = 0.283 \cdot 10^{-8}$ kg. The value of K_s is taken as 100. Since $\theta = \mu/G = 10$ ms, this value corresponds to $\omega = 10^4\,\mathrm{s^{-1}}$, which is in the frequency range of typical noise in the laboratory.

Figures 5.15(a-e) illustrate the development of a typical jet path. The time periodic perturbations, Eqs. (5.64), that grow along the jet develop nonlinear loops of the bending instability. The jet flows continuously from the pendant drop in response to the electric field established by the externally applied potential between the droplet and the collector. This electric field also causes the jet to be charged as it leaves the pendant drop. At $\bar{t} = 0.99$ in Fig. 5.15(e) the instantaneous path of the jet is similar to the patters recorded in experiments using a high-speed video camera such as those shown in Fig. 5.2. It is emphasized that the stresses σ_{ui} and σ_{di} are positive along

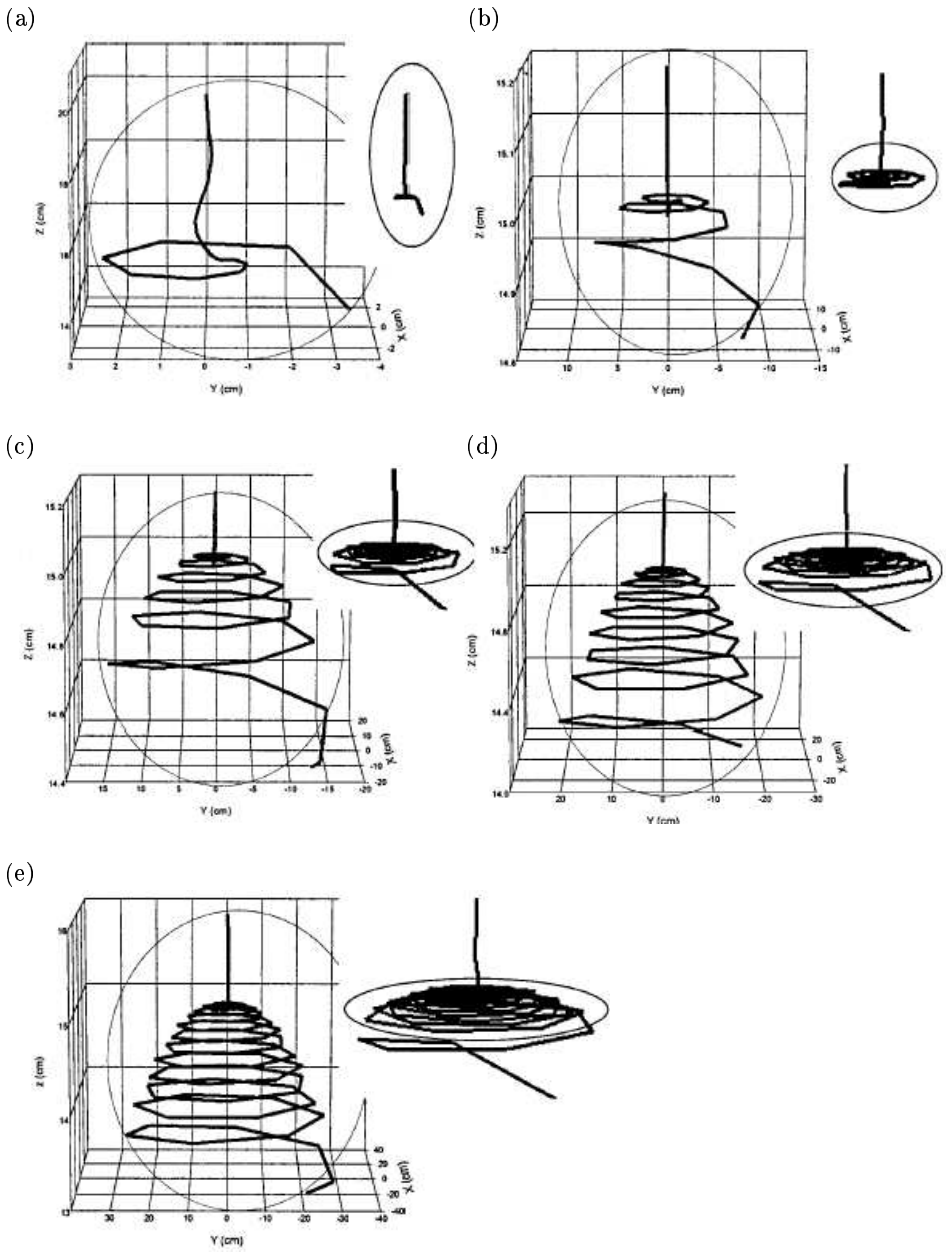

FIGURE 5.15. Perturbations develop into a bending instability. The dimensionless groups have the following values: $Q = F_{ve} = 78359.6$, $V = 156.7$, $A = 17.19$, $K_s = 100$, $H = 626.9$. (a) $\bar{t} = 0.19$, (b) 0.39, (c) 0.59, (d) 0.79, and (e) 0.99.

the entire jet in Figs. 5.15(a-e), which means that the whole jet is stretched continuously.

In Fig. 5.15, a long segment near the vertex of the envelope cone is plotted in the x, y, and z coordinates at various times and scales to show details of the jet path. The entire length of both the straight segment and the spiral part is shown at the same scale in the inset at the upper right of each part of Fig. 5.15. An ellipse in each inset encloses the part of the jet path shown in the corresponding coordinate box. The pendant drop was always at $x = 0$, $y = 0$, and $z = h$.

The experimental evidence shows a self-similar, fractal-like process of development of the electrically driven bending instabilities. The diameter of the first generation of bending loops becomes larger and the jet becomes thinner. Then much small bending perturbations set in on these loops and begin to grow also. This self-similar process continues at smaller and smaller scales until viscoelastic force, surface tension, or solidification of the jet arrest further bending. The numerical results in Fig. 5.15 describe only the emergence and growth of the first cycle of the loops. This is a consequence of the fact that the distances between the beads increase enormously in the simulation of the development of the first cycle. No new beads were added except at the top of the rectilinear segment. Therefore, the capability of the present computer code to elucidate smaller details in the path decreases as the jet elongates enormously.

Figure 5.16 shows the path of a charged jet calculated from a realistic but different set of dimensionless parameters and perturbations than was used in Fig. 5.15. The path displays a bending instability generally similar to that shown in Fig. 5.15.

To show that the bending instability is driven by the Coulomb interaction, the charge, e, on the beads is taken to be zero so that $Q = 0$. The electrical driving force for the bending instability is then zero, but the other parameters are exactly the same as those in Fig. 5.16. If a jet were then pulled downward by gravity, which can supply a downward component of force that acts on the segment in the same way as the downward component of the electrical force from the electrical field, one would expect the uncharged jet to be almost straight in spite of the small perturbations applied to it, since the perturbations would not develop into a bending instability. The calculated result with the same parameters as those in Fig. 5.16, but $Q = 0$, is in fact a straight jet growing downward, even at a later time ($\bar{t} = 8.99$). Increasing

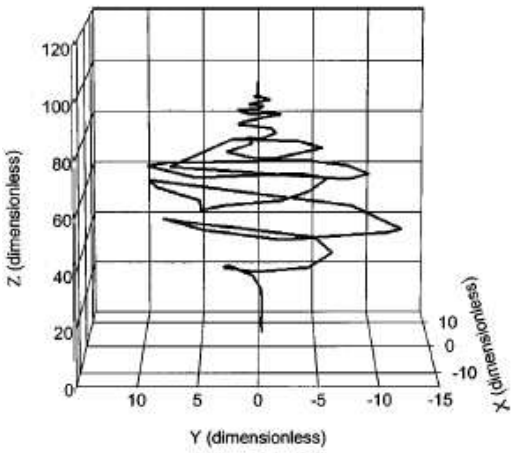

FIGURE 5.16. Charged jet with values of the dimensionless parameters that are realistic but different from those used in Fig. 5.15. $Q = F_{ve} = 12$, $V = 2$, $A = 0.9$, $K_s = 100$, $H = 100$, $\bar{t} = 4.99$.

the ratio of the surface tension to the Coulomb force also stabilizes a charged jet. If A is increased to 9, by increasing the surface tension while all the other parameters are kept the same as those in Fig. 5.16, practically no bending occurs. The results for the gravity driven jet and for the high surface tension jet are not shown because the calculated jet path cannot be distinguished from a straight line at the scale in Fig. 5.16.

5.10.2. Jet path calculated for the electrically driven bending instability accounting for evaporation and solidification

As was shown in Sec. 5.10.1 the qualitative pattern of the jet behaviour in the electrospinning process can be drawn without accounting for evaporation and solidification. A quantitative comparison can be made only accounting for evaporation and solidification. Such a comparison is the aim of the present section. Also, a comparison between the results obtained with and without accounting for evaporation and solidification will be made here.

Calculations of the present work were done for an aqueous solution with an initial 6% concentration of poly(ethylene oxide) studied experimentally as described in Sec. 5.2. The following values of the dimensional parameters were established: the initial cross-sectional radius $a_0 = 150\,\mu$m, the density $\rho = 10^3\,\mathrm{kg/m^3}$, the surface tension $\sigma = 0.07\,\mathrm{kg/s^2}$, the initial viscosity

$\mu_0 = 10^3\,\mathrm{kg/(m{\cdot}s)}$, the initial relaxation time $\theta_0 = 10\,\mathrm{ms}$, the charge density $1\,\mathrm{C}/\ell$, the distance to the collecting plate $h = 20\,\mathrm{cm}$. In the calculations of the present work we took the field strength $U_0/h = 1.5\,\mathrm{kV/m}$. In the experiment the electric field was $50\,\mathrm{kV/m}$. The values of the dimensionless groups introduced in Eqs. (5.6), (5.65) and (5.66) are now based on the initial values of the dimensional parameters and are equal to $Q = F_{ve} = 78359.57$,

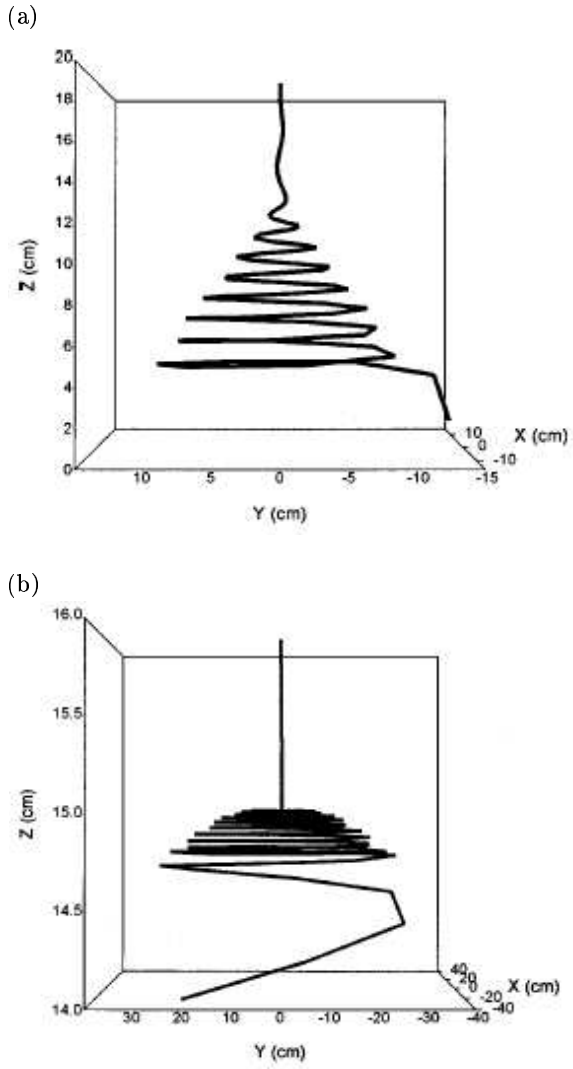

FIGURE 5.17. (a) Jet path calculated accounting for evaporation and solidification. (b) Jet path calculated without accounting for evaporation and solidification.

$V = 47.02$, $A = 17.19$, $K_S = 100$ and $H = 626.88$, whereas $L_{e\ell} = 0.319\,\mathrm{cm}$. We also took the humidity of 16.5%, $c_{s\infty} = 0.165$, and the temperature of 20°C. The best representation of the envelope cone of the bending loops (see below) was found at $B = 7$ and $m = 0.1$ in the solidification law (5.52), (5.55) and (5.56), which agrees with the estimates known from the literature and those discussed in the previous sections. These values were used in the present calculations.

Figure 5.17(a) shows the path of the jet accounting for evaporation and solidification, whereas Fig. 5.17(b) was calculated without accounting for these effects. Due to the evaporation and solidification each loop of the jet becomes more viscous with time, and its elastic modulus increases. As a result, the bending stiffness increases, and the radius of the bending loops in Fig. 5.17(a) (with the evaporation and solidification) is smaller than that of Fig. 5.17(b) (without the evaporation and solidification). The radius of the bending perturbations of the jet calculated accounting for the evaporation and solidification effects is well comparable with that found in the experiment (cf. Fig. 5.2), which is illustrated in the following section.

5.10.3. Envelope cone

Shape of the envelope cone can be easily seen by a naked eye, or using a camera with long exposure time (cf. Fig. 5.18). The two bright lines bifurcating in Fig. 5.18 from a point emphasized by the arrow resulted from a specular reflection of light from segments near the maximum lateral excursion of each loop. Each loop moved downward during a long exposure time of the camera and created the bright lines seen in Fig. 5.18, which define the envelope cone of the bending jet during the electrospinning process. For comparison with the results of the calculations, the generatrix of the envelope cone in Fig. 5.18 is also represented in Fig. 5.19.

The calculations showed that the evaporation and solidification have a strong effect on the predicted shape of the envelope cone. Two theoretical curves: without evaporation and solidification, and with these effects accounted for ($m = 0.1$) are presented in Fig. 5.19. It is clearly seen that the result accounting for evaporation and solidification agrees fairly well with the experimental data.

The envelope visible in the experiment does not extend beyond a radius of about 3 cm, whereas the theory allowed for further growth of a radius

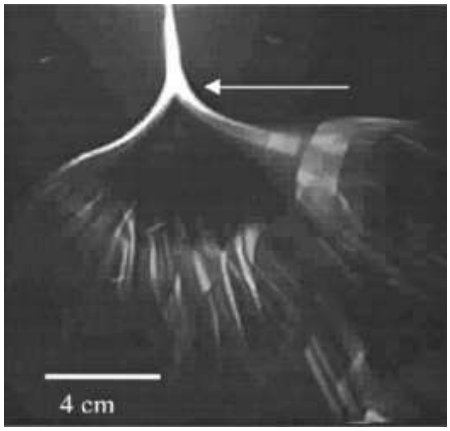

FIGURE 5.18. Shape of the envelope cone created by the electrically driven bending instability. The complicated image in the lower part of the figure is a consequence of the long exposure time ($\sim$ 16 ms) used to observe the envelope cone, and the time varying path of the jet in that region.

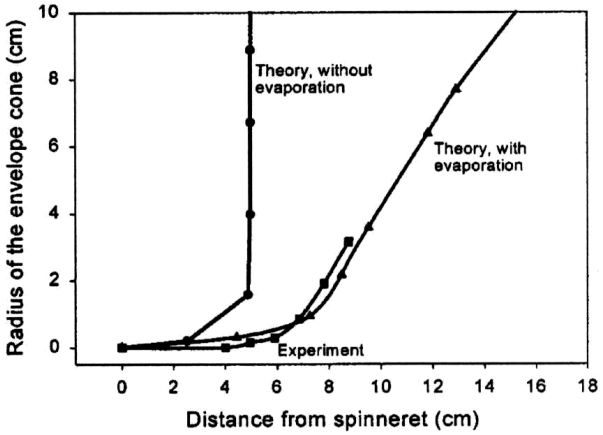

FIGURE 5.19. Shape of the envelope cone: experiment vs theory. Points show calculated radii of successive loops. Experimental points were measured from a photograph.

until 10 cm. The reason may be that after the jet had solidified in the experiment, it became much more rigid, i.e. unstretchable. On the other hand, in the theoretical calculations the solidified jet is still described as a liquid (albeit highly viscous, with a high elastic modulus), which still allows for some additional stretching. Actually, the comparison in Fig. 5.19 shows that

the calculations should be stopped as the radius of the envelope cone has achieved the value of 3-4 cm.

5.10.4. Jet velocity

Downward velocity in the electrified jet was measured by following the downward motion of a loop. The comparison of the experimental and theoretical results is shown in Fig. 5.20. The velocity is practically independent on time in both experiment and theory. The theoretical value of the velocity overestimates the measured by a factor of four. Given the fact that the values of several governing parameters used in the experiments are only an order of magnitude estimates, the discrepancy represented by the factor of four is not dramatic.

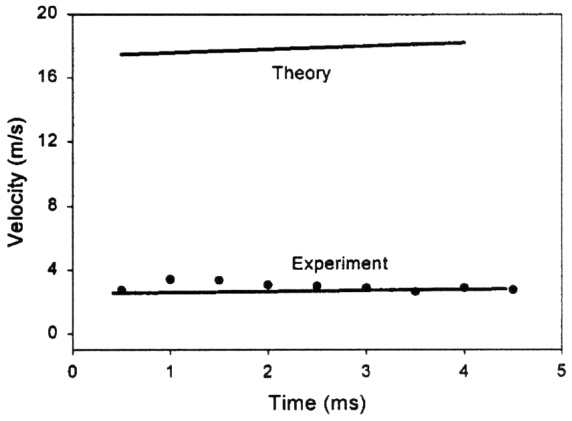

FIGURE 5.20. Downward velocity of the jet: experiment vs theory. $B = 7$, $m = 0.1$.

5.10.5. Elongation and drying of the jet

The theoretical results suggest that the stretching of material elements along the jet makes it possible to achieve very high draw ratio values in the electrospinning process. In the calculation the initial distance between two successive beads was $3.99 \cdot 10^{-4}$ cm, whereas the final distance was 13.92 cm. Assuming that the initial polymer concentration in the jet was 6%, the cross-sectional radius of a dry fiber (a_f), after elongation and solvent evaporation have been completed, is related to the initial radius of the jet (a_0), by the

material balance equation

$$\pi a_f^2 \cdot 13.92 = \pi a_0^2 \cdot 3.99 \cdot 10^{-4} \cdot 0.06. \tag{5.69}$$

For $a_0 = 150\,\mu$m this yields $a_f = 196.7\,$nm. The corresponding draw ratio due to elongation is equal to $(a_0/a_f)^2 \cdot 0.06 = 34815$. It is emphasized that if the jet would be straight and stationary, like in the ordinary fiber spinning processes, the ratio of the fiber velocity at the winding bobbin V_f to the initial one in the spinline V_0 becomes

$$V_f = V_0 \frac{\pi a_0^2 \cdot 0.06}{\pi a_f^2} = 34815\, V_0. \tag{5.70}$$

For the experimentally measured value of $V_0 \cong 0.1\,$m/s the velocity V_f would be

$$V_f = 3481.5\,\text{m/s} = 10 \times \text{(speed of sound)!} \tag{5.71}$$

This obviously is not true. The paradoxical value of V_f in (5.71) results from the fact that huge elongation of the fiber cannot be achieved at the distance of

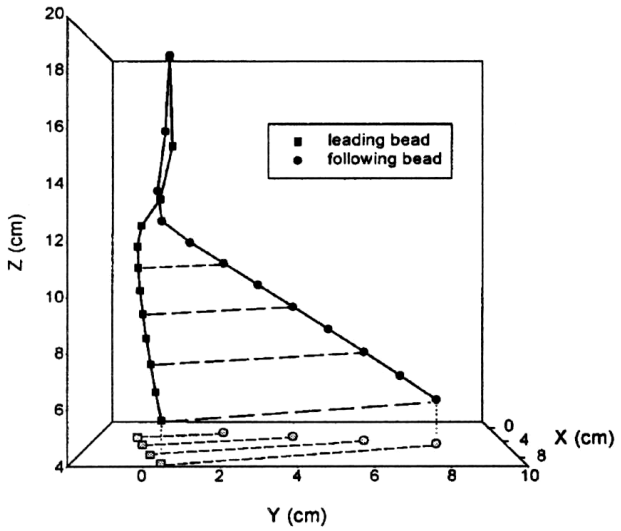

FIGURE 5.21. Stretching of a segment of the jet. Each solid line represents a trajectory of one of the two successive beads. The dashed lines represent the segment of the jet between the successive beads. The length of the segment increases with time as a result of the jet stretching during the course of electrospinning. B=7, m=0.1. The projections of the bead positions onto the X-Y plane are shown by the gray symbols.

about 10 cm along a straight line. The electrically driven bending instability supplies the mechanism of strong elongation via fractal-like looping which allows reduction of the final radius a_f to the range of nanofibers, even though $V_f \cong 1\,\mathrm{m/s}$.

Figure 5.21 shows the trajectories of two successive beads of the jet in the course of electrospinning. The trajectories are shown by solid lines, and the positions of the beads by black squares and circles. The lines that have longer dashes connect the positions of the adjacent beads. To simplify, not every connection is shown. The projections of the dashed line onto the X-Y plane are shown by the lines with shorter dashes. The X-Y projections of the bead positions are shown by gray squares or circles. The dashed lines connecting the two beads at a given time represent the elongating segment. Its increase in length illustrates stretching of the jet element between the two beads. The initial distance between the beads was $3.99 \cdot 10^{-4}\,\mathrm{cm}$ as mentioned above. The time interval covered by Fig. 5.21 is 6.5 ms. A corresponding draw ratio is shown in Fig. 5.22 versus the vertical distance of the segment from the tip. It is instructive to see the envelope cone, too (the dashed line in Fig. 5.22), since it shows where the draw ratio grows. Along the straight part of the jet, which is about 6 cm long, the draw ratio achieves a value of about 1000. In the bending loops inside the envelope cone the draw ratio increases by another factor of 25, to the value of 25000. Without evaporation and solidification

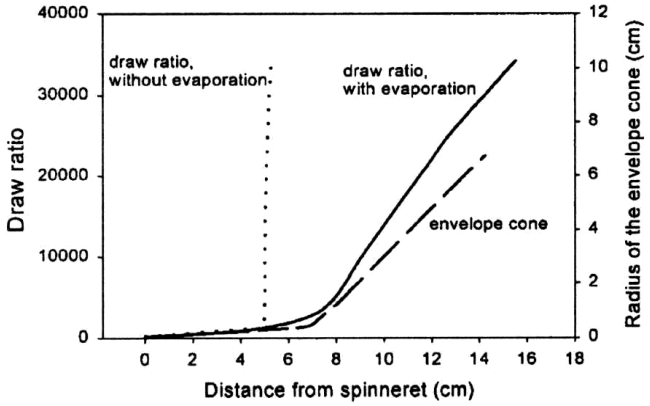

FIGURE 5.22. Calculated draw ratio of a segment of the jet along its length. $B = 7$, $m = 0.1$. The dotted line was generated using the results not accounting for evaporation and solidification.

in the model, the draw ratio extracted from the calculation increased very rapidly, as shown in Fig. 5.22.

5.10.6. Viscosity profile in the bending jet

The distribution of the viscosity along the jet at $t = 6\,\text{ms}$ is shown by solid line in Fig. 5.23. Viscosity slowly increases along the straight part of the jet. When bending perturbations begin to grow rapidly, velocity of the motion increases, and the evaporation process strongly intensifies. It is clearly seen when comparing the viscosity profile with that of the envelope cone shown in Fig. 5.23 by the dashed line. Fast evaporation strongly increases the polymer fraction in the jet, which leads to solidification manifested by the appearance of the high viscosity plateau at a distance of about 2 cm from the beginning of the envelope cone. The calculation showed that at the beginning of the plateau, nanofibers have already been formed, since the cross-sectional radius of the fiber is already about 640 nm.

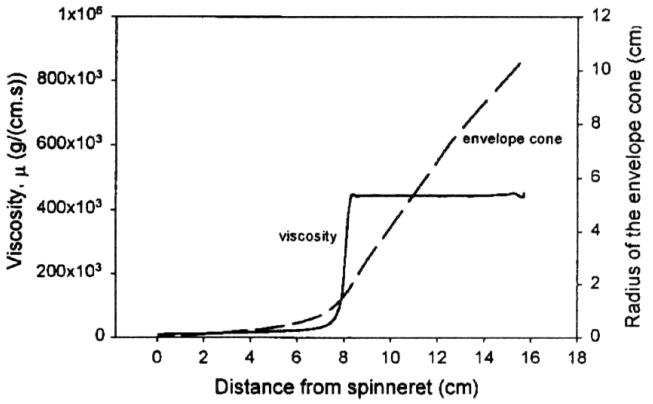

FIGURE 5.23. Calculated viscosity along the jet; $t = 6\,\text{ms}$, $B = 7$ and $m = 0.1$. The calculated radius of the envelope cone continued to grow after the viscosity reached the plateau.

5.10.7. Longitudinal strain rate and molecular orientation

The high value of the area reduction ratio and the associated high longitudinal strain rate imply that the macromolecules in the nanofibers should be stretched and axially oriented. Most electrospun nanofibers, even those made from a styrene-butadiene-styrene triblock copolymer, are birefringent [85].

The longitudinal strain rate was different at different places along the jet. The longitudinal strain rate for three different parts of the jet was determined.

1. The jet velocity in the downward direction was determined from the sequential images by determining the velocity of particular maxima of the growing bending instability and the length of the straight segment. In this work, the length of the straight segment (L_z) was 5 cm and the velocity was 1 m/s. Therefore the longitudinal strain rate was:

$$\frac{\delta L_z}{L_z \delta t} = \frac{V \delta t}{L_z \delta t} = \frac{V}{L_z} = \frac{1\,\mathrm{m/s}}{0.05\,\mathrm{m}} = 20\,\mathrm{s}^{-1}, \tag{5.72}$$

   which is the strain rate in the straight segment of the jet.

2. The observation of expanding loops provided a second measure of the longitudinal strain rate for the segment that formed the loop. A typical loop grew from a diameter of 1 to 8 mm in 7 ms. The resulting longitudinal strain rate in such a loop was 1000 s^{-1}.

3. The overall longitudinal strain rate can be estimated using the data provided in Sec. 5.10.5. The time that a typical segment of the electrospun jet is in flight (δt) can be estimated as the distance between the pendant droplet and the collector (20 cm) divided by the average downward velocity of the jet (1 m/s). The resulting δt is 0.2 s. The longitudinal strain rate is $\delta\zeta/(\delta t\,\zeta)$, where ζ is the initial segment length, and $\delta\zeta$ is the growth in length. Since $\delta\zeta$ is much greater than ζ, $\delta\zeta$ is approximately the final segment length. The ratio $\delta\zeta/\zeta$ was around 10^5, and therefore the longitudinal strain rate was around $0.5 \cdot 10^6\,\mathrm{s}^{-1}$. Using the estimate, Eq. (5.72), we find that in the straight segment the length of a liquid element has been approximately doubled, and the cross-sectional radius decreased by a factor of four. Then the longitudinal strain rate in the loops becomes of the order of $10^5\,\mathrm{s}^{-1}$. The actual value will be lower due to the effects of evaporation and solidification.

Theory suggests that the transformation from a random coil to a stretched macromolecule occurs when the strain rate multiplied by the conformational relaxation time of the molecule is greater than 0.5 [83, 84]. Since the relaxation time of the polymer solution is about 0.01 s, then $\delta\zeta/(\delta t\,\zeta)$ multiplied by the relaxation time was equal to $10 \div 10^3$, which is much greater than 0.5. Therefore, the longitudinal flow in the electrospun jet is strong, and the macromolecules are likely to be stretched in the direction of the jet axis.

5.11. Concluding remarks

The entire electrospinning process and the electrically driven bending instabilities of an electrospun fluid can each be viewed as particular examples of the very general Earnshaw theorem in electrostatics. This theorem leads to the conclusion that it is impossible to create a stable structure in which the elements of the structure interact only by Coulomb's law. Charges on or embedded in a polymer fluid move the fluid in quite complicated ways to reduce their Coulomb interaction energy. Electrospinning, and perhaps other useful processes, utilize this behaviour to produce interesting and useful polymer objects.

The localized approximation introduced in the present section utilized a far-reaching analogy between the electrically driven bending instability in the electrospinning process and the aerodynamically driven bending instability studied before [62, 78]. The quasi-one-dimensional partial differential equations of the jet dynamics that describe the course of electrospinning were established.

A reasonably quantitative description of the experimental data was achieved, which allowed us to calculate the shape of the envelope cone, which surrounds the bending loops of the jet in the course of electrospinning. The downward velocity of the jet can also be calculated to be within an order of magnitude of the observed velocity. The theoretical results also allow for the calculation of the elongation of material elements of the jet. The calculated results also illustrate the increase in viscosity of segments of the jet as the solvent evaporates during the course of electrospinning.

It is emphasized that presently, information on the rheological material behaviour of polymer solution being elongated at the rate and other conditions encountered during electrospinning, is rather scarce. Data on evaporation and solidification of polymer solutions in the electrospinning process are practically unavailable. Therefore, at present a number of the parameters in this calculation can only be estimated by the order of magnitude, or found from experimental observations of the electrospinning process. Material science data acquired for the electrospinning process will allow researchers to avoid such obstacles in future. A more detailed description of the nature of the solvent (in this case, a mixture of water and ethanol with a variable evaporation rate) may also be very helpful for a further upgrading of the present model.

Chapter 6

Scientific and technological challenges in producing nanofibers with desirable characteristics and properties

Electrospinning has been shown to be an effective method for the production of nanofibers. For most applications, it is desirable to control, in addition to the diameter of the fibers, also the architecture, the internal composition, the internal morphology and the surface topology as well as fibers alignment in a structure. Porous fibers are of interest, for instance, for filter applications. Core-shells fibers or fibers, which are hollow, are of interest for storage, release systems, insulation, etc. A given surface topology will affect, for instance, the wetting behavior (super-hydrophobicity), as well as specific adsorption processes [86−88], and it will couple very effectively to the surrounding matrix in the case of reinforcement. The objective is to tailor the fiber formation during electrospinning in such a way that fibers with specific diameters, architectures, internal structures and surface topologies are manufactured and aligned, specified in view of the targeted application.

A further objective is the inclusion of specific additives-drugs, catalysts, nonlinear optical materials, electrically conducting and photosensitive materials, chromophores, etc. into the fibers, possibly only in well-defined compartments within the fibers. Chemical modifications, functionalizations on the fibers, again directed at optimizing the properties for specific applications, are highly desirable.

First successes in preparation of conductive and photosensitive nanofibers from electronic and photonic polymers [89−92] show that electrically con-

ducting and light-emitting nanofibers/ nanotubes are relatively easily achievable via electrospinning.

Electrical conductivity and strength of nanofibers can be significantly improved if single- and multi-wall carbon nanotubes (CNTs) (see the recent reviews in [93] and [94]) were incorporated into them. The first attempts in this direction show that nanofibers containing CNTs can be electrospun from a polymer-based solution of CNTs [95, 96]. The most important issue to be tackled when electrospinning polymer-CNT solutions, is the achievement of a fine and stable dispersion of CNTs. This is doable by desolving CNTs in solutions of surfactants (e.g. in sodium dodecyl sulfate, SDS [97], or in a nonionic surfactant like Triton X at low concentration). In these systems, the amphiphilic character of the surfactant stabilizes a colloidal suspension in water. However, there is no evidence that this process separates the CNT bundles into individual tubes. In fact, viscosity measurements performed on these systems revealed a low viscosity (as that of water) [97], which demonstrates the colloidal/aggregated character of these suspensions.

Another approach to disperse nanotubes is based on introducing nanotubes with attached polymers [98−100].

A new, simple one-step process was recently reported using a natural polysaccharide, Gum Arabic, to disperse single-wall carbon nanotubes, SWNTs, in aqueous solutions [101].

Combination of both electrostatic and steric repulsion interaction in aqueous dispersion can be achieved by attaching a block or grafted copolymer to the particles where the hydrophilic block is charged [102].

The stabilized dispersions of CNTs in surfactant solutions are mixed at the following stage with polymer solutions [97]. In the latter work, a rather simple way to assemble SWNTs into a macroscopic long ribbon or fiber was proposed. By pumping the SWNT-PVA solution, a long ribbon without entanglements could easily be drawn out. Young's modulus of these fibers after rinsing and drying varied between 9-15 GPa, which is much lower than for the individual nanotubes, but is one order of magnitude greater than the modulus of the "bucky paper". X-ray diffraction of these fibers [103] has shown that the nanotubes preferentially oriented along the fiber axis.

Another method to process nanotube dispersions was demonstrated in [95, 96], and [104], using the electrospinning technique. In the latter works, carbon nanotubes were dispersed in a solution of polyurethane in DMF (dimethylformamide) and polyaniline to produce a spinnable solution (10%

polymer, 10% carbon nanotubes and 80% DMF). The solution was electrospun, resulting in a composite nanofiber enclosing oriented clusters of nanotubes along its axis.

Conducting and photosensitive nanofibers can be obtained not only by electrospinning, but also via different chemical and electrochemical synthesis methods and template methods [105–109]. However, these nanofibers are always very short ($\sim$ several μm) as compared to the electrospun nanofibers ($\sim$ 10 cm and more).

Some additional details on scientific and technological challenges related to electrospinning of biofunctional, conducting and photosensitive nanofibers, will be given below in the sections devoted to these particular topics.

To overcome technological challenges in fabrication of microdevices, techniques for in situ alignment of as-spun nanofibers/nanotubes using electrostatic repulsion forces [28, 110, 111] have recently been demonstrated as a route for alignment of nanofibers/nanotubes.

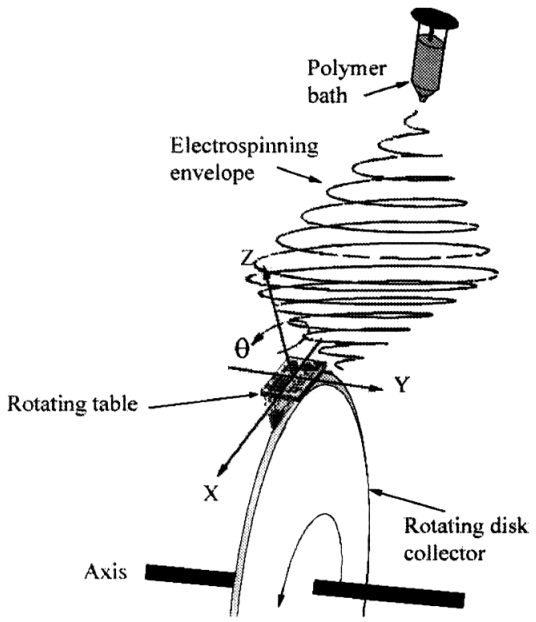

FIGURE 6.1. Schematic drawing of the electrospinning process, showing the double-cone envelope of the jet. The collector disk is equipped with a table that assists to collect the nanofibers. The table can be rotated about the Z-axis when the disk rotation is temporarily stopped to enable layer-by-layer collection at a desired angle between the nanofiber array layers.

A sketch of the experimental apparatus is shown in Fig. 6.1 [1)]. The jet flows downward from the surface of a pendant drop of polymer solution toward a rotating disk collector at a distance of 120 mm below the droplet. The disk was made of aluminum (with a diameter of 200 mm) and had a tapered edge with a half angle of 26.6° in order to create a stronger converging electrostatic field (an electrostatic lens). An electric potential difference of around 8 kV was created between the surface of the liquid drop and the rotating disk collector. At the beginning of the experiment, a pendant droplet of polymer solution was supported at the tip of the exit. When the potential difference between the droplet and the grounded wheel is increased, the droplet acquires a cone-like shape (the Taylor cone). At a certain potential difference, a stable jet emerged from the cone and moved downward toward the wheel. After the jet flowed away from the droplet in a nearly straight line, it bent into a complex path that can be described by an envelope cone. Then, at a certain point above the wheel the envelope cone started to shrink, resulting in an inverted envelope cone with its apex at the wheel's edge.

During the electrospinning process, the disk was rotated at a constant speed to collect the developing nanofibers onto its sharp edge. The linear speed at the tip of the disk collector was $V = 11\,\mathrm{m/s}$. As the spun fiber reached the wheel's edge, it was wound around the wheel.

A small table (5×4 mm) made of aluminum was attached to the disk edge to facilitate the collection of the nanofibers and to detach them further on. The table can be rotated about its Z-axis when the disk rotation is temporarily stopped, hence the direction of the collected nanofibers can be controlled. The nanofibers were collected over a 10 sec period. The collected two-dimensional nanofiber arrays are shown in Fig. 6.2. The diameter of the nanofibers is not uniform and varies from 100 to 300 nm in Fig. 6.2(a) and from 200 to 400 nm in Fig. 6.2(b). The separation between the parallel nanofibers is not completely uniform and varies from 1 to 2 μm in Fig. 6.2(a) and from 1 to 1.5 μm in Fig. 6.2(b). Typical three-dimensional nanofiber arrays (crossbars) are depicted in Fig. 6.3. A single junction is shown in Fig. 6.4. The collected nanofibers show a high order of alignment. The diameter of the nanofibers in this case is also non-uniform and varies in the range 10-80 nm. When nanofibers were electrospun onto the wheel's sharp edge without the table, ropes of nanofibers were obtained. A typical image of a rope of nano-

[1)] These results were published by A. Theron, E. Zussman and A.L. Yarin in [28] and [111].

(a)

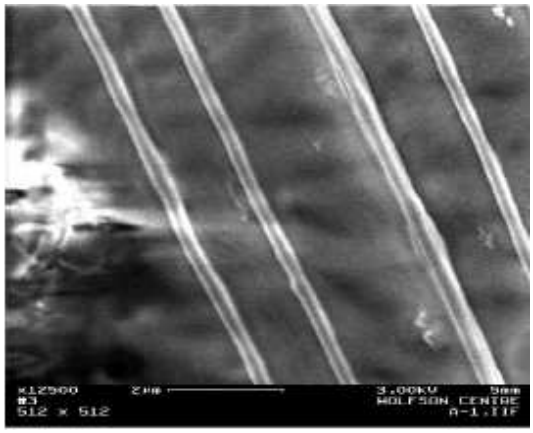

(b)

FIGURE 6.2. HR-SEM images of aligned NFs that were collected on a carbon tape attached to the edge of the disc collector. In (a), the diameter of the fibres varies from 100 to 300 nm. The pitch (centre to centre) varies from 1 to 2 μm. In (b), the diameter of the fibres varies from 200 to 400 nm. The pitch varies from 1 to 1.5 μm.

fibers is shown in Fig. 6.5. The duration of the collection process was 60 s. The rope was manually detached from the wheel edge. An HR-SEM image of the rope is shown in Fig. 6.6. The nanofibers are in contact, and their parallelism is high.

Arrays similar to those shown in Figs. 6.2- 6.4 represent themselves as key elements of light-emitting diodes (LEDs), polymer lasers, and photonic crystals – a composite of a periodic array of dielectric scatterers in a homogeneous

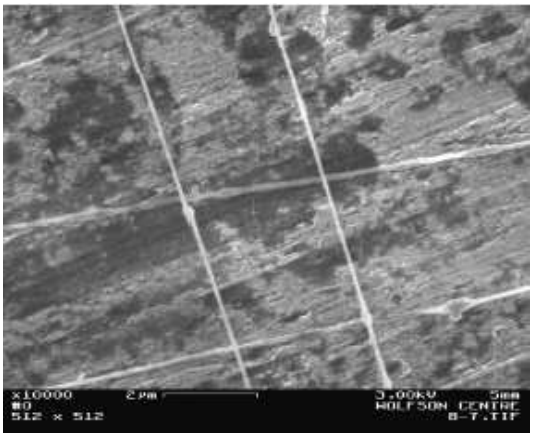

FIGURE 6.3. Typical SEM image of crossed arrays of PEO based nanofibers collected on an aluminum table. The structure was obtained in a two-step assembly process with orthogonal placement directions for the sequential steps.

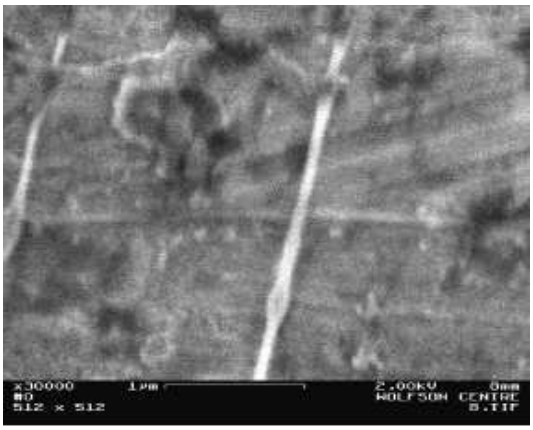

FIGURE 6.4. A junction of the nanofiber crossed array.

dielectric matrix. These devices affect the properties of a photon similar to a semiconductor effect on the properties of an electron. As a result, photons can have band structures, localized defect modes and surface modes. A foreseen ability to mold and guide light can enable a variety of novel applications of nanofibers/nanotubes in such fields as microelectronics, telecommunications, solar energy conversion, medical and pharmaceutical industry.

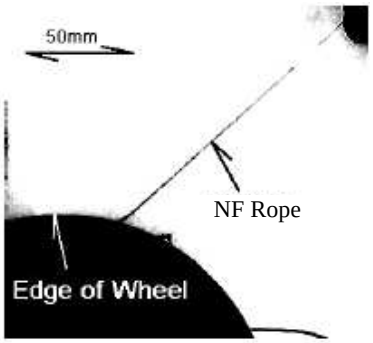

FIGURE 6.5. A rope of aligned NFs manually pulled from the collector. Almost all the NFs were collected on the edge of the sharpened disc collector.

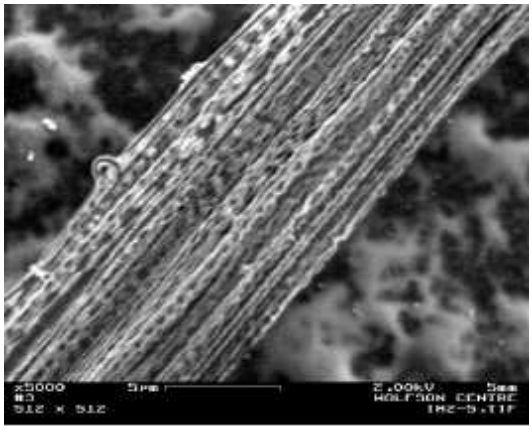

FIGURE 6.6. Typical HR-SEM image of a rope of aligned NFs. The density is about 100 NFs μm^{-2}.

For short nanofibers and nanowires prepared by methods other than electrospinning, various assembly methods were proposed, i.e. electric-field assisted assemby [112] and micro- fluidics methods [113].

Chapter 7

Characterization methods and tools for studying the nanofiber properties

Morphological characterization of nanofibers and nanotubes should allow recognition of their crystalline or amorphous structure, spherulites, internal defects, and complex internal structures (i.e. incorporated solid particles, CNTs, etc.). The degree of crystallinity, the crystal orientation and the crystal modifications present can be investigated in this way. X-ray scattering and diffraction traditionally employed for textile fibers, have already been demonstrated as a useful tool in characterization of nanofibers [114]. Wide-angle X-ray scattering (WAXS), wide-angle X-ray diffraction (WAXD) and small angle scattering are very useful for these aims. In particular, Philips diffractometer for WAXD with the Bragg-Brentano scheme for beam focusing is extremely helpful.

However, using only X-ray scattering measurements it is rather difficult to arrive at unambiguous conclusions, especially in the case of nanofibers containing nanoparticles and CNTs as well as different defects (cracks, necks, etc.), and nanotubes with internal boundaries. Supplementary techniques for morphology characterization are available and should be used. These include scanning electron microscopy (SEM), and transmission electron microscopy (TEM) [28, 34–37, 114]. The latter is extremely helpful in the case of compound nanofibers and nanotubes, as well as nanofibers containing CNTs.

Characterization of tensile stress and elastic and plastic properties of nanofibers, as well as fractographic analysis [115], are extremely important

for applications. Conventional tensile testing machines used for characterization of textile fibers cannot be applied to nanofibers. Application of various microstages and low-load commercial tests (like a Housfield H1KS machine with a 5N load cell) is called for [116]. Composites of nanofibers in epoxy resin were tested using a double torsion fracture test setup in [117]. Three points bending tests were carried out using atomic force microscopy (AFM) [118]. AFM was also used to measure nanofiber dimensions and nanofiber-array structures in [28].

Using microstages and tensile machines (even the smallest ones), it is possible to make measurements only with samples of non-woven nanofiber-based materials or oriented nanofiber ropes [28]. In particular, non-woven samples were tested in relation to tissue engineering scaffolds [119–121], where it was shown that these materials could fit the properties of natural skin (i.e. tensile modulus, ultimate tensile stress, and ultimate tensile strain). At present only AFM allows for studying mechanical properties of a single nanofiber.

Surface characterization and porosity of electrospun nanofibers (in particular, biocompatible ones) and nanotubes can be achieved using SEM images [34–37, 122].

The surface energy and the wetting behaviour are studied by corresponding tensiometers. Functionalized nanofibers and nanotubes containing specific groups such as dipolar groups or chromophores are analyzed via absorption and fluorescence spectroscopy and dielectric relaxation studies as far as dipolar groups are concerned.

In the case of nanofibers containing carbon nanotubes, orientation of the latter can be detected by Raman spectroscopy [123]. In the case of conducting and photosensitive nanofibers, electrical and optical measurements are called for. Current-voltage curves of polyaniline-based nanofibers were measured using a non-woven mat collected on a silicon wafer [90]. Two gold electrodes separated by $60.3\,\mu$m were deposited on the fiber after its deposition on the substrate. For the steady-state photoluminescence measurements, the samples can be excited by a monochromatic illumination at a wavelength of about 470 nm. The emission is measured through a polarizer, which is placed in front of a monochromator and a photo-multiplication detecting system (PMT).

Additional details on challenges in electrospinning of conducting and photosensitive nanofibers will be given below in the section devoted to them.

Rheological characterization of the viscoelastic polymer solutions used for electrospinning is very poor at present. It should involve uniaxial elongational rheometry at high strain rates. In this context elongational rheometers of the type discussed in [62, 63, 124, 126] and [127], can be very helpful to characterize spinnability and rheological parameters of the solutions depending on polymer type and concentration.

Polymer solutions used in electrospinning can be characterized as leaky dielectrics [128, 129]. The nature of the ions involved is typically unknown. Therefore, electric characterization of the solutions intended for measuring their electric conductivity and dielectric permeability is highly desirable. Electric field and current affect the shape of the transitional region connecting the Taylor cone and the jet. Experimental studies should reveal a relation between the electric and fluid mechanical parameters, which is also affected by the electric conductivity and dielectric permeability of the leaky dielectrics [130]. Such studies can be facilitated by the theoretical solutions for the transition region found in [131−137].

Non-circular cross-sectional shapes and garland-like structures developing in certain nanofibers were revealed by morphological analyses in [137] and [138].

Chapter 8

R&D needed for development and application of several specific types of nanofibers

8.1. Biofunctional (bioactive) nanofibers for scaffolds in tissue engineering applications

Electrospinning of scaffolds for tissue engineering applications follows the standard trend characteristic of electrospinning of the other polymer materials. For scaffold applications polymer solutions are electrospun from the tip of a pendant or sessile drop at the edge of a syringe needle by applying electric potential differences of the order of 10 kV, or the field strengths of the order of 1 kV/cm [119−122]. Nanofibers are collected on a ground plate as a non- woven mat [119, 121, 122], or on a rotating mandrel [120]. The latter introduces slight orientation in the electrospun mats. The fact that scaffolds should be biodegradable determines which polymers should be used. For example, Poly(glycolic acid) (PGA), Poly(l-lactic acid), Polycaprolactone (PCL), and their copolymers (e.g. PLGA) were electrospun for these purposes. These materials have many favorable properties, although unfortunately these polymers have not performed up expectation in the clinical setting [120]. That is the reason that such natural materials like collagen prepared from calfskin and from human placenta were used to electrospin skin scaffolds [120].

Scaffold engineering includes an additional non-trivial stage at which scaffolds are submerged into a bath with cellular cultures. Cells are expected to be able to attach to the electrospun mat and proliferate into it. Therefore,

such design criterion of an ideal engineering scaffold should be met as the favorable cell-matrix interaction, and an active biocompatibility of the structure [121]. The results of [121] show that this is in principle possible for mouse fibroblasts and human bone-marrow-derived mesenchymal stem cells on Poly (D,L-lactide-co-glycolide) (PLGA) nanofibers. This opens a green light for scaffolding human skin and cartilage, as well as cardiovascular and bone-like materials (to make the latter, cells should be calcium producing, which fortifies the structure). Moreover, the results of tensile tests show [119, 121] that electrospun structures possess tensile modulus of the order of 323 MPa comparable with that of cartilage (130 MPa) and skin (15-150 MPa). The ultimate tensile stresses are also close (23, 19 and 5-30 MPa, respectively), as well as the ultimate tensile strains (96, 20-120 and 35-115%, respectively).

The effective pore diameters for cell ingrowth into a non-woven mat are between 20 and 60 μm while for bone ingrowth 75 to 150 μm are required [121]. If in a non-woven mat of nanofibers the latter are not merged, cells are able to push nanofibers aside. Therefore, even the smallest pores become appropriate for cell ingrowth.

There are some indications that smooth muscle cells can better infiltrate a slightly oriented matrix [120]. This conclusion should be checked using fully oriented matrices produced by the method of [28]. Using this method it is possible to fabricate complex, seamless, three- dimensional scaffolds for tissue engineering.

To the best of our knowledge, nanofibers or oriented nanofiber ropes still have not been used for nerve regeneration. The method of [28] can easily be applied for fabrication of oriented ropes of conducting nanofibers, which can be tested as nerve substitutes.

Nanofiber scaffolds in tissue engineering should be both strong and biologically compatible. One of the possible candidates as a scaffolding material is spider silk [115, 139, 140]. Spider dragline silk is stronger than Kevlar and stretches better than nylon, and it also might be biologically compatible. This combination of properties is seen in no other fiber. Numerous trials to domesticate spiders and to raise spiders on a farm failed. However, there is a way to utilize spider silk, which was recently developed via gene engineering and polymer science. Namely, spider dragline silk genes were spliced into mammalian cells. It was shown that this resulted in secreting soluble silk proteins outside the cells where they could easily be collected [139, 140]. One can imagine a goat or a cow secreting spider silk proteins into milk, from

where they could easily be separated. Spider silk proteins produced using this route have already been formed as fibers of diameters of about 50 μm [139, 140]. They are still not as strong and sophisticated as the natural spider silk. However, the results are quite promising. Electrospinning of the solutions of these proteins is obviously called for, since such nanofibers could become one of the good candidates for scaffolds for tissue engineering and artificial organs.

Nanofiber mats have great potential as scaffolds for synthetic skin and artificial organs.

8.2. Conducting nanofibers: displays, lighting devices, optical sensors

Electrospinning of conducting nanofibers was considered briefly in Chapter 6. In the present chapter, we extend the discussion.

Poly(pyrrole), Polyaniline, PEDOT, PPV and MEH-PPV (Poly(2-methoxy, 5-(2'-ethyl-hexoxy)-p-phenylenevinylene) were the conducting conjugated polymers which deserved the most attention from the researchers dealing with fiber and nanofiber applications. The interest is related first of all to their possible applications in micro- and opto-electronics. Conjugated polymer light emitting diodes (LEDs) have been examined as polarized emission structures for such applications as displays and lighting [141, 142]. The intrinsic anisotropy of their electronic structure means that, provided they can be oriented into a specific direction, polarized emission will occur. Required polarization ratios depending on specifications should be up to 200:1 to allow complete removal of the power inefficient external polarizers [143]. In order to optimize the broad range of the electrical properties of conjugated polymers, a variety of processing techniques has been developed focusing on chain extension and chain alignment, with the goal of improving the structural order to the point that the intrinsic properties of the macromolecular chains can be achieved. These techniques include mechanical alignment by rubbing, stretching [144], or alignment of luminescent "guest" molecules in a "host" polymer matrix [145]. However, further improvement in material quality is necessary to enable the exploration of the intrinsic electronic properties of conjugated polymers, as well as improvement of the ability to fabricate thin media for creating power efficient devices with low voltage operation. Most of the research until now was concentrated on luminescent thin films [141−145].

Electrospinning represents a very promising technique for fabrication of luminescent nanofibers based on conducting, photosensitive polymers. The high value of the area reduction ratio and the associated high longitudinal strain rate ($\sim 1000\,s^{-1}$) imply that macromolecules in the nanofibers should be stretched and axially oriented in the direction of the jet axis. In the present context, the aim is to electrospin spinnable "host" polymer nanofibers containing luminescent "guest" conjugated polymers. Utilizing the high degree of chain extension, chain alignment, and structural order attainable, in principle, in electrospinning of the "host" polymer, one can expect to induce a similar order in the "guest" conjugated macromolecules incorporated in the nanofiber. This will allow a combination of the mechanical properties of electrospun "host" polymer nanofiber with the electronic properties (electric conductivity, anisotropic linear and non-linear optical properties, etc.) of the conjugated "guest" polymer.

Electrospinning of a blend of polyaniline doped with camphorsulfonic acid (PAn.HCSA) and polyethylene oxide (PEO) was previously demonstrated [89–91]. The electrospun nanofibers had diameters ranging between 950 nm and 2100 nm, with a generally uniform thickness along the fiber. The fibers formed a non-woven mat with high porosity with a relatively low conductivity comparing to cast films. The method proposed in [28] allows assembly of the individual electrospun nanofibers aligned with a preferable orientation relative to the substrate. In this method in addition to high molecular orientation of the nanofibers, a structural orientation is guaranteed. Photovoltaic diodes, which could be based on such nanofibers, are described in [146].

8.3. Protective clothing, chemical- and biosensors and smart fabrics

Protective clothing, which is under development at the Natick Soldier Center in Massachusetts, will employ polymer nanofibers as a key element [147]. The advantages of using nanofibers in protective clothing are twofold. (i) Nanofiber mats have a huge internal surface which allows an enhanced contact area between the protective medium and dangerous and aggressive environment. Examples of such an environment are lethal gases such as mustard gas, sarin and nerve gases, as well as aerosols of contagious disease spores, etc., which could be used in chemical and biological warfare.

(ii) It is relatively easy to incorporate different chemical agents into polymer solutions and (via electrospinning) into polymer nanofibers. These agents could effectively deactivate dangerous chemical and biological compounds in contact with them, and thus protect personnel. Nanofibers containing deactivating agents could also be used in gas masks. For all these applications, as well as for such applications as nanofiber-based filters, mass production of nanofibers at fast rate becomes crucial. This makes intensification of the manufacturing process based on electrospinning, as important as a search for appropriate stable deactivating agents compatible with nanofiber-forming polymer solutions.

Bulletproof vests based on nanofibers could become more effective and stronger than the Kevlar-based ones given the fact that spider dragline silk is stronger than Kevlar and stretches better than nylon [139, 140] (cf. Sec. 8.1). When nanofibers will be fabricated via electrospinning of the corresponding spider proteins (which is highly desirable and could be done in significant amounts using the recent achievement of gene engineering, cf. Sec. 8.1), bulletproof vests based on them can, indeed, be developed. Moreover, calculations in [26] proved that the coil-to-stretched conformation transition could be easily achieved in the electrospinning process (cf. Sec. 5.10.7). It is foreseen that electrospinning can provide a novel pathway for extended-chain polymer nanofibers without recourse to rigid or ultra-long chain architecture. The tensile modules and the strength of polymers depend on the degree of chain orientation. Achievement of a high degree of chain orientation has been an ongoing goal in the technology of high performance polymer fibers. The high draw ratios achieved in electrospinning (of the order of 1000) offer an opportunity to obtain highly oriented nanofibers with fully extended polymer chain conformation. These nanofibers electrospun from ordinary polymers are expected to be very strong and can also be useful in the development of new bulletproof protective vests.

Consider now a possible trend for the development of nanofiber-based chemical- and biosensors, as well as smart fabrics. In a recent work [148], micro-aerodynamic decelerators based on permeable surfaces of nanofiber mats were proposed and studied. The nanofibers were obtained through electrospinning of polymer solutions. The mats were electrospun directly onto light pyramid-shaped frames. These platforms fell freely through the stagnant air, apex down, at a constant velocity. The motivation of [148] stems from a necessity to develop very light airborne platforms of weight less than 1 g,

capable of carrying relatively large payloads up to several grams. The platforms, "smart dust" or "smart fabrics", should be capable of easily delivering various chemical, biological, thermal, radioactive, etc., sensors to the locations otherwise difficult to reach. This is of crucial importance in the cases of spillage or dissemination of hazardous materials, for atmospheric studies, etc. In spite of the fact that different platform configurations could be imagined, their feasibility is rooted in the same question: whether or not a permeable (and thus very light) parachute could possess the same drag as the corresponding intact one? It was demonstrated [148] that terminal velocity of such permeable structures is of the order of 30-50 cm/s with payloads of up to several grams. The reduced settling velocity at the mat porosities of the order of 0.8-0.9 shows that permeable wing or parachute based on nanofibers are possible. Passive platforms similar to those of [148] should be easily transported by wind to large distances. Active flapping or jet-propulsion-based light flying objects fabricated via electrospinning are also possible in principle. The interfiber spaces constitute a significant part of their area. This fact allows for a significant reduction in the weight of these structures compared to the corresponding impermeable structures. Moreover, permeable non-woven nanofiber networks are sufficiently strong but have negligible weight even compared to the light frames or to light plastic wrap. Therefore, the role of the non-woven fiber mats positioned on the frames is twofold: (i) they serve to generate drag force, while (ii) they reduce the weight. The ultimate aim of such a construction is to reduce the terminal settling velocity while carrying a useful payload (e.g. a sensor). (iii) In addition, the nanofiber mats can be electrospun for this purpose from photo-sensitive polymers, which can generate electric power for sensors from the sunlight, thus making the wings also a source of energy for the sensors and their transmitters.

Different chemical and biological indicators can easily be incorporated in polymers [149]. As a continuation of the work in [148], one of the chemical indicators (Bromophenol) was incorporated into nanofibers-based airborne platforms [150]. It was shown that the platforms changed their color subject to an appropriate acid or base environment thus serving as chemical indicators. This clearly indicates applicability of such devices in large scales. In [151], non-woven nanofiber mats incorporated pyrene methanol. The mats were used as a highly responsive fluorescence-based optical sensor for explosive detection.

Acknowledgements

The results presented in the course have been obtained in cooperation with my colleagues from the University of Akron, U.S.A., and the Technion – Israel Institute of Technology. I am deeply grateful to Prof. D.H. Reneker and Prof. E. Zussman, Dr. H. Fong and Dr. S. Koombhongse and Ph.D. students: W. Kataphinan and A. Theron. Cooperation with Prof. D. Weihs is acknowledged.

The work was supported in part by the Israel Science Foundation, the Israel Academy of Sciences, grant N 287/00-1. The hospitality and support of the University of Akron and of the Centre of Excellence AMAS of the Institute of Fundamental Technological Research, Polish Academy of Sciences are greatly appreciated.

Bibliography

1. G.M. Whitesides, J.P. Mathias, C.T. Seto, *Science*, 254, 1312 (1991).
2. G.A. Ozin, *Adv. Mat.*, 4, 612 (1992).
3. J.M. Schnur, *Science*, 262, 166 (1993).
4. C.R. Martin, *Science*, 266, 1961 (1994).
5. F.T. Edelmann, *Angew. Chem.*, 11, 1473 (1999), *Angew. Chem. Intern. Ed.*, 38, 1381 (1999).
6. S. Ijima, *Nature*, 354, 56 (1991).
7. M. Ghadiri, J.R. Granja, L. Buehler, *Nature*, 369, 301 (1994).
8. C.R. Martin, *Acc. Chem. Res.*, 28, 61 (1995).
9. E. Evans, H. Brownman, A. Leung, D. Needham, D. Tirrell, *Science*, 273, 933 (1996).
10. G.Y. Tseng, J.C. Ellenbogen, *Science*, 294, 1293 (2001).
11. T. Ondarcuhu, J. Joachim, *Europhys. Letters*, 42, 215 (1998).
12. D.H. Cobden, *Nature*, 409, 32 (2001).
13. X. Duan, Y. Huang, Y. Cui, J. Wang, C.M. Lieber, *Nature*, 409, 66 (2001).
14. M.P. Zach, K.H. Ng, R.M. Penner, *Science*, 290, 2120 (2000).
15. A. Hatzor, P.S. Weiss, *Science*, 291, 101 (2001).
16. E. Braun, Y. Eichen, U. Sivan, G. Ben-Yoseph, *Nature*, 391, 775 (1998).
17. J.K.N. Mbindyo, B.D. Reiss, B.R. Martin, C.D. Keating, M.J. Natan, T.E. Mallouk, *Adv. Mater.*, 13, 249 (2001).
18. P.K. Baumgarten, *J. Colloid Interface Sci.*, 36, 71 (1971).
19. L. Larrondo, R.St.J. Manley, *J. Polym. Sci., Part B: Polym. Phys.*, 19, 909 (1981).

20. L. LARRONDO, R.ST.J. MANLEY, *J. Polym. Sci., Part B: Polym. Phys.*, 19, 921 (1981).

21. L. LARRONDO, R.ST.J. MANLEY, *J. Polym. Sci., Part B: Polym. Phys.*, 19, 933 (1981).

22. D.H. RENEKER, I. CHUN, *Nanotechnology*, 7, 216 (1996).

23. A. FORMHALS, *U.S. Patent No. 1 975 504* (filed 1934).

24. H. FONG, I. CHUNG, D.H. RENEKER, *Polymer*, 40, 4585 (1999).

25. H. FONG, D.H. RENEKER, *J. Polym. Sci., Part B: Polym. Phys.*, 37, 3488 (1999).

26. D.H. RENEKER, A.L. YARIN, H. FONG, S. KOOMBHONGSE, *J. Appl. Phys.*, 87, 4531 (2000).

27. A.L. YARIN, S. KOOMBHONGSE, D.H. RENEKER, *J. Appl. Phys.*, 89, 3018 (2001).

28. A. THERON, E. ZUSSMAN, A.L. YARIN, *Nanotechnology*, 12, 384 (2001).

29. J.N. DOSHI, G. SHRINIVASAN, D.H. RENEKER, *Polym. News*, 20, 206 (1995).

30. J.N. DOSHI, G. SHRINIVASAN, D.H. RENEKER, *J. Electrostatics*, 35, 151 (1995).

31. X. TANG, D.H. RENEKER, *J. Macromol. Sci. Phys. Ed. B*, 36, 169 (1997).

32. R. JAEGER, H. SCHÖNHERR, G.J. VANSCO, *Macromol.*, 29, 7634 (1996).

33. R. JAEGER, M.M. BERGHOF, C. MARTIN I BATTLE, H. SCHÖNHERR, G.J. VANSCO, *Macromol. Symp.*, 127, 141 (1981).

34. M. BOGNITZKI, TH. FRESE, A. SCHAPER, J.H. WENDORFF, A. GEINER, Polym. Prep. (Am. Chem. Soc., Div. Polym. Chem.) 2000.

35. M. BOGNITZKI, H. HOU, M. ISHAQUE, TH. FRESE, M. HELLWIG, CH. SCHWARTE, A. SCHAPER, J.H. WENDORFF, A. GREINER, *Adv. Mat.*, 12, 637 (2000).

36. M. BOGNITZKI, W. CZADO, TH. FRESE, A. SCHAPER, M. HELLWIG, M. STEINHART, A. GREINER, J.H. WENDORFF, *Adv. Mat.*, 13, 70 (2001).

37. M. BOGNITZKI, W. CZADO, TH. FRESE, A. SCHAPER, M. HELLWIG, M. STEINHART, A. GREINER, J.H. WENDORFF, *Polym. Eng. Sci.*, (2002).

38. R.A. CARUSO, J.H. SCHATTKA, A. GREINER, *Adv. Mater.*, 13, 1577 (2001).

39. H. FONG, D.H. RENEKER, in: *Structure Formation in Polymer Fibers* (Eds.: D.R. Salem, M.V. Sussman), Hauser, 225 (2000).

40. A.L. YARIN, S. KOOMBHONGSE, D.H. RENEKER, *J. Appl. Phys.*, 90, 4836 (2001).

41. G.I. TAYLOR, *Proc. R. Soc. London, Ser. A*, 258, 383 (1964).

42. H. SCHLICHTING, *Boundary Layer Theory* (7^{th} ed.), McGraw-Hill, New York (1979).

43. YA. B. ZEL'DOVICH, *JETP*, 7 1463 (1937). Also: *Selected works of Ya. B. Zel'dovich*, Vol.1, *Chemical Physics and Hydrodynamics*, Princeton Univ. Press, Princeton, NJ (1992).

44. K.E. DZHAUGASHTIN, A.L. YARIN, *J. Eng. Phys.*, 32, 666 (1977).

45. A.L. YARIN, D.A. WEISS, *J. Fluid Mech.*, 283, 141 (1995).

46. C.F. EYRING, S.S. MACKEOWN, R.A. MILLIKAN, *Phys. Rev.*, 31, 900 (1928).

47. D.R. KINGHAM, L.W. SWANSON, *Appl. Phys. A: Solids Surf.*, 34, 123 (1984).

48. W.R. SMYTHE, *Static and Dynamic Electricity* (3^{rd} ed.), McGraw-Hill, New York (1968).

49. E. STERNBERG, W.T. KOITER, *J. Appl. Mech.*, 25, 575 (1958).

50. A.L. YARIN, G. BRENN, O. KASTNER, D. RENSIK, C. TROPEA, *J. Fluid Mech.*, 399, 151 (1999).

51. D. MICHELSON, *Electrostatic Atomization*, Adam Higler, Bristol and New York (1990).

52. M.T. HARRIS, O.A. BASARAN, *J. Colloid and Interface Sci.*, 161, 389 (1993).

53. H.A. STONE, J.R. LISTER, M.P. BRENNER, *Proc. R. Soc. London, Ser. A*, 455, 329 (1999).

54. J.D. SHERWOOD, *J. Phys. A*, 24, 4047 (1991).

55. H. LI, T.C. HALSEY, A. LOBKOVSKY, *Europhys. Lett.*, 27, 575 (1994).

56. V.G. SUVOROV, E.A. LITVINOV, *J. Phys. D*, 33, 1245 (2000).

57. A. RAMOS, A. CASTELLANOS, *Phys. Lett. A*, 184, 268 (1994).

58. R.G. FORBES, G.L.R. MAIR, *J. Phys. D*, 15, L153 (1982).

59. P.D. PREWETT, G.L.R. MAIR, S.P. THOMPSON, *J. Phys. D*, 15, 1339 (1982).

60. W. DRIESEL, CH. DIETZSCH, R. MUHLE, *J. Vac. Sci. Technol. B*, 14, 3367 (1996).

61. J. FERNANDEZ DE LA MORA, *J. Fluid Mech.*, 243, 561 (1992).

62. A.L. YARIN, *Free Liquid Jets and Films: Hydrodynamics and Rheology*, Longman, Harlow and Wiley, New York (1993).

63. M. STELTER, G. BRENN, A.L. YARIN, R.P. SINGH, F. DURST, *J. Rheol.*, 44, 595 (2000).

64. A.M. GANAN-CALVO, *J. Fluid Mech.*, 335, 165 (1997).

65. A.M. GANAN-CALVO, *J. Aerosol Sci.*, 30, 863 (1999).

66. L.T. CHERNEY, *J. Fluid Mech.*, 378, 167 (1999).

67. L.T. CHERNEY, *J. Aerosol Sci.*, 30, 851 (1999).

68. R.B. BIRD, R.C. ARMSTRONG, O. HASSAGER, *Dynamics of Polymeric Liquids* (2^{nd} ed.), Wiley, New York (1987).

69. A.L. YARIN, *J. Non-Newtonian Fluid Mech.*, 37, 113 (1990).

70. D.V. KHAKHAR, J.M. OTTINO, *Int. J. Multiphase Flow*, 13, 71 (1987).

71. J. JEANS, *The Mathematical Theory of Electricity and Magnetism*, Cambridge University Press, Cambridge (1958).

72. R.J. ARMS, F.R. HAMA, *Phys. Fluids*, 8, 553 (1965).

73. G.K. BATCHELOR, *An Introduction to Fluid Dynamics*, Cambridge University Press, Cambridge (1967).

74. H. AREF, E.P. FLENCHEM, *J. Fluid Mech.*, 148, 477 (1984).

75. A.L. YARIN, *J. Non-Newtonian Fluid Mech.*, 69, 137 (1997).

76. C. POZRIKIDIS, *Introduction to Theoretical and Computational Fluid Dynamics*, Oxford University Press, New York (1997).

77. A.L. YARIN, *J. Non-Newtonian Fluid Mech.*, 37, 113 (1990).

78. V.M. ENTOV, A.L. YARIN, *J. Fluid Mech.*, 140, 91 (1984).

79. A. ZIABICKI AND H. KAWAI (Eds.), *High-Speed Fiber Spinning*, Wiley, New York (1985).

80. A. ZIABICKI, *Fundamentals of Fibre Formation*, Wiley, London (1976).

81. M. SEAVER, A. GALLOWAY, T.J. MANUCCIA, *Rev. Sci. Instrum.*, 60, 3452 (1989).

82. G.I. TAYLOR, *Proc. R. Soc. London, Ser A*, 313, 453 (1969).

83. P.G. DE GENNES, *J. Chem. Phys.*, 60, 5030 (1974).

84. H. CHANG, A.S. LODGE, *Rheol. Acta*, 11, 127 (1972).

85. H. FONG, D.H. RENEKER, *J. Polym. Sci. Part B: Polym. Phys.*, 37, 3488 (1999).

86. J.P. YOUNGBLOOD, TH.J. MCCARTHY, *Macromolecules*, 32, 6800 (1999).

87. D. ONER, TH.J. MCCARTHY, *Langmuir*, 16, 7777 (2000).

88. H.J. BUSSCHER, A.W.J. VAN PELT, P. DE BOER, H.P. DE JONG, J. ARENDS, *Colloid. Surf. Sci.*, 9, 319 (1984).

89. I.D. NORRIS, M.M. SHAKER, F.K. KO, A.G. MACDIARMID, *Synthetic Metals*, 114, 109 (2000).

90. A.G. MACDIARMID, W.E. JONES, JR., I.D. NORRIS, J. GAO, A.T. JOHNSON, JR., N.J. PINTO, J. HONE, B. HAN, F.K. KO, H. OKUZAKI, M. LLAGUNO, *Synthetic Metals*, 119, 27 (2000).

91. A.G. MACDIARMID, *Angew. Chem. Int. Ed.*, 40, 2581 (2001). Also in: *Synthetic Metals*, 125, 11 (2002).

92. C. DREW, X. WANG, K. SENECAL, H. SCHREUDER-GIBSON, J. HE, S. TRIPATHY, L. SAMUELSON, *ANTEC 2000*, 1477 (2000).

93. E.G. RAKOV, *Russian Chemical Reviews*, 69, 35 (2000).

94. E.G. RAKOV, *Russian Chemical Reviews*, 70, 827 (2001).

95. H. SCHREUDER-GIBSON, K. SENECAL, M. SENNET, Z. HUANG, J. WEN, W. LI, D. WANG, S. YANG, Y. TU, Z. REN, C. SUNG, *Characteristics of electrospun carbon nanotube–polymer composites* (manuscript published online, 2002).

96. F.K. KO, W.B. HAN, S. KHAN, A. RAHMAN, O. ZHOU, *16th Annual Technical Conf.*, American Society of Composites (Nov. 2001).

97. B. VIGOLO, A. PENICAUD, C. COULON, C. SAUDER, R. PAILLER, C. JOURNET, P. BERNIER, P. POULIN, *Science*, 290, 1331 (2000).

98. B. MCCARTHY, S.A. CURRAN, A.B. DALTON, A.P. DAVEY, Z. KONYA, A. FONSECA, J.B. NAGY, W.J. BLAU, *J. Materials Science*, Letters 19, 2239 (2002).

99. A.B. DALTON, W.J. BLAU, G. CHAMBERS, J.N. COLEMAN, K. HENDERSON, S. LEFRANT, B. MCCARTHY, C. STEPHAN, H.J. BYRNE, *Synthetic Metals*, 121, 1217 (2001).

100. M.J. O'CONNELL, P.J. BOUL, L.M. ERICSON, C.B. HUFFMAN, Y. WANG, E. HAROZ, C. KUPER, J. TOUR, K.D. AUSMAN, R.E. SMALLEY, *Chemical Physical Letters*, 342, 265 (2001).

101. R. BANDYOPADHYAYA, E. NATIV-ROTH, O. REGEV, R. YERUSHALMI-ROZEN, *Nano Letters*, 0, 1 (2001).

102. I.W. HAMLEY, *Introduction to Soft Matter*, John Wiley, Chichester (2000).

103. P. LAUNOIS, A. MARUCCI, B. VIGOLO, P. BERNIER, A. DERRE, P. POULIN, *J. Nanoscience and Nanotechnology*, 1, 125 (2001).

104. H. SCHREUDER-GIBSON, K. SENECAL, M. SENNETT, L. SAMUELSON, *Proc. Electrochem. Soc.*, 2000 (2000).

105. C. JEROME, D. LABAYE, I. BODART, R. JEROME, *Synthetic Metals*, 101, 3 (1999).

106. S. DEMOUSTIER-CHAMPAGNE, J. DUCHET, R. LEGRAS, *Synthetic Metals*, 101, 20 (1999).

107. M. WAN, J. HUANG, Y. SHEN, *Synthetic Metals*, 101, 708 (1999).

108. C.H. HSU, H. SHIH, S. SUBRAMONEY, A.J. EPSTEIN, *Synthetic Metals*, 101, 677 (1999).

109. S.J. POMFRET, P.N. ADAMS, N.P. COMFORT, A.P. MONKMAN, *Synthetic Metals*, 101, 724 (1999).

110. J.M. DEITZEL, J.D. KLEINMEYER, J.K. HIRVONEN, N.C. BECK TAN, *Polymer*, 42, 8163 (2001).

111. E. ZUSSMAN, A. THERON, A.L. YARIN, *Proc. of 2nd IEEE Conference on Nanotechnology, Washington, DC, August 26-28*, 283 (2002).

112. P.A. SMITH, C.D. NORDQUIST, T.N. JACKSON, T.S. MAYER, *Appl. Phys. Letters*, 77, 1399 (2000).

113. Y. HUANG, X. DUAN, Q. WEI, C.M. LIEBER, *Science*, 291, 630 (2001).

114. W. LIU, Z. WU, D.H. RENEKER, *Polymer Preprints*, 41, 1193 (2000).

115. P. POZA, J. PEREZ-RIGUEIRO, M. ELICES, J. LLORCA, *Engineering Fracture Mechanics* (2001).

116. Q. FANG, D.G. CHETWYND, J.W. GARDNER, *Proc. of 2nd EUSPEN International Conference, Turin, Italy, May 27th-31st*, 32 (2001).

117. J.S. KIN, D.H. RENEKER, *Polymer Composites*, 20, 124 (1999).

118. S. CUENOT, S. DEMOUSTIER-CHAMPAGNE, B. NYSTEN, *Phys. Rev. Letters*, 85, 1690 (2000).

119. E.D. BOLAND, G.E. WNEK, D.G. SIMPSON, K.J. PAWLOWSKI, G.L. BOWLIN, *J. Macromol. Sci. – Pure Appl. Chem.*, A38, 1231 (2001).

120. J.A. MATTHEWS, G.E. WNEK, D.G. SIMPSON, G.L. BOWLIN, *Biomacromolecules*, 3, 232 (2002).

121. W.J. LI, C.T. LAURENCIN, E.J. CATERSON, R.S. TUAN, F.K. KO, *J. of Biomedical Materials Research*, 60, 613 (2002).

122. C.J. BUCHKO, K.M. KOZLOFF, D.C. MARTIN, *Biomaterials*, 22, 1289 (2001).

123. J.R. WOOD, Q. ZHAO, H.D. WAGNER, *Composites: Part A*, 32, 391 (2001).

124. M. STELTER, J. WUNDERLICH, S.K. RATU, G. BRENN, A.L. YARIN, R.P. SINGH, F. DURST, *J. Appl. Polym. Sci.*, 74, 2773 (1992).

125. T. WUNDERLICH, M. STELTER, T. TRIPATHY, B.R. NAYAK, G. BRENN, A.L. YARIN, R.P. SINGH, P.O. BRUNN, F. DURST, *J. Appl. Polym. Sci.*, 77, 3200, (2000).

126. M. STELTER, G. BRENN, A.L. YARIN, R.P. SINGH, F. DURST, *J. Rheol.*, 46, 507 (2002).

127. G.H. MCKINLEY, A. TRIPATHI, *J. Rheol.*, 44, 653 (2000).

128. J.R. MELCHER, G.I. TAYLOR, *Ann. Rev. Fluid Mech.*, 1, 111 (1969).

129. D.A. SAVILLE, *Ann. Rev. Fluid Mech.*, 29, 27 (1997).

130. M.M. DEMIR, I. YILGOR, E. YILGOR, E. ERMAN, *Polymer*, 43, 3303 (2002).

131. V.N. KIRICHENKO, I.V. PETRYANOV-SOKOLOV, N.N. SUPRUN, A.A. SHUTOV, *Sov. Phys. Dokl.*, 31, 611 (1986).

132. Y.M. SHIN, M.M. HOHMAN, M.P. BRENNER, G.C. RUTLEDGE, *Appl. Phys. Letters*, 78, 1149 (2001).

133. Y.M. SHIN, M.M. HOHMAN, M.P. BRENNER, G.C. RUTLEDGE, *Polymer*, 42, 9955 (2001).

134. M.M. HOHMAN, M. SHIN, G. RUTLEDGE, M.P. BRENNER, *Phys. Fluids*, 13, 2201 (2001).

135. M.M. HOHMAN, M. SHIN, G. RUTLEDGE, M.P. BRENNER, *Phys. Fluids*, 13, 2221 (2001).

136. J.J. FENG, *Phys. Fluids*, 14, 3912 (2002).

137. S. KOOMBHONGSE, W. Liu, D.H. Reneker, *J. Polym. Sci. Part B: Polym. Phys.*, 39, 2598 (2001).

138. D.H. RENEKER, W. KATAPHINAN, A. THERON, E. ZUSSMAN, A.L. YARIN, *Polymer*, 43, 6785 (2002).

139. R.F. SERVICE, *Science*, 295, 419 (2002).

140. A. LAZARIS, S. ARCIDIACONO, Y. HUANG, J.F. ZHOU, F. DUGUAY, N. CHRETIEN, E.A. WELSH, J.W. SOARES, C.N. KARATZAS, *Science*, 295, 472 (2002).

141. C. WEDER, C. SARWA, A. MONTALI, G. BASTIAANSEN, P. SMITH, *Science*, 279, 835 (1998).

142. P.K.H. HO, D.S. THOMAS, R.H. FRIEND, N. TESSLER, *Science*, 285, 233 (1999).

143. K.S. WHITEHEAD, M. GRELL, D.D.C. BRADLEY, *Applied Physics Letters*, 76, 2946 (2000).

144. M. GRELL, D.D.C. BRADLEY, *Adv. Mater.*, 11, 895 (1999).

145. T.W. HAGLER, K. PAKBAZ, K.F. VOSS, A.J. HEEGER, *Physical Review B*, 44, 8652 (1991).

146. M. GRANTSTROM, K. PETRITSCH, A.C. ARIAS, A. LUX, M.R. ANDERSSON, R.H. FRIEND, *Nature*, 395, 257 (1998).

147. *Nature*, 411, 236 (2001).

148. E. ZUSSMAN, A.L. YARIN, D. WEIHS, *Exp. in Fluids*, 33, 315 (2002).

149. SADAOKA, Y. SAKAI, M. YAMADA, *J. Mater. Sci.*, 3, 877 (1993).

150. Reports on this work were published by two Israeli newspapers "*Maariv*" on 5.5.02 (`http://images.maariv.co.il/cgi-bin/print/pl`) and "*Haaretz*" on 6.6.02 (`www.haaretzdaily.com`) [in Hebrew].

151. X. WANG, S.H. LEE, C. DREW, K.J. SENECAL, J. KUMAR, L.A. SAMUELSON, *Polymer Preprints*, 43, 130 (2002).

AMAS PUBLICATIONS

Already appeared in the *Lecture Notes* series:

1. J. HOLNICKI-SZULC (Ed.), *Structural Control and Health Monitoring*
2. P.J. PRENDERGAST, *Biomechanical Techniques for Pre-clinical Testing of Prostheses and Implants*
3. D. BIGONI, *Selected Mechanical Problems in Structural Ceramics*
4. Z. MRÓZ (Ed.), *Mechanics of Advanced Materials*

Already appeared in the *Conference Proceedings* series:

1. J. DEPUTAT and Z. RANACHOWSKI (Eds.), *Nondestructive Testing of Materials and Structures*
2. S. JENDO, K. DOLIŃSKI and M. KLEIBER (Eds.), *Reliability-Based Design and Optimisation*

INSTITUTE OF FUNDAMENTAL TECHNOLOGICAL RESEARCH
publishes the following periodicals:

ARCHIVES OF MECHANICS — bimonthly (in English)
ARCHIVES OF ACOUSTICS — quarterly (in English)
ARCHIVES OF CIVIL ENGINEERING — quarterly (in English)
ENGINEERING TRANSACTIONS — quarterly (in English)
COMPUTER ASSISTED MECHANICS AND ENGINEERING SCIENCES — quarterly (in English)
JOURNAL OF TECHNICAL PHYSICS — quarterly (in English)

Subscription orders for all journals edited by IFTR may be sent directly to:
Editorial Office
Institute of Fundamental Technological Research
Świętokrzyska 21, p. 508
00-049 Warszawa, POLAND
